Electroweak and Higgs physics at high energies

by

Yang Ma

B. Sc., Nanchang University, 2012

M. Sc., Chongqing University, 2016

M. Sc., University of Pittsburgh, 2017

Submitted to the Graduate Faculty of

the Dietrich School of Arts and Science in partial fulfillment

of the requirements for the degree of

Doctor of Philosophy

University of Pittsburgh

2022

UNIVERSITY OF PITTSBURGH

DIETRICH SCHOOL OF ARTS AND SCIENCES

This dissertation was presented

by

Yang Ma

It was defended on

April 19th 2022

and approved by

Tao Han, Department of Physics and Astronomy, University of Pittsburgh

Brian Batell, Department of Physics and Astronomy, University of Pittsburgh

Vittorio Paolone, Department of Physics and Astronomy, University of Pittsburgh

Manfred Paulini, Department of Physics, Carnegie Mellon University

Andrew Zentner, Department of Physics and Astronomy, University of Pittsburgh

Electroweak and Higgs physics at high energies

Yang Ma, PhD

University of Pittsburgh, 2022

Though the Standard Model (SM) of particle physics is one of the most successful achievements in modern physics and has been confirmed with almost all experimental results, it fails to explain mysteries such as the strong CP problem, the nature of dark matter, and the origin of neutrino mass, etc. Along this line, it is important to study phenomena at high-energy colliders to precisely test the SM and search for the hint of new physics beyond the SM. This thesis contains works in the following two related directions.

For future ultra-high-energy colliders where the collisions happen at energies well above the electroweak scale, the heavy SM particles could also be radiated off the beams. For the phenomenology studies at future high-energy colliders, all the SM particles should be treated as "partons" and a proper parton distribution function is needed. In this thesis, the electroweak parton distribution functions (EW PDFs) framework is introduced, where the Dokshitzer–Gribov–Lipatov–Altarelli–Parisi (DGLAP) evolution is employed to sum the large logarithms to obtain the EW PDFs at the Leading-Log accuracy. Using the EW PDFs formalism, partonic luminosities of a possible high-energy muon collider and the cross sections of typical SM processes are calculated to show the partonic picture of future ultra-high-energy lepton colliders.

The discovery of the Higgs boson at the Large Hadron Collider (LHC) is a milestone in particle physics. Since it is directly related to the electroweak symmetry breaking mechanism, Higgs is regarded as the portal to new physics. In this thesis, we suggest two approaches to test the Muon-Higgs coupling and the Charm-Higgs coupling respectively. By calculating the multi-boson production processes at a future multi-TeV muon collider, we show that it is possible to precisely measure the Muon-Higgs coupling. Using the non-relativistic QCD framework, we study the Higgs boson decay to a J/ψ and a pair of free charm quarks and show the possibility to measure the Charm-Higgs coupling at a 3 ab^{-1} high-luminosity LHC.

Table of Contents

Preface xiv
1.0 Introduction 1
  1.1 The Standard Model of particle physics 1
    1.1.1 The Standard Model Lagrangian 2
      1.1.1.1 SM gauge sector 2
      1.1.1.2 SM fermion sector 4
      1.1.1.3 SM Higgs sector 7
      1.1.1.4 SM Yukawa sector 9
      1.1.1.5 Quark mass mixing and the Cabibbo–Kobayashi–Maskawa matrix 11
  1.2 Relativistic kinematics and phase space 12
    1.2.1 Relativistic kinematics 12
    1.2.2 Phase space 14
      1.2.2.1 One body phase space 14
      1.2.2.2 Two body phase space 15
      1.2.2.3 Three body phase space 16
      1.2.2.4 Recursion relation for the phase space element 17
    1.2.3 Cross section and decay width 18
2.0 Electroweak parton distribution functions 20
  2.1 Approximations at the leading order 20
    2.1.1 Equivalent photon approximation 20
    2.1.2 Effective weak boson approximation 25
  2.2 Electroweak parton distribution functions 26
  2.3 The evolution of the SM electroweak parton distribution functions 27
    2.3.1 PDF evolution in QED and QCD 29
    2.3.2 The complete SM running above μ_{EW} 31
3.0 Standard Model physics at a high-energy muon collider 36

3.1 The physics picture of a high-energy muon collider 36
    3.1.1 Introduction 36
    3.1.2 The partonic picture of a high-energy muon collider 39
    3.1.3 Discussions and conclusions 43
3.2 Colored partons of high-energy leptons 45
    3.2.1 PDFs and partonic luminosities at a lepton collider 45
    3.2.2 The standard processes and jet production 50
        3.2.2.1 EW processes 50
        3.2.2.2 Jet production 54
    3.2.3 Summary 62
4.0 Yukawa couplings of the second generation fermions 65
4.1 Precision test of the Muon-Higgs coupling at a high-energy muon collider . . 65
    4.1.1 Introduction 65
    4.1.2 EFT Description of an Anomalous Muon Yukawa Coupling 67
        4.1.2.1 The Yukawa interaction in the HEFT parameterization 68
        4.1.2.2 The Yukawa interaction in the SMEFT parameterization . . . 71
        4.1.2.3 Unitarity bounds on a nonstandard Yukawa sector 75
    4.1.3 Phenomenology of Muon-Higgs Coupling at a high-energy Muon Collider 78
        4.1.3.1 Multi-boson production 78
        4.1.3.2 Kinematic distributions 84
        4.1.3.3 Statistical sensitivity on the Muon Yukawa Coupling 89
    4.1.4 Summary 93
4.2 Higgs boson decay to charmonia via charm quark fragmentation 94
    4.2.1 Calculational Formalism 96
        4.2.1.1 Color-singlet states 97
        4.2.1.2 Color-octet states 99
        4.2.1.3 Electroweak contributions 102
    4.2.2 Phenomenological results 104
        4.2.2.1 Standard Model results 104
        4.2.2.2 Probing the charm quark Yukawa 108

4.2.2.3 Backgrounds . . . 111
4.2.3 Summary . . . 113
5.0 Conclusions . . . 115
Appendix A. Rotation of Wavefunctions . . . 117
Appendix B. The splitting functions . . . 118
Appendix C. The running of the Muon Yukawa Coupling . . . 121
Appendix D. Polarization sum . . . 126
Bibliography . . . 127

List of Tables

1 Weak quantum numbers for the quarks and leptons in a single generation. The symbol T denotes the weak isospin, T_3 is the third component of T, Y is the hypercharge, and Q is the electric charge. 6

2 Weak quantum numbers for ϕ^+ and ϕ^0. The symbol T denotes the weak isospin, T_3 is the third component of T, Y is the hypercharge, and Q is the electric charge. 7

3 Momentum fractions (%) carried by various parton species. The sea leptons include $\ell_{\rm sea} = \bar{\mu} + \sum_{i\neq\mu}(\ell_i + \bar{\ell}_i)$ and $\nu = \sum_i(\nu_i + \bar{\nu}_i)$. The quark components include all the 6 flavors. 27

4 Production cross sections at a muon collider in units of fb by VBF utilizing the EW PDF and by direct $\mu^+\mu^-$ annihilation with ISR effects. 43

5 The averaged momentum fractions [%] carried by each parton species for (a) an electron beam and (b) a muon beam with a few representative values of the factorization scale Q. 49

6 Some representative cross sections in e^+e^- and $\mu^+\mu^-$ collisions including both annihilation and fusion for a variety of energies. We have included the ISR for the annihilation processes. The fusion to $W^+W^-, t\bar{t}$ cross sections only include the dominated $\gamma\gamma$ initialized processes with the resummed γ PDF. The acceptance cuts in Eq. (201) are applied to the final-state particles, including the W^+W^- and $t\bar{t}$ as well. The numbers outside (inside) of the parentheses correspond cross sections with the acceptance cut $|\eta_j| < 3.13$ ($|\eta_j| < 2.44$). 63

7 The cut-flow for the cross sections of WWH and ZHH production through annihilation (SM with $\kappa_\mu = 1$) with and without ISR, and the BSM signal models for $\kappa_\mu = 0$ (2) (i.e., $\Delta\kappa_\mu = \pm 1$). The last two columns are the SM backgrounds from charged (CVBF) and neutral vector boson fusion (NVBF), respectively. All cross sections are at a $\sqrt{s} = 10$ TeV $\mu^+\mu^-$ collider. The event numbers correspond to an integrated luminosity $\mathcal{L} = 10$ ab^{-1}. The signal and background are defined in Eq. (236). 88

8 Some fitted numerical values of color-octet (CO) LDMEs for J/ψ production (in units of GeV^3) 100

9 Color factors of different Feynman diagrams for the CS and CO SDCs. The pure QCD contribution, pure QED contribution and the QCD/QED interference are represented as QCD, QED, and QCD×QED, respectively. 102

10 Color factors of the HZZ diagrams for the CS and CO SDCs. 103

11 The ratios of the SDCs to their pure QCD values $\hat{\Gamma}_{\mathbb{N}}/\hat{\Gamma}_{\mathbb{N}}^{\mathrm{QCD}}$. The pure QCD contribution, pure QED contribution, QCD/QED interference, and EW correction are marked as QCD, QED, QCD×QED, and EW, respectively. 105

12 The decomposed numerical values of $\Gamma(H \to c\bar{c}+J/\psi(\eta_c))$ and the corresponding branching fractions. 106

13 The CO contributions to $\Gamma(H \to c\bar{c} + J/\psi(\eta_c))$ and the branching fractions. . . 110

List of Figures

1 Elementary particles in the Standard Model. 1

2 Illustration for the recursion relation that relates an n-body phase space element to the product of a two-body phase space element and an $(n-1)$ one. This figure is adopted from Ref. [5]. 17

3 Diagrammatic representation of $fX \to X\gamma^* \to fY$ scattering. 21

4 Production cross sections in $\mu^+\mu^-$ collisions versus the c.m. energy. The dashed falling curves are for the direct $\mu^+\mu^-$ annihilation, and the solid falling curves (slightly above the dashed) include the ISR effects. The solid rising curves are for $\gamma\gamma$-EPA by Eq. (190) and the dashed rising curves are from the leading-order γ-PDF at $Q = \sqrt{\hat{s}}/2$. 37

5 Distributions for (a) EW PDFs $f_i(x)$ and, (b) parton luminosities $\mathrm{d}\mathcal{L}_{ij}/\mathrm{d}\tau$ versus $\sqrt{\tau}$ for $\sqrt{s} = 30$ TeV with a factorization scale $Q = \sqrt{\hat{s}}/2$ (solid) and $\sqrt{\hat{s}}$ (dashed). 40

6 Production cross section for semi-inclusive processes at a $\mu^+\mu^-$ collider versus the c.m. energy. The solid curves are for (a) the total cross sections and the dashed (dotted) curves from VBF ($\mu^+\mu^-$ annihilation) with EW PDF, and (b) for $t\bar{t}$ production decomposed to the underlying contributions from $\mu^+\mu^-, \gamma/Z/\gamma Z, W_TW_L$, W_LW_L and W_TW_T. 41

7 Normalized differential distributions for the final state $t\bar{t}$ system (a) the invariant mass $m_{t\bar{t}}$ and (b) the rapidity $y_{t\bar{t}}$. 42

8 PDFs in a high-energy lepton for (a) an electron and (b) a muon below the EW scale at $Q = 30$ (50) GeV; and for (c) an electron and (d) an muon above the EW scale at $Q = 3$ (5) TeV. 46

9 Parton luminosities $\mathrm{d}\mathcal{L}_{ij}/\mathrm{d}\tau$ for (a) an e^+e^- collider at $\sqrt{s} = 3$ TeV, (b) a $\mu^+\mu^-$ collider at $\sqrt{s} = 3$ TeV, (c) an e^+e^- collider at $\sqrt{s} = 10$ TeV, and (d) a $\mu^+\mu^-$ collider at $\sqrt{s} = 10$ TeV. The factorization scale is chosen as $Q = \sqrt{\hat{s}}/2$ (solid curves) and $\sqrt{\hat{s}}$ (dashed curves). 51

10 Cross sections for the annihilation processes versus the collider c.m. energy for an e^+e^- collider (left panels) and a $\mu^+\mu^-$ collider (right panels) with basic acceptance cuts in Eq. (201). The downward dashed (dotted for $\tau^+\tau^-$) curves indicate the corresponding Bhabha scattering and $\ell^+\ell^-$ annihilation processes with (without) ISR. 53

11 The photonic (a) and leptonic (b) cross sections for photon-induced hadronic production at high-energy lepton colliders. We adopted the models by Pythia [81, 82] or SLAC [77] parameterizations as stated in the text. 56

12 Cross sections for di-jet (or W^+W^-) production ($j = q, g$) versus the collider c.m. energy for an e^+e^- collider (left panels) and a $\mu^+\mu^-$ collider (right panels) with basic acceptance cuts in Eq. (201). 57

13 Invariant mass (m_{ij}, upper panels) and rapidity (y_{ij}, lower panels) distributions for the di-jet (or W^+W^-) system from various sub-processes for an e^+e^- collider at $\sqrt{s} = 3$ TeV (left panels), and a $\mu^+\mu^-$ collider at $\sqrt{s} = 10$ TeV (right panels), respectively. 59

14 Inclusive jet (or W) distributions for transverse momentum (p_T^j, upper panels), jet energy (E_j, middle panels) and the normalized pseudo-rapidity (η_j, lower panels) in various sub-processes for an e^+e^- collider at $\sqrt{s} = 3$ TeV (left panels), and a $\mu^+\mu^-$ collider at $\sqrt{s} = 10$ TeV (right panels), respectively. 61

15 Inclusive inelastic cross section $\mu^+\mu^- \to X$ for multiple Goldstone and Higgs-boson production in the GBET approximation. We show the result for the sequence of SMEFT scenarios defined by the conditions in Eq. (222), truncated at dimension $d = 6, 8, 10, 12, 14$, respectively. The maximal multiplicity of the final state is $n = 3, 5, 7, 9, 11$, respectively. The shaded area indicates the region that is excluded by the universal unitarity bound for the inclusive cross section in Eq. (230). 77

16 The cross sections of diboson production at a $\mu^+\mu^-$ collider as a function of the c.m. energy $\sqrt{s}$. The solid and dotted lines are for the direct annihilation with muon Yukawa coupling as $\kappa_\mu = 1$ and $\kappa_\mu = 0$ (2) (hardly visible), respectively. The dashed rising curves are the (charged) vector boson fusions (VBF), $\mu^+\mu^- \to \nu_\mu\bar{\nu}_\mu X$, calculated using the fixed-order (FO) approach with a cut on the invariant mass of $\nu_\mu\bar{\nu}_\mu$ pair $M_{\nu_\mu\bar{\nu}_\mu} > 150\,\text{GeV}$. All calculations are carried out with WHIZARD 2.8.5. 79

17 Similar to Fig. 16, the cross sections of three-boson production at a $\mu^+\mu^-$ collider as a function of the c.m. energy $\sqrt{s}$. 80

18 Similar to Fig. 16, the cross sections of four-boson production at a $\mu^+\mu^-$ collider as a function of the c.m. energy $\sqrt{s}$, for SM $\kappa_\mu = 1$ only. 80

19 The cross sections of four-boson production at a $\mu^+\mu^-$ collider via (a) annihilation $\mu^+\mu^- \to 4B$ and (b) the (charged) vector boson fusions (VBF), $\mu^+\mu^- \to \nu_\mu\bar{\nu}_\mu X$ as functions of the c.m. energy $\sqrt{s}$. The solid and dotted lines are for the results with muon Yukawa coupling as $\kappa_\mu = 1$ and $\kappa_\mu = 0$ (2), respectively. 81

20 Representative diagrams for the signal annihilation process $\mu^+\mu^- \to W^+W^-H$ (left and middle), and for the VBF background process (right). 84

21 The kinematic distributions of the boson angle θ_B, the diboson distance R_{BB}, and the triboson invariant mass M_{3B} ($B = W, H$), respectively, in the WWH production at a $\sqrt{s} = 10$ TeV $\mu^+\mu^-$ collider. 85

22 The kinematic distributions for θ_B, R_{BB}, and M_{3B} as in Fig. 21, but for ZHH production at a $\sqrt{s} = 10$ TeV $\mu^+\mu^-$ collider. 86

23 The cross sections of annihilation without ISR for the three-boson production channels $\mu^+\mu^- \to WWH, ZZZ, ZZH, ZHH$ versus the $\mu^+\mu^-$ c.m. energy $\sqrt{s}$ and the effective coupling κ_μ. The lower two clusters of curves correspond the flow cut: $\theta_{if} > 10^\circ$ and the accumulated $\Delta R > 0.4$. 90

24 The statistical sensitivity of a high-energy muon collider to the muon Yukawa coupling κ_μ from the measurements of three-boson production. 92

25 Feynman diagrams for a charmonium Fock state $\langle c\bar{c}\rangle$ production from Higgs decay via charm-quark fragmentation. 97

26 QED Feynman diagrams for color-singlet (CS) charmonium state production via $H \to c + \bar{c} + \langle c\bar{c} \rangle$. 98

27 Feynman diagrams for color-octet (CO) charmonium state production. (a) and (b) are the single gluon fragmentation to ${}^3S_1^{[8]}$ state, while (c) and (d) contribute to both ${}^3S_1^{[8]}$ and ${}^1P_1^{[8]}$ states. 101

28 Feynman diagrams for charmonium state production through the HZZ coupling. 103

29 Feynman diagrams for charmonium state production with top-quark and W loop contributions. The gluonic diagram in (a) only contributes to ${}^3S_1^{[8]}$, while the photon one in (c) only contributes to ${}^3S_1^{[1]}$. 104

30 Charmonium energy distributions for (a) J/ψ and (b) η_c. The blue dotted and orange dashed curves are for color-singlet (CS) QCD only and QCD+QED contributions, the red (green) solid curve is for the sum of full leading order (full CS) result. All curves are normalized using the full leading order decay width in Table 12. 108

31 Transverse momentum distributions in the Higgs rest frame $H \to c\bar{c} + J/\psi$ (η_c): (a) and (b) for J/ψ and η_c distributions, respectively; (c) and (d) for the charm quark distributions associated with J/ψ and η_c, respectively, where the solid curves are for the p_T^{max} and dashed curves are for the p_T^{min} distribution. The red, green and black curves are for CS, CO, and the full leading order result. All curves are normalized using the full leading order decay width in Table 12. . . . 109

32 Charmonium energy distributions for (a) J/ψ and (b) η_c for $\kappa_c = 1$ (SM), 3, 5. The solid curves are for the one-loop running mass $m_c(m_H) = 0.694$ GeV; the dashed curves are for the four-loop running mass $m_c(m_H) = 0.629$ GeV. The dotted purple curve is for the background from Hbb decay mode. The colored bands are for the uncertainties from the CO LDMEs. All curves are normalized using the full SM leading order decay width in Table 12. 111

33 Feynman diagrams for $H \to b\bar{b} + J/\psi(\eta_c)$ production. The gluon diagrams in (a, b) only contribute to ${}^3S_1^{[8]}$, while the photon ones only contribute to ${}^3S_1^{[1]}$. (c) is nonzero only for the CS states. 113

34 LO RGE running of the muon Yukawa y_μ coupling as a function of the energy scale Q, in the SM (red solid). In the extra-dimensional scenarios (with inverse radius $1/R = 3$ TeV), we consider 1) Bulk: all fields propagating in the bulk, and 2) Brane: all matter fields localized to the brane. 122

35 LO RGE running of SM vacuum expectation value v (left scale) and muon mass m_μ (right scale) as functions of the energy scale Q. 122

Preface

At this point, I would like to gratefully acknowledge my debt to my Ph.D. supervisor, Tao Han, for all his guidance, support, comments, and even criticism throughout my full Ph.D. career. His enthusiasm in science and deep knowledge in collider physics have always been a source of my own passion and determination in research. Words fail me in expressing how much I have been learning from him and how much I would like to thank him. I would like to also express my gratitude to the members of my thesis committee: Brian Batell, Vittorio Paolone, Manfred Paulini, and Andrew Zentner, for their suggestions and questions on my thesis work.

The works presented in this thesis would not have been accomplished without the help from many collaborators. Apart from Tao, I am particularly grateful to Keping Xie for his help and support in our works on the electroweak parton distribution functions and the phenomenology at future multi-TeV lepton colliders. I have benefited a lot in physics understandings from the discussions with Adam Leibovich on non-relativistic quantum chromodynamics and I have also learned about the effective field theory as well as the WHIZARD package from my coauthors Wolfgang Kilian, Nils Kreher, Jürgen Reuter, and Tobias Striegl. Xiaoze Tan helped me to check and confirm the numerical results of the Higgs decay to charmonia calculation.

I would like to thank all the professors and visitors of the physics department that I have taken courses from: Brian Batell, Daniel Boyanovsky, Ayres Freitas, Tao Han, Kaoru Hagiwara, Jeremy Levy, Roger Mong, Manfred Paulini, and Andrew Zentner. I earned teaching experience by serving as a graduate teaching assistant, and I would like to thank the instructors that I was working with, Matteo Broccio, Russell Clark, and Vittorio Paolone for their guidance in teaching strategies and skills.

The support from my friends and colleagues at Pitt should never be underestimated in my Ph.D. life. Thank Barmak Shams, who was sharing the office space with me for two years and has been encouraging me since 2017. Thank Rudrajit Banerjee and Christine Mazzola for our tons of long conversations. Thank my friends Hongbo Cai, Junmou Chen, Lisong

Chen, Yilun Guan, Shan Hao, Iris Leung, Chi Wing Ng, Weitao Shan, Qian Song, Qi Yao, Dengyu Yang, Bomin Zhang, for their help whenever I needed.

Last but not least, I would like to thank my family members. I am particularly grateful to my parents for bringing me to the world. They both have set great examples for their son, which have made me into the person I am. I also owe special thanks to my girlfriend, whose absence made it possible for me to finish this thesis on time.

1.0 Introduction

1.1 The Standard Model of particle physics

The Standard Model (SM) of particle physics provides a remarkable successful description of the elementary matter and forces that found the picture of the universe. The SM is a gauge theory in the framework of quantum field theory and is based on the local symmetry group $SU(3)_c \times SU(2)_L \times U(1)_Y$, where the indices denote color, weak isospin, and hypercharge. The gauge structure uniquely controls the strong, weak, and electromagnetic interactions between matter particles and force carriers with the coupling constants determined from experiments. All elementary particles in the SM are listed in Fig. 1. According to the SM, the matters are made of fermions, *i.e.* quarks and leptons, and the gauge interactions are carried by gauge bosons *i.e.* photon, gluon, the W and Z bosons. The Higgs boson is the only scalar particle (spin-0) in the SM and it gives rise of masses of all the other elementary particles via the electroweak symmetry breaking (EWSB) mechanism. This chapter will briefly introduce the SM, which helps the readers to understand my research.

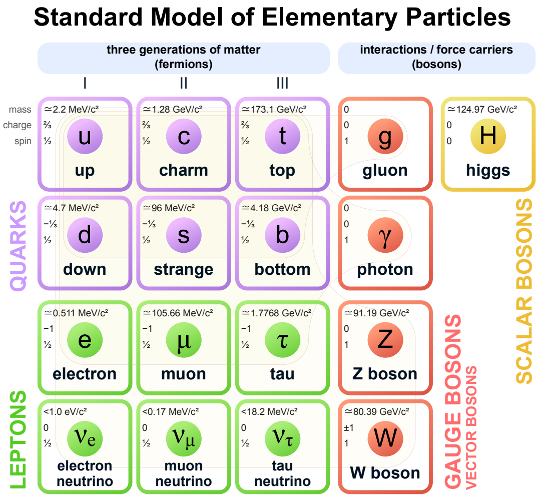

Figure 1: Elementary particles in the Standard Model.

1.1.1 The Standard Model Lagrangian

The dimension-four Lagrangian of the SM reads

$$\mathcal{L}_{\rm SM} = \mathcal{L}_{\rm Gauge} + \mathcal{L}_{\rm Fermion} + \mathcal{L}_{\rm Higgs} + \mathcal{L}_{\rm Yukawa}, \tag{1}$$

which includes the gauge, fermion, Higgs, and Yukawa sectors of the theory. We will discuss these terms in details in the following.

1.1.1.1 SM gauge sector

The gauge sector of the SM is given by the gauge boson kinetic terms

$$\mathcal{L}_{\rm Gauge} = -\frac{1}{4}G^a_{\mu\nu}G^{\mu\nu}_a - \frac{1}{4}W^i_{\mu\nu}W^{\mu\nu}_i - \frac{1}{4}B_{\mu\nu}B^{\mu\nu}. \tag{2}$$

The field strength tensors for $SU(3)_c$, $SU(2)_L$, and $U(1)_Y$ are

$$\begin{aligned} G^a_{\mu\nu} &= \partial_\mu G^a_\nu - \partial_\nu G^a_\mu - g_s f_{abc} G^b_\mu G^v_\nu, \quad a,\, b,\, c \in [1,\, 8], & (3)\\ W^i_{\mu\nu} &= \partial_\mu W^i_\nu - \partial_\nu W^i_\mu - g\epsilon_{ijk} W^j_\mu W^k_\nu, \quad i,\, j,\, k \in [1, 3], & (4)\\ B_{\mu\nu} &= \partial_\mu B_\nu - \partial_\nu B_\mu. & (5) \end{aligned}$$

where g_s and g and the corresponding couplings, the indices $a,\, b,\, c = 1, \dots 8$ are introduced for the color degrees of freedom, and $i,\, j,\, k = 1, \dots 3$ are for the left-handed weak isospin degrees of freedom. The eight fields G^a_μ and the three fields W^i_μ correspond to the $SU(3)_c$ generator $T^a = \lambda^a/2$ and the $SU(2)_L$ generator $\tau^i = \sigma^i/2$, respectively. Explicitly, we have

$$\lambda^1 = \begin{pmatrix} 0 & 1 & 0 \\ 1 & 0 & 0 \\ 0 & 0 & 0 \end{pmatrix}, \quad \lambda^2 = \begin{pmatrix} 0 & -i & 0 \\ i & 0 & 0 \\ 0 & 0 & 0 \end{pmatrix}, \quad \lambda^3 = \begin{pmatrix} 1 & 0 & 0 \\ 0 & -1 & 0 \\ 0 & 0 & 0 \end{pmatrix}, \quad \lambda^4 = \begin{pmatrix} 0 & 0 & 1 \\ 0 & 0 & 0 \\ 1 & 0 & 0 \end{pmatrix}, \tag{6}$$

$$\lambda^5 = \begin{pmatrix} 0 & 0 & -i \\ 0 & 0 & 0 \\ -i & 0 & 0 \end{pmatrix}, \quad \lambda^6 = \begin{pmatrix} 0 & 0 & 0 \\ 0 & 0 & 1 \\ 0 & 1 & 0 \end{pmatrix}, \quad \lambda^7 = \begin{pmatrix} 0 & 0 & 0 \\ 0 & 0 & -i \\ 0 & i & 0 \end{pmatrix}, \quad \lambda^8 = \frac{1}{\sqrt{3}}\begin{pmatrix} 1 & 0 & 0 \\ 0 & 1 & 0 \\ 0 & 0 & -2 \end{pmatrix}, \tag{7}$$

and

$$\sigma^1 = \begin{pmatrix} 0 & 1 \\ 1 & 0 \end{pmatrix}, \quad \sigma^2 = \begin{pmatrix} 0 & -i \\ i & 0 \end{pmatrix}, \quad \sigma^3 = \begin{pmatrix} 1 & 0 \\ 0 & -1 \end{pmatrix}. \tag{8}$$

There exist commutation relations between the SM gauge group generators

$$[T^a, T^b] = i f^{abc} T_c, \quad [\tau^i, \tau^j] = i\epsilon^{ijk}\tau_k, \quad [Y, Y] = 0, \tag{9}$$

where ϵ^{ijk} is the three-dimensional Levi-Civita tensor and the non-zero antisymmetric color structure constants f^{abc} are

$$f^{123} = 1,\ f^{458} = f^{678} = \frac{\sqrt{3}}{2},\ f^{147} = f^{246} = f^{257} = f^{345} = f^{516} = f^{637} = \frac{1}{2}. \tag{10}$$

Due to the non-abelian property of the $SU(2)$ and $SU(3)$ groups, self-interactions between the gauge fields show up as

$$\begin{aligned} \text{Triple gauge boson coupling} \quad &: \quad i g_I \,\mathrm{Tr}\,(\partial_\nu V_\mu - \partial_\mu V_\nu)\,[V_\mu, V_\nu], \\ \text{Quartic gauge boson coupling} \quad &: \quad \frac{1}{2} g_I^2 \,\mathrm{Tr}[V_\mu, V_\nu]^2, \end{aligned}$$

for $V_\mu = W_\mu$ or G_μ and g_I is the corresponding coupling constant.

1.1.1.2 SM fermion sector

The SM fermion sector contains massless chiral fermion fields that couple to the bosoinc fields through gauge or Yukawa interactions. Consider a Dirac fermion field ψ, its left-handed (LH) and right-handed (RH) components are defined by

$$\psi_{L(R)} \equiv P_{L(R)} = \frac{1 \mp \gamma^5}{2}\psi, \tag{11}$$

where the $P_{L(R)}$ is the chiral projection operator. The SM fermion sector contains the LH doublets

$$Q_L^{am} = \begin{pmatrix} u_L^{\alpha m} \\ d_L^{\alpha m} \end{pmatrix}, \quad L_L^m = \begin{pmatrix} \nu_L^m \\ e_L^m \end{pmatrix}, \tag{12}$$

and RH singlets

$$u_R^{\alpha m}, \quad d_R^{\alpha m}, \quad e_R^m, \tag{13}$$

where α is the color index and $m = 1, 2, 3$ represents that there are three generations of fermions. It is worthy to mention that there is no RH neutrino ν_R in the SM.

The Lagrangian of the SM fermion sector is

$$\mathcal{L}_{\text{Fermion}} = i \sum_{m=1}^{3} \left(\bar{Q}_L^{\alpha m} \not{D} Q_L^{\alpha m} + \bar{L}_L^m \not{D} L_L^m + \bar{u}_R^{\alpha m} \not{D} u_R^{\alpha m} + \bar{d}_R^{\alpha m} \not{D} d_R^{\alpha m} + \bar{e}_R^m \not{D} e_R^m \right), \tag{14}$$

where the covariant derivative D_μ is defined as

$$D_\mu = \partial_\mu + i g_s T^a G_\mu^a + i g \tau^i W_\mu^i + i g' \frac{Y}{2} B_\mu. \tag{15}$$

It can be read from the Lagrangian that a SM matter field ψ couples to the a gauge field V_μ with an interaction coupling constant g_I as

$$\text{Fermion} - \text{gauge boson coupling}: \quad - g_I \bar{\psi} V_\mu \gamma^\mu \psi.$$

So far, we have the Lagrangian

$$\mathcal{L}_{\text{Gauge}} + \mathcal{L}_{\text{Fermion}}$$

that is invariant under the infinitesimal local gauge transformation of $SU(2)_L$ and $U(1)_Y$ as

$$\begin{array}{cc}
SU(2)_L & U(1)_Y \\
\psi_L \to (1 - ig\vec{\tau}\cdot\vec{\alpha}(x))\,\psi_L & \psi_L \to \left(1 - ig'\tfrac{Y}{2}\beta(x)\right)\psi_L \\
\psi_R \to \psi_R & \psi_R \to \left(1 - ig'\tfrac{Y}{2}\beta(x)\right)\psi_R \\
\vec{W}_\mu \to \vec{W}_\mu + \partial_\mu\vec{\alpha}(x) + g\vec{\alpha}\times\vec{W}_\mu & W_\mu \to W_\mu \\
B_\mu \to B_\mu & B_\mu \to B_\mu + \partial_\mu\beta(x)
\end{array}$$

By introducing the isospin raising and lowering operators

$$\tau^{\pm} = \left(\tau^1 \pm i\tau^2\right)/\sqrt{2}, \tag{16}$$

the W^i_μ field can be redefined as

$$W^{\pm}_\mu = \left(W^1_\mu \mp iW^2_\mu\right)/\sqrt{2}, \quad W^0_\mu = W^3_\mu, \tag{17}$$

and hence

$$\begin{aligned}
\vec{\tau}\cdot\vec{W}_\mu = \tau^i W^i_\mu &= \tau^1 W^1_\mu + \tau^2 W^2_\mu + \tau^3 W^3_\mu \\
&= \tau^+ W^+_\mu + \tau^- W^-_\mu + \tau^3 W^0_\mu.
\end{aligned} \tag{18}$$

The W^+, W^-, and W^0 can be understood as gauge bosons that increases, decreases, or leaves the weak isospin unchanged of a field that absorbs it. In order to unify the electromagnetic interaction with the weak interaction, the electromagnetic term $ieQA_\mu$ should be included in the neutral term of the covariant derivative D_μ. The above requirement indicates that the gauge fields W^3 and B can be related to A and another neutral field Z

$$\begin{pmatrix} W^3_\mu \\ B_\mu \end{pmatrix} = \begin{pmatrix} \cos\theta_W & \sin\theta_W \\ -\sin\theta_W & \cos\theta_W \end{pmatrix} = \begin{pmatrix} Z_\mu \\ A_\mu \end{pmatrix}, \tag{19}$$

where θ_W is the electroweak mixing angle. The neutral term in D_μ is then written as

$$ig\tau^3 W^3_\mu + ig'\frac{Y}{2}B_\mu = iA_\mu\left(g\sin\theta_W\tau^3 + g'\cos\theta_W\frac{Y}{2}\right) + iZ_\mu\left(g\cos\theta_W\tau^3 - g'\sin\theta_W\frac{Y}{2}\right). \tag{20}$$

Requiring the coefficient of the electromagnetic field A_μ to be ieQ, we need the coupling constants to obey

$$g = \frac{e}{\sin\theta_W}, \quad g' = \frac{e}{\cos\theta_W}. \tag{21}$$

Finally, we have the covariant derivative in form

$$D_\mu = \partial_\mu + ig_s T^a G^a_\mu + \frac{ig}{\sqrt{2}}\tau^+ W^+_\mu + \frac{ig}{\sqrt{2}}\tau^- W^-_\mu + ieQA_\mu + ig_Z Z_\mu(\tau^3 - \sin^2\theta_W Q), \tag{22}$$

with the coupling $g_Z = e/(\sin\theta_W \cos\theta_W)$.

The weak hypercharge Y of a field is related to its electric charge Q and the third component of its weak isospin T_3 as

$$Q = T_3 + \frac{Y}{2}. \tag{23}$$

The weak quantum numbers for the SM fermions in a single generation are listed in Table 1.

	ν_L	e_L	u_L	d_L	e_R	u_R	d_R
T	$\frac{1}{2}$	$\frac{1}{2}$	$\frac{1}{2}$	$\frac{1}{2}$	0	0	0
T_3	$\frac{1}{2}$	$-\frac{1}{2}$	$\frac{1}{2}$	$-\frac{1}{2}$	0	0	0
$\frac{Y}{2}$	$-\frac{1}{2}$	$-\frac{1}{2}$	$\frac{1}{6}$	$\frac{1}{6}$	-1	$\frac{2}{3}$	$-\frac{1}{3}$
Q	0	-1	$\frac{2}{3}$	$-\frac{1}{3}$	-1	$\frac{2}{3}$	$-\frac{1}{3}$

Table 1: Weak quantum numbers for the quarks and leptons in a single generation. The symbol T denotes the weak isospin, T_3 is the third component of T, Y is the hypercharge, and Q is the electric charge.

1.1.1.3 SM Higgs sector

In the SM, a set of complex scalar fields is introduced as an $SU(2)$ doublet

$$\phi = \begin{pmatrix} \phi^+ \\ \phi^0 \end{pmatrix},$$

whose self-interactions generate the mass terms for the gauge and fermion fields via spontaneous symmetry breaking (SSB). This $SU(2)$ doublet is called "Higgs doublet" since it gives rise to the only scalar particle in SM, *i.e.* the Higgs boson. The electroweak quantum numbers of the complex fields ϕ^+ and ϕ^0 are listed in Table. 2.

	T	T_3	$\frac{Y}{2}$	Q
ϕ^+	$\frac{1}{2}$	$\frac{1}{2}$	$\frac{1}{2}$	1
ϕ^-	$\frac{1}{2}$	$-\frac{1}{2}$	$\frac{1}{2}$	0

Table 2: Weak quantum numbers for ϕ^+ and ϕ^0. The symbol T denotes the weak isospin, T_3 is the third component of T, Y is the hypercharge, and Q is the electric charge.

The Higgs sector of the SM Lagrangian is

$$\mathcal{L}_{\text{Higgs}} = (D^\mu \phi)^\dagger D_\mu \phi - V(\phi), \quad V(\phi) = \mu^2 |\phi|^2 + \lambda |\phi|^4, \tag{24}$$

where $V(\phi)$ is the renormalizable Higgs potential, and

$$D_\mu \phi = \left(\partial_\mu + i g \tau^i W^i_\mu + \frac{i g'}{2} B_\mu \right) \phi. \tag{25}$$

For $\mu^2 < 0$, the neutral component ϕ^0 develops a vacuum expectation value (vev) v so that

$$v = \sqrt{-\frac{\mu^2}{\lambda}}, \quad \langle \phi \rangle_0 \equiv \langle 0 \,|\, \phi \,|\, 0 \rangle = \begin{pmatrix} 0 \\ v/\sqrt{2} \end{pmatrix}. \tag{26}$$

In order to separate out the vev, we redefine the Higgs doublet in the "radial representation" as

$$\phi = \exp\big(i \tau^i \xi_i(x)\big) \begin{pmatrix} 0 \\ (v + H(x))/\sqrt{2} \end{pmatrix}, \tag{27}$$

where the real scalar fields $\xi_1(x)$, $\xi_2(x)$, $\xi_3(x)$ and $H(x)$ contain zero vev. It is convenient to remove the overall phase factor by making an $SU(2)$ gauge transformation

$$\phi(x) \to \exp\big(-i\tau^i\xi_i(x)\big)\phi(x) = \begin{pmatrix} 0 \\ (v+H(x))/\sqrt{2} \end{pmatrix} \tag{28}$$

to move $\phi(x)$ into the "unitary gauge". Applying the covariant derivative to $\phi(x)$ then gives

$$\begin{aligned} D_\mu\phi &= \frac{1}{\sqrt{2}}\left[\partial_\mu + \frac{ig}{\sqrt{2}}(\tau^+W_\mu^+ + \tau^-W_\mu^-) + ieQA_\mu + ig_Z Z_\mu(\tau^3 - \sin^2\theta_W Q)\right]\begin{pmatrix} 0 \\ v+H(x) \end{pmatrix} \\ &= \frac{1}{\sqrt{2}}\begin{pmatrix} igW_\mu^+(v+H(x))/\sqrt{2} \\ \partial_\mu H(x) - ig_Z Z_\mu(v+H(x))/2 \end{pmatrix}. \end{aligned} \tag{29}$$

The kinetic term in $\mathcal{L}_{\text{Higgs}}$ then gives rise to the weak gauge boson mass terms and the three-point and four-point interaction terms

$$\begin{aligned} (D^\mu\phi)^\dagger D_\mu\phi = &\ \frac{1}{2}\begin{pmatrix} -gW^{\mu-}(v+H(x))/\sqrt{2} \\ \partial^\mu H(x) + ig_Z Z^\mu(v+H(x))/2 \end{pmatrix}^T \begin{pmatrix} igW_\mu^+(v+H(x))/\sqrt{2} \\ \partial_\mu H(x) - ig_Z Z_\mu(v+H(x))/2 \end{pmatrix}, \\ = &\ \frac{1}{2}\partial^\mu H\partial_\mu H + m_W^2 W^{\mu-}W_\mu^+ + \frac{1}{2}m_Z^2 Z^\mu Z_\mu + gm_W W^{\mu-}W_\mu^+ H \\ &+ g_Z m_Z Z^\mu Z_\mu + \frac{g^2}{4}W^{\mu-}W_\mu^+ HH + \frac{g_Z^2}{8}Z^\mu Z_\mu HH, \end{aligned} \tag{30}$$

where

$$m_W = \frac{1}{2}gv, \quad m_Z = \frac{1}{2}g_Z v = \frac{m_W}{\cos\theta_W}. \tag{31}$$

After the discovery of $W^\pm$ and Z boson at the CERN Super Proton Synchrotron in 1983, the masses of $W^\pm$ and Z have been measured very precisely. The current world average values are [1]

$$m_W = 80.379 \pm 0.012 \text{ GeV}, \quad m_Z = 91.1876 \pm 0.0021 \text{ GeV} \tag{32}$$

Using relation in Eq. (31), we can relate vev to the Fermi constant G_F [1]

$$\frac{G_F}{\sqrt{2}} = \frac{g^2}{8m_W^2} \quad \Rightarrow \quad v = \sqrt{\sqrt{G_F}} \sim= 246 \text{ GeV}. \tag{33}$$

---

[1] $G_F = 1.1663787(6) \times 10^{-5}$ GeV^{-2} is derived from the muon lifetime measurement [1].

The Higgs mass term and its self-interaction terms are contained in the Higgs potential

$$\begin{aligned} V(\phi) &= \frac{\mu^2}{2}(v+H)^2 + \frac{\lambda}{4}(v+H)^4 \quad (34)\\ &= \frac{1}{2}m_H^2 H^2 + \sqrt{\frac{\lambda}{2}} m_H H^3 + \frac{\lambda}{4}H^4 - \frac{\lambda v^4}{4}, \quad (35)\end{aligned}$$

where the Higgs mass is

$$m_H = v\sqrt{2\lambda} = \sqrt{2}|\mu|. \quad (36)$$

The Higgs boson was discovered by the ATLAS and CMS group at the CERN Large Hadron Collider (LHC) in 2012 [2, 3]. The present most precise measurement of Higgs mass is given by the CMS group [4]

$$m_H = 125.38 \pm 0.14 \text{ GeV}. \quad (37)$$

1.1.1.4 SM Yukawa sector

In the SM, the fermions acquire their masses through their Yukawa couplings to the scalars. The Lagrangian of the SM Yukawa sector reads

$$\mathcal{L}_{\text{Yukawa}} = -\sum_{i,j=1}^{3}\left(y_{ij}^u \overline{Q}_{Li}\tilde{\phi}u_{Rj} + y_{ij}^d \overline{Q}_{Li}\phi d_{Rj} + y_{ij}^e \overline{L}_{Li}\phi e_{Rj}\right) + h.\,c., \quad (38)$$

where we have allowed inter-generation couplings, i, j are indices for the generations and $\tilde{\phi}$ is the conjugate of the Higgs doublet ϕ that satisfies

$$\tilde{\phi} = i\sigma_2\phi^* = \begin{pmatrix} \phi^{0*} \\ -\phi^- \end{pmatrix}.$$

For simplicity, we now consider the Yukawa Lagrangian that involves leptons in a single generation, *e.g.* electron

$$\begin{aligned} \mathcal{L}_{\text{Yukawa}} &\supset -y_e\overline{L}_L\phi e_R + h.\,c. \\ &= -\frac{y_e}{\sqrt{2}}(v+H)(\bar{e}_L e_R + \bar{e}_R e_L) \\ &= -\frac{y_e v}{\sqrt{2}}\bar{e}e - \frac{y_e}{\sqrt{2}}H\bar{e}e. \quad (39)\end{aligned}$$

The first term in the last line of Eq. (39) is the mass term of electron

$$m_e = \frac{y_e v}{\sqrt{2}}, \tag{40}$$

that given by the Higgs vev.

The SM mass generation mechanism for the quarks is similar to the lepton case, but a little bit more complicated since the three generations should be considered together. The Yukawa interaction in the Lagrangian

$$\mathcal{L}_{\text{Yukawa}} \supset -\sum_{i,j=1}^{3} \left(y_{ij}^u \overline{Q}_{Li} \tilde{\phi} u_{Rj} + y_{ij}^d \overline{Q}_{Li} \phi d_{Rj} \right) + h.\,c., \tag{41}$$

depends on 18 complex coupling parameters in y_{ij}^u and y_{ij}^d. The up-type and down-type quarks acquire their mass terms from the vev of ϕ and $\tilde{\phi}$ as

$$\mathcal{L}_{\text{Yukawa}} \supset -\left(\bar{u}_1, \bar{u}_2, \bar{u}_3\right)_R \mathcal{M}^u \begin{pmatrix} u_1 \\ u_2 \\ u_3 \end{pmatrix}_L - \left(\bar{d}_1, \bar{d}_2, \bar{d}_3\right)_R \mathcal{M}^d \begin{pmatrix} d_1 \\ d_2 \\ d_3 \end{pmatrix}_L + h.\,c., \tag{42}$$

where the quark mass matrices in generation space are written as

$$\mathcal{M}_{ij}^u = \frac{v}{\sqrt{2}} y_{ij}^u, \quad \mathcal{M}_{ij}^d = \frac{v}{\sqrt{2}} y_{ij}^d. \tag{43}$$

In order to find the quark mass eigenstates, we need to define unitary transformations

$$\begin{pmatrix} u_1 \\ u_2 \\ u_3 \end{pmatrix}_{L,R} = U_{L,R} \begin{pmatrix} u \\ c \\ t \end{pmatrix}_{L,R}, \quad \begin{pmatrix} d_1 \\ d_2 \\ d_3 \end{pmatrix}_{L,R} = D_{L,R} \begin{pmatrix} d \\ s \\ b \end{pmatrix}_{L,R} \tag{44}$$

where u, d, c, s, t, b are the quark mass eigenstates. The two complex matrices $\mathcal{M}_{ij}^u$ and $\mathcal{M}_{ij}^d$ can then be diagonalized as

$$U_R^{-1} \mathcal{M}^u U_L = \begin{pmatrix} m_u & 0 & 0 \\ 0 & m_c & 0 \\ 0 & 0 & m_t \end{pmatrix}, \quad D_R^{-1} \mathcal{M}^d D_L = \begin{pmatrix} m_d & 0 & 0 \\ 0 & m_s & 0 \\ 0 & 0 & m_b \end{pmatrix}. \tag{45}$$

1.1.1.5 Quark mass mixing and the Cabibbo–Kobayashi–Maskawa matrix

In the charged current weak interaction part in Eq. (14), we encounter the sum of quark bilinear terms

$$\begin{aligned}\sum_{\ell=1}^{3} \bar{u}_{L\ell}\gamma^\mu d_{L\ell} &= (\bar{u}_1, \bar{u}_2, \bar{u}_3)_L\, \gamma^\mu \begin{pmatrix} d_1 \\ d_2 \\ d_3 \end{pmatrix}_L = (\bar{u}, \bar{c}, \bar{t})_L\, U_L^\dagger \gamma^\mu D_L \begin{pmatrix} d \\ s \\ b \end{pmatrix}_L \\ &= (\bar{u}, \bar{c}, \bar{t})_L\, \gamma^\mu V \begin{pmatrix} d \\ s \\ b \end{pmatrix}_L ,\end{aligned} \tag{46}$$

where

$$V \equiv U_L^\dagger D_L \tag{47}$$

is the Cabibbo–Kobayashi–Maskawa (CKM) matrix that describes the generation mixing of the mass eigenstates. It is straightforward to show that the CKM matrix is unitary

$$V^\dagger V = \left(U_L^\dagger D_L\right)^\dagger \left(U_L^\dagger D_L\right) = D_L^\dagger U_L U_L^\dagger D_L = 1, \tag{48}$$

so that it can be parametrized using three angles and a phase factor as

$$\begin{aligned} V_{\text{CKM}} &= \begin{pmatrix} V_{ud} & V_{us} & V_{ub} \\ V_{cd} & V_{cs} & V_{cb} \\ V_{td} & V_{ts} & V_{tb} \end{pmatrix} \\ &= \begin{pmatrix} 1 & 0 & 0 \\ 0 & \cos\theta_{23} & \sin\theta_{23} \\ 0 & -\sin\theta_{23} & \cos\theta_{23} \end{pmatrix} \begin{pmatrix} \cos\theta_{13} & 0 & \sin\theta_{13}e^{-i\delta_{13}} \\ 0 & 1 & 0 \\ -\sin\theta_{13}e^{i\delta_{13}} & 0 & \cos\theta_{13} \end{pmatrix} \begin{pmatrix} \cos\theta_{12} & \sin\theta_{12} & 0 \\ -\sin\theta_{12} & \cos\theta_{12} & 0 \\ 0 & 0 & 0 \end{pmatrix} .\end{aligned}$$

The non-zero phase δ_{13} in the CKM matrix indicates the CP violation in the SM weak interaction.

In the neutral current weak interaction part of Eq. (14), there exist terms such as

$$\sum_{\ell=1}^{3}\bar{u}_{L\ell}\gamma^{\mu}u_{L\ell} = (\bar{u}_1,\bar{u}_2,\bar{u}_3)_L\,\gamma^{\mu}\begin{pmatrix}u_1\\u_2\\u_3\end{pmatrix}_L = (\bar{u},\bar{c},\bar{t})_L\,U_L^{\dagger}\gamma^{\mu}U_L\begin{pmatrix}u\\c\\t\end{pmatrix}_L . \tag{49}$$

The fact $U_L^{\dagger}U_L = 1$ forbids the mixing between generations. Similarly, the bilinear terms for U_R and $d_{L,R}$ are also unmixed. As a result, there is no flavor change neutral current (FCNC) at tree level in the SM.

1.2 Relativistic kinematics and phase space

1.2.1 Relativistic kinematics

In collider physics studies, we explore the phenomena of particle collisions at very high energies, where the beam particles are ultra-relativistic. Consider a particle with mass m moving in an inertial frame $\mathcal{O}$ with momentum $\vec{p}$, then its four dimensional momentum is written as

$$p \equiv p^{\mu} = (E,\vec{p}), \tag{50}$$

and the mass obeys the on-shell condition

$$p^2 \equiv p^{\mu}p_{\mu} = E^2 - \vec{p}\cdot\vec{p} = m^2. \tag{51}$$

Furthermore, the particle's velocity (in unit of the speed of light c) is defined as

$$\vec{\beta} \equiv \frac{\vec{v}}{c} = \frac{\vec{p}}{E}\ \ (-1 \le \beta \le 1), \quad \gamma \equiv \frac{1}{\sqrt{1-\beta^2}} = \frac{E}{m}. \tag{52}$$

Usually, we need to study the particle in another frame. Consider a frame $\mathcal{O}'$ that is moving alone the $\hat{z}$ direction with respect to $\mathcal{O}$ with a relative velocity β_0. The four-momentum of the particle in these two frames are related using Lorentz boost

$$\begin{pmatrix}E'\\p'_z\end{pmatrix} = \begin{pmatrix}\gamma_0 & -\gamma_0\beta_0\\-\gamma_0\beta_0 & \gamma_0\end{pmatrix}\begin{pmatrix}E\\p_z\end{pmatrix} = \begin{pmatrix}\cosh y_0 & -\sinh y_0\\-\sinh y_0 & \cosh y_0\end{pmatrix}\begin{pmatrix}E\\p_z\end{pmatrix}, \tag{53}$$

where y_0 is the rapidity of the moving $\mathcal{O}'$

$$y_0 = \frac{1}{2} \ln \frac{1+\beta_0}{1-\beta_0}, \quad (-\infty < y_0 < \infty). \tag{54}$$

More generally, if the frame $\mathcal{O}'$ is moving in an arbitrary direction $\vec{\beta}_0$, measurements of a Lorentz covariant four-vector X in the two frames can be related by $X' = B(\vec{v})X$, and the boost $B(\vec{v})$ between the unprimed and primed frames is

$$B(\vec{v}) = \begin{pmatrix} \gamma_0 & -\gamma_0\beta_{0,x} & -\gamma_0\beta_{0,y} & -\gamma_0\beta_{0,z} \\ -\gamma_0\beta_{0,x} & 1+(\gamma-1)\beta_{0,x}^2/\beta_0^2 & (\gamma-1)\beta_{0,x}\beta_{0,y}/\beta_0^2 & (\gamma-1)\beta_{0,x}\beta_{0,z}/\beta_0^2 \\ -\gamma_0\beta_{0,y} & (\gamma-1)\beta_{0,y}\beta_{0,x}/\beta_0^2 & 1+(\gamma-1)\beta_{0,y}^2/\beta_0^2 & (\gamma-1)\beta_{0,y}\beta_{0,z}/\beta_0^2 \\ -\gamma_0\beta_{0,z} & (\gamma-1)\beta_{0,z}\beta_{0,x}/\beta_0^2 & (\gamma-1)\beta_{0,z}\beta_{0,y}/\beta_0^2 & 1+(\gamma-1)\beta_{0,z}^2/\beta_0^2 \end{pmatrix}, \tag{55}$$

with $\beta_0 = \sqrt{\beta_{0,x}^2 + \beta_{0,y}^2 + \beta_{0,z}^2}$. The above transformations are particularly useful when we need to boost the momentum of a decay product from the parent rest frame ($\mathcal{O}'$) to the lab frame ($\mathcal{O}$). In this case, the relative velocity $\vec{\beta}_0$ is given by the velocity of the parent particle

$$\vec{\beta}_0 = \vec{\beta}_{\text{parent}} = \vec{p}_{\text{parent}}/E_{\text{parent}} \tag{56}$$

For two-body processes, the Källen kinematic function, which is also known as the "basic three-particle kinematic function"

$$\lambda(x,y,z) = (x-y-z)^2 - 4yz = x^2 + y^2 + z^2 - 2xy - 2xz - 2yz \tag{57}$$

is widely used. This "λ function" is also called "triangle function", since $\sqrt{-\lambda(x,y,z)}/4$ equals to the area of a triangle whose three sides are $\sqrt{x}$, $\sqrt{y}$, and $\sqrt{z}$. Consider a two-particle final state with the momenta $\vec{p}_1$, $\vec{p}_2$, the energies and the magnitudes of $\vec{p}_1$, $\vec{p}_2$ in the center of momentum frame are

$$|\vec{p}_1|^{\text{cm}} = |\vec{p}_2|^{\text{cm}} = \frac{\lambda^{1/2}(s, m_1^2, m_2^2)}{2\sqrt{s}}, \quad E_1^{\text{cm}} = \frac{s + m_1^2 - m_2^2}{2\sqrt{s}}, \quad E_2^{\text{cm}} = \frac{s + m_2^2 - m_1^2}{2\sqrt{s}}, \tag{58}$$

where $s = (p_1 + p_2)^2$. It is useful to express the two-body kinematics by some Lorentz invariant variables. For a $2 \to 2$ process

$$p_A + p_B \to p_1 + p_2, \tag{59}$$

there are three Lorentz-invariant "Mandelstam variables" defined as

$$s = (p_A + p_B)^2 = (p_1 + p_2)^2 = E_{\rm cm}^2, \tag{60}$$

$$t = (p_A - p_1)^2 = (p_B - p_2)^2 = m_A^2 + m_1^2 - 2(E_A E_1 - p_A p_1 \cos\theta_{A1}), \tag{61}$$

$$u = (p_A - p_2)^2 = (p_B - p_1)^2 = m_A^2 + m_2^2 - 2(E_A E_2 - p_A p_2 \cos\theta_{A2}), \tag{62}$$

where E_{cm} denotes the "center of momentum energy", θ_{A1} (θ_{A2}) is the angle between p_A and p_1 (p_2).

1.2.2 Phase space

One of the far-reaching concepts in high energy physics is phase space (PS), which is the set of all possible configurations that a system may exist according to the corresponding conservation law. The Lorentz invariant phase space of an n-particle final state is written as

$$\mathrm{dPS}_n \equiv (2\pi)^4 \delta^4\left(P - \sum_{i=1}^{n} p_i\right) \prod_{i=1}^{n} \frac{\mathrm{d}^3\vec{p}_i}{(2\pi)^3 2E_i}, \tag{63}$$

where P is the total momentum of the initial state and δ-function constrains the phase space to satisfy the four-momentum conservation. All the final state particles are required to be on shell, *i.e.* $p_i^2 = m_i^2$.

1.2.2.1 One body phase space

The phase space element for one-particle final state is quite special, for the invariant mass of the final state particle is forced to equal the total c.m. energy by momentum conservation. Consider a one-particle state with four-momentum p_1 and mass m_1, the phase space integral follows

$$\int \mathrm{dPS}_1 = (2\pi)^4 \int \frac{\mathrm{d}^3\vec{p}_1}{(2\pi)^3 2E_1} \delta^4(P - p_1). \tag{64}$$

Making use of the relation

$$\int \frac{\mathrm{d}^3\vec{p}}{2E} = \int \mathrm{d}^4 p \; \delta(p^2 - m^2), \tag{65}$$

we can write the one-body phase space integral as

$$\int \mathrm{dPS}_1 = 2\pi \int \mathrm{d}^4 p \; \delta(p_1^2 - m_1^2)\delta^4(P - p_1) = 2\pi\delta(s - m_1^2), \tag{66}$$

hence we know the "phase-space volume" of one-particle state is 2π.

1.2.2.2 Two body phase space

For a two-body final state system with four-momenta p_1 and p_2, the Lorentz-invariant phase space is

$$\int \mathrm{dPS}_2 = (2\pi)^4 \int \frac{\mathrm{d}^3\vec{p}_1}{(2\pi)^3 2E_1} \frac{\mathrm{d}^3\vec{p}_2}{(2\pi)^3 2E_2} \delta^4(P - p_1 - p_2). \tag{67}$$

Without loss of generality, one can integrate over p_2 and have

$$\begin{aligned} \int \mathrm{dPS}_2 &= \int \frac{\mathrm{d}^3\vec{p}_1}{(2\pi)^3 2E_1 2E_2} 2\pi \; \delta(\sqrt{s} - E_1 - E_2), & (68) \\ &= \int \frac{1}{(4\pi)^2} \frac{|\vec{p}_1|^{\mathrm{cm}}}{\sqrt{s}} \mathrm{d}\Omega = \int \frac{1}{(4\pi)^2} \frac{|\vec{p}_1|^{\mathrm{cm}}}{\sqrt{s}} \mathrm{d}\cos\theta \; \mathrm{d}\phi. & (69) \end{aligned}$$

Taking Eq. (58), the above expression can be written as

$$\mathrm{dPS}_2 = \frac{1}{(4\pi)^2} \frac{1}{2} \lambda^{1/2}(1, \frac{m_1^2}{s}, \frac{m_2^2}{s}) \mathrm{d}\cos\theta \; \mathrm{d}\phi \tag{70}$$

One important tool in collider phenomenology studies is numerical simulation using Monte Carlo (MC) integration. In order to implement the MC approach, we define x_1, x_2 so that

$$\cos\theta = 2x_1 - 1, \quad \phi = 2\pi y_2, \quad x_1, x_2 \in [0, 1], \tag{71}$$

to rescale the integration variables, and thus

$$\mathrm{dPS}_2 = \frac{1}{4\pi} \frac{1}{2} \lambda^{1/2}(1, \frac{m_1^2}{s}, \frac{m_2^2}{s}) \mathrm{d}x_1 \; \mathrm{d}x_2. \tag{72}$$

The phase-space volume of a two-particle final state system is scaled down with respect to that of a one-particle final state by

$$\frac{\mathrm{dPS}_2}{s \; \mathrm{dPS}_1} = \frac{1}{(4\pi)^2}. \tag{73}$$

1.2.2.3 Three body phase space

Given a three-particle final state with momenta $\vec{p}_1$, $\vec{p}_2$, and $\vec{p}_3$, the phase space integral is written as

$$\int \mathrm{dPS}_3 = (2\pi)^4 \int \frac{\mathrm{d}^3\vec{p}_1}{(2\pi)^3 2E_1} \frac{\mathrm{d}^3\vec{p}_2}{(2\pi)^3 2E_2} \frac{\mathrm{d}^3\vec{p}_3}{(2\pi)^3 2E_3} \delta^4(P - p_1 - p_2 - p_3) \tag{74}$$

Also integrating over p_3 using the δ-function, the phase space element is given by

$$\mathrm{dPS}_3 = \frac{1}{(2\pi)^3} \delta(\sqrt{s} - E_1 - E_2 - E_3) \frac{|\vec{p}_1|^2 \mathrm{d}|\vec{p}_1|}{2E_1} \frac{|\vec{p}_2^{(23)}|^2 \mathrm{d}|\vec{p}_2^{(23)}|}{2E_2^{(23)} 2E_3^{(23)}}. \tag{75}$$

The upper index "(23)" indicates the variable is in the p_{23}-frame, satisfying the relations

$$\begin{aligned} m_{23} &\equiv \sqrt{p_{23}^2} - E_{23} = E_2^{(23)} + E_3^{(23)}, & (76)\\ \mathrm{d}E_{23} &= |\vec{p}_2^{(23)}| \left(\frac{m_{23}}{E_2^{(23)} E_3^{(23)}} \right) \mathrm{d}|\vec{p}_2^{(23)}|, & (77)\\ |\vec{p}_2^{(23)}| &= \frac{m_{23}}{2} \lambda^{1/2} \left(1, \frac{m_2^2}{m_{23}^2}, \frac{m_3^2}{m_{23}^2} \right). & (78) \end{aligned}$$

With appropriate substitutions to Eq. (75), we have

$$\mathrm{dPS}_3 = \frac{1}{(4\pi)^5} 2|\vec{p}_1| \mathrm{d}E_1 \mathrm{d}\Omega_1 \mathrm{d}\Omega_2 \; \lambda^{1/2} \left(1, \frac{m_2^2}{m_{23}^2}, \frac{m_3^2}{m_{23}^2} \right). \tag{79}$$

In the c.m. frame, the maximum values of energy and momentum for particle 1 are

$$E_1^{\max} = \frac{s + m_1^2 - (m_2 + m_3)^2}{2\sqrt{s}}, \quad |\vec{p}_1|^{\max} = \frac{\lambda^{1/2}(s, m_1^2, (m_2 + m_3)^2)}{2\sqrt{s}}. \tag{80}$$

Similar to the two-body case, we need to rescale the variables to implement the MC integration by introducing $x_1 \dots x_5 \in [0, 1]$ so that

$$E_1 = (E_1^{\max} - m_1) y_1 + m_1, \;\; \cos\theta_1 = 2x_2 - 1, \;\; \phi_1 = 2\pi x_3, \;\; \cos\theta_2 = 2x_4 - 1, \;\; \phi_2 = 2\pi x_5. \tag{81}$$

The three-body phase space integral then simplifies to

$$\int \mathrm{dPS}_3 = \int \mathrm{d}x_1 \mathrm{d}x_2 \mathrm{d}x_3 \mathrm{d}x_4 \mathrm{d}x_5 \frac{E_1^{\max} - m_1}{(4\pi)^3} 2|\vec{p}_1| \; \lambda^{1/2} \left(1, \frac{m_2^2}{m_{23}^2}, \frac{m_3^2}{m_{23}^2} \right). \tag{82}$$

1.2.2.4 Recursion relation for the phase space element

One useful property of phase space is that one can decompose an n-body phase space into smaller ones, which makes automated MC event generator possible. The recursion relation states that the n-body phase space element is equivalent to the product of an $(n-1)$-body phase space element and a two-body phase space element

$$\mathrm{dPS}_n(P;p_1,\dots p_n)=\mathrm{dPS}_{n-1}(P;p_1,\dots p_{n-1,n})\mathrm{dPS}_2(p_{n-1,n};p_{n-1},\dots p_n)\frac{\mathrm{d}m^2_{n-1,n}}{2\pi}, \tag{83}$$

where

$$m_{n-1}+m_n\leq m_{n-1,n}\leq\sqrt{s}-\sum_{i=1}^{n-2}m_i \tag{84}$$

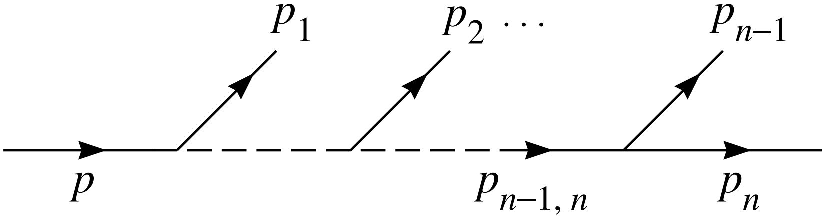

Figure 2: Illustration for the recursion relation that relates an n-body phase space element to the product of a two-body phase space element and an $(n-1)$ one. This figure is adopted from Ref. [5].

Here we show two examples of applying the recursion relation on three-body and four-body phase space integrals respectively. A three-body phase space element can be decomposed into a product of two two-body ones

$$\mathrm{dPS}_3(P;p_1,p_2,p_3)=\mathrm{dPS}_2(P;p_1,p_{23})\mathrm{dPS}_2(p_{23};p_2,p_3)\frac{\mathrm{d}m^2_{23}}{2\pi}, \tag{85}$$

where

$$m_2+m_3\leq m_{23}\leq\sqrt{s}-m_1. \tag{86}$$

For the four-body case, the recursion relation is

$$\mathrm{dPS}_4(P;p_1,p_2,p_3,p_4) = \mathrm{dPS}_3(P;p_1,p_2,p_{34})\mathrm{dPS}_2(p_{34};p_3,p_4)\frac{\mathrm{d}m_{34}^2}{2\pi}, \tag{87}$$

$$= \mathrm{dPS}_2(P;p_1,p_{234})\mathrm{dPS}_2(p_{234};p_2,p_{34})\mathrm{dPS}_2(p_{34};p_3,p_4)\frac{\mathrm{d}m_{234}^2}{2\pi}\frac{\mathrm{d}m_{34}^2}{2\pi}, \tag{88}$$

with

$$m_2 + m_{34} \leq m_{234} \leq \sqrt{s} - m_1, \quad m_3 + m_4 \leq m_{34} \leq \sqrt{s} - (m_1 + m_2). \tag{89}$$

1.2.3 Cross section and decay width

In high-energy colliders, antiparallel particle beams *e.g.* proton-proton beams or lepton-lepton beams, are focused onto each other to make high-energy scattering processes happen. One important parameter for a given collider is the number of particles passing each other per unit time through unit transverse area at the collision point, which is known as the instantaneous luminosity $\mathcal{L}$. The number of scattering events $\mathcal{N}$ at a particular scattering energy $\sqrt{s}$ is given by

$$\mathcal{N}(s) = \sigma(s)\mathcal{L}, \tag{90}$$

where $\sigma(s)$ is the corresponding cross section at $\sqrt{s}$. For a given luminosity, the cross section can be interpreted as a measure of the likelihood for a particular scattering process to occur.

In general, a cross section is given by

$$\sigma = \frac{\text{Number of events}}{\text{Incoming particle flux}} = \frac{\text{Scattering likelihood}}{(\text{Number density}) \times (\text{Relative velocity})}. \tag{91}$$

The numerator of the above expression is the matrix element square summed over final state degrees of freedom. For an arbitrary $2 \to n$ scattering process, $A+B \to X$, the cross section can be written as

$$\sigma(A+B \to X) = \int \mathrm{dPS}_n \frac{\mathrm{d}\sigma}{\mathrm{dPS}_n} = \frac{1}{2\lambda^{1/2}(s,m_A^2,m_B^2)} \int \mathrm{dPS}_n \overline{|\mathcal{M}(A+B \to X)|^2}, \tag{92}$$

where λ is the Källen kinematic function and the symbol $\overline{|\mathcal{M}|^2}$ denotes that the sum over final state degrees of freedom and average over the initial ones are already done.

Heavy unstable particles can be produced in high-energy collisions. The decay width of an unstable particle A into a particular final state f is called “partial width”. Assume A is unpolarized, then its partial width $\Gamma(A \to f)$ is given by

$$\Gamma(A \to f) = \frac{1}{2m_A} \int \mathrm{dPS}_n \overline{|\mathcal{M}(A \to f)|^2}. \tag{93}$$

Again, the sum over final state degrees of freedom and average over the initial ones are absorbed into the symbol $\overline{|\mathcal{M}|^2}$. The sum of all allowed partial widths of A gives the “total decay width”

$$\Gamma^A_{\text{Tot.}} \equiv \sum_f \Gamma(A \to f), \tag{94}$$

which is related to A's mean lifetime τ_A via

$$\tau_A = \frac{1}{\Gamma^A_{\text{Tot.}}}. \tag{95}$$

The fraction of times that a particle decays through an individual decay mode is called “branching fraction” (BR)

$$\mathrm{BR}(A \to f) \equiv \frac{\Gamma(A \to f)}{\Gamma^A_{\text{Tot.}}}. \tag{96}$$

2.0 Electroweak parton distribution functions

For collisions that happen well above the electroweak scale, all the SM particles should be treated as "partons" and be described using the electroweak parton distribution functions. In this chapter, we will start from the existing "equivalent photon approximation" and "effective weak boson approximation" to draw the partonic picture at high-energy colliders. We will then introduce the electroweak parton distribution functions formalism at the Leading-Log accuracy. The results in this chapter have been published on Ref. [6, 7].

2.1 Approximations at the leading order

2.1.1 Equivalent photon approximation

One of the central talent of perturbative QCD is to factorize the scattering amplitudes into a product of process-independent terms (the parton distribution functions) and the process-dependent hard scattering cross section. In this section, we will show that the collinear photon emission results into an analogue of a parton distribution function (PDF), which is very helpful to understand the method of factorization and the parton picture of high-energy collisions.

For a general example, we take the scattering process of a fermion $f(p_A)$ with an arbitrary initial state $X(p_B)$ as shown in Fig. 3

$$f(p_A) + X(p_B) \to f(p_1) + \gamma^*(q) + X(p_B) \to f(p_1) + Y, \tag{97}$$

which contains the "partonic hard process"

$$\gamma^*(q) + X(p_B) \to Y, \quad q = p_A - p_1. \tag{98}$$

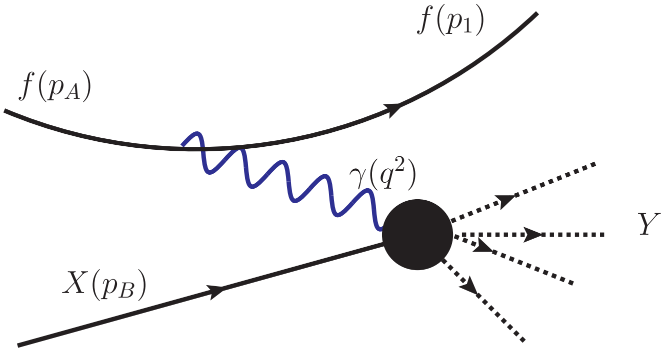

Figure 3: Diagrammatic representation of $fX \to X\gamma^* \to fY$ scattering.

The Feynman amplitude of the above fX scattering process can be written as

$$\begin{aligned}
\mathcal{M} &= J^\mu(f \to f\gamma^*)\frac{-ig_{\mu\nu}}{q^2}J^\nu(\gamma^* X \to Y), && (99)\\
&\to \frac{(-ieq_f)}{q^2}\bar{u}(p_1)\gamma^\mu u(p_A)\left(\sum_\lambda \epsilon^*_\mu(q,\lambda)\epsilon_\nu(q,\lambda)\right) J^\nu(\gamma^* X \to Y), && (100)\\
&= \frac{(-ieq_f)}{q^2}\sum_\lambda \left[\bar{u}(p_1)\not{\epsilon}^* u(p_A)\right]\left[\epsilon \cdot J(\gamma X \to Y)\right], && (101)\\
&= \frac{(-ieq_f)}{q^2}\sum_\lambda \mathcal{M}(f \to f\gamma)\mathcal{M}(\gamma X \to Y), && (102)
\end{aligned}$$

where q_f is the electric charge of the initial state fermion, $\mathcal{M}(f \to f\gamma)$ is the Feynman amplitude for the $f \to f\gamma$ splitting, and $\mathcal{M}(\gamma X \to Y)$ is the Feynman amplitude of the photon initialized process defined in Eq. (98). In Eq. (100), we took the on-shell limit of the photon and used the replacement

$$\frac{-ig_{\mu\nu}}{q^2} \to \frac{+i}{q^2}\sum_\lambda \epsilon^*_\mu(q,\lambda)\epsilon_\nu(q,\lambda). \qquad (103)$$

In future discussions, we would treat the photon as on-shell and write γ^* as γ since we have assumed that the dominant contribution is from the nearly on-shell photon. Now we see that the entire Feynman amplitude of fX scattering can be separated into two pieces: the $f \to f\gamma$ splitting and the $\gamma X \to Y$ scattering. The squared matrix element of fX scattering, averaged over the initial states and summed over the degree of freedom of the final state, is expressed as

$$\sum_{\text{d.o.f.}} \overline{|\mathcal{M}|^2} \to \frac{e^2 q_f^2}{q^4} \sum_{\lambda} \sum_{\text{d.o.f.}} \overline{|\mathcal{M}(f \to f\gamma)|^2}\; \overline{|\mathcal{M}(\gamma X \to Y)|^2}. \tag{104}$$

With phase space integral, the cross section is given by

$$\begin{aligned} & \sigma(fX \to fY) \\ = \;& \frac{1}{2\lambda^{1/2}(s, m_f^2, m_X^2)} \int \mathrm{dPS}_{fX\to fY} \sum_{\text{d.o.f.}} \overline{|\mathcal{M}|^2}, & (105) \\ \to \;& \frac{1}{2\lambda^{1/2}(s, m_f^2, m_X^2)} \int \mathrm{dPS}_{f\to f\gamma} \int \mathrm{dPS}_{\gamma X\to Y} \sum_{\text{d.o.f.}} \overline{|\mathcal{M}|^2}, & (106) \\ = \;& \int \frac{\mathrm{d}^3 p_1}{(2\pi)^3 2E_1} \frac{\lambda^{1/2}(\hat{s}, m_f^2, m_X^2)}{\lambda^{1/2}(s, m_f^2, m_X^2)} \sum_{\lambda} \overline{|\mathcal{M}(f \to f\gamma)|^2} \frac{e^2 q_f^2}{q^4} \hat{\sigma}(\gamma X \to Y), & (107) \end{aligned}$$

where s and $\hat{s}$ are defined as

$$s = (p_A + p_B)^2, \quad \hat{s} = (q + p_B)^2. \tag{108}$$

In the case that both s and $\hat{s}$ are much larger than the initial state particle mass m_f, the cross section can be further simplified to

$$\sigma(fX \to fY) = \int \frac{\mathrm{d}^3 p_1}{(2\pi)^3 2E_1} \frac{\hat{s}}{s} \sum_{\lambda} \overline{|\mathcal{M}(f \to f\gamma)|^2} \frac{e^2 q_f^2}{q^4} \hat{\sigma}(\gamma X \to Y). \tag{109}$$

In the $f \to f\gamma$ splitting, the two final particles are almost collinear with a very small transverse momentum. Choosing the incident fermion momentum to be along $\hat{z}$ axis and the outgoing two particle to be in the $\hat{x} - \hat{z}$ plane and setting z to be the fraction of energy of the incoming fermion carried off by the photon, we can write the 4-momenta as

$$\begin{aligned} p_A &= (E_A, 0, 0, p_A), & (110) \\ q &= (zE_A, p_T, 0, zE_A + \frac{p_T^2}{2(1-z)E_A}), & (111) \\ p_1 &= ((1-z)E_A, -p_T, 0, (1-z)E_A - \frac{p_T^2}{2(1-z)E_A}), & (112) \end{aligned}$$

and have

$$p_1^2 = 0, \quad q^2 = -\frac{p_T^2}{1-z}, \tag{113}$$

up to $\mathcal{O}(p_T^4)$. With respect to helicity conservation, we now consider a left-handed (LH) initial fermion case (so that the final state fermion is also LH)

$$i\mathcal{M} = \bar{u}_L(p_1)(-ieq_f\gamma_\mu)u_L(p_A)\epsilon_T^{*\mu}(q), \tag{114}$$

where the photon can be either LH or RH. Recall the helicity-basis formulae

$$\gamma_\mu = \begin{pmatrix} 0 & \sigma_\mu \\ \bar{\sigma}_\mu & 0 \end{pmatrix}, \qquad u_L(p_A) = \sqrt{2p_A^0}\begin{pmatrix} \xi(p_A) \\ 0 \end{pmatrix}, \tag{115}$$

we can write more explicitly

$$i\mathcal{M} = -ieq_f\sqrt{2(1-z)p_A}\sqrt{2p_A}\xi^\dagger(p_1)\sigma^i\xi(p_A)\cdot\epsilon_T^{*i}(q), \tag{116}$$

for $m_f \sim 0$, where we have used the relateion $E_A = p_A$ in the massless limit. Recall the rotation of wave functions in Appx. A, we write the LH spinors

$$\xi(p_A) = \begin{pmatrix} 0 \\ 1 \end{pmatrix}, \qquad \xi(p_1) = \begin{pmatrix} p_T/2(1-z)p_A \\ 1 \end{pmatrix}, \tag{117}$$

and the polarization vectors for the photon

$$\epsilon_L^{*i}(q) = \frac{1}{\sqrt{2}}\left(1, i, -\frac{p_T}{zp_A}\right), \qquad \epsilon_R^{*i}(q) = \frac{1}{\sqrt{2}}\left(1, -i, -\frac{p_T}{zp_A}\right). \tag{118}$$

By substituting Eqs. (117, 118) into Eq. (116), we have

$$i\mathcal{M}(f_L^- \to f_L^-\gamma_R) = ieq_f\frac{\sqrt{2(1-z)}}{z}p_T, \tag{119}$$

$$i\mathcal{M}(f_L^- \to f_L^-\gamma_L) = ieq_f\frac{\sqrt{2(1-z)}}{z(1-z)}p_T. \tag{120}$$

For parity invariance, it is straightforward to obtain

$$i\mathcal{M}(f_R^- \to f_R^-\gamma_L) = ieq_f\frac{\sqrt{2(1-z)}}{z}p_T, \tag{121}$$

$$i\mathcal{M}(f_R^- \to f_R^-\gamma_R) = ieq_f\frac{\sqrt{2(1-z)}}{z(1-z)}p_T. \tag{122}$$

Therefore, the initial polarization averaged amplitude square is

$$\sum_\lambda \overline{|\mathcal{M}|^2} = \frac{2e^2q_f^2p_T^2}{z(1-z)}\left[\frac{1+(1-z)^2}{z}\right]. \tag{123}$$

Rewrite the integral over k in Eq.(109) to isolate the collinear singularity,

$$d^3p_1 = dp_1^3 d^2p_T = p_A dz \cdot \pi dp_T^2, \tag{124}$$

so that the cross section fX scattering is

$$\begin{aligned}
\sigma(fX \to fY) &= \int \frac{p_A \mathrm{d}z \cdot \pi \mathrm{d}p_T^2}{(2\pi)^3 2(1-z)E_A} \frac{\hat{s}}{s} \frac{2e^2 q_f^2 p_T^2}{z(1-z)} \left[\frac{1+(1-z)^2}{z}\right] \frac{e^2 q_f^2}{q^4} \hat{\sigma}(\gamma X \to Y), \qquad (125)\\
&= \int_{z_{\min}}^{z_{\max}} \mathrm{d}z \int \frac{\mathrm{d}p_T^2}{p_T^2} \frac{\alpha q_f^2}{2\pi} P_{\gamma f}(z) \hat{\sigma}(\gamma X \to Y), \qquad (126)
\end{aligned}$$

where we have assumed that all masses are negligible comparing to the scattering energy so that $p_A = E_A$ and $\hat{s} = (q + p_B)^2 = 2zp_A \cdot p_B = zs$. The symbol $P_{ji}(z)$ is the so-called "splitting kernel" for $i \to j$ splitting with the energy $E_j = zE_i$ carried by particle j. The three splitting kernels in quantum electrodynamics (QED) are listed below:

$$P_{\gamma e}(z) = \frac{1+(1-z)^2}{z}, \quad P_{ee}(z) = \frac{1+z^2}{1-z}, \quad P_{e\gamma}(z) = z^2 + (1-z)^2.$$

In the above example, we notice that the cross section diverges at zero momentum transfer *i.e.* $q^2 = 0$. However, this singularity could be regulated by the fermion mass m_f, which can be seen in the photon virtuality

$$q^2 = (p_A - p_1)^2 = 2m_f^2 - E_A E_1 (1 - \beta_A \beta_1 \cos\theta), \quad \beta_{A,1} < 1. \tag{127}$$

The fermion mass m_f serves as a regulator, thus it is natrual to evolve the momentum transfer scale from $q^2 = m_f^2$ to a typical scale Q^2 and give

$$\sigma(fX \to fY) = \int_{z_{\min}}^{z_{\max}} \mathrm{d}z \frac{\alpha q_f^2}{2\pi} P_{\gamma f}(z) \log\left(\frac{Q^2}{m_f^2}\right) \hat{\sigma}(\gamma X \to Y). \tag{128}$$

This result is also known as "equivalent photon approximation" (EPA) or Weizsäicker-Williams approximation [8, 9]. A more commonly used form is

$$\sigma(fX \to fY) = \int_{z_{\min}}^{z_{\max}} \mathrm{d}z f_{\gamma/f}(z, Q^2) \hat{\sigma}(\gamma X \to Y), \tag{129}$$

where the parton distribution function (PDF) of photon

$$f_{\gamma/f}(z, Q^2) = \frac{\alpha q_f^2}{2\pi} P_{\gamma f}(z) \log\left(\frac{Q^2}{m_f^2}\right) \tag{130}$$

describes the likelihood of observing a photon in an energetic fermion f that possesses an energy fraction z of f's total energy at a momentum transfer scale Q^2. The integral limits are controlled by the relation $\hat{s} = zs$

$$z_{\max} = \frac{s}{s} = 1, \quad z_{\min} = \frac{\hat{s}_{\min}}{s}, \tag{131}$$

$z_{\min}$ is the minimum invariant mass for the partonic process $\gamma X \to Y$.

2.1.2 Effective weak boson approximation

In very high-energy collisions, where the $Q^2 \gg m_Z,\ m_W$, the W and Z bosons could also be treated as massless. Following the same procedure in the derivation of EPA, the PDFs to describe the likelihood of finding a vector boson V in a fermion f can be derived to give the "effective weak boson approximation" (EWA) [10, 11]

$$f_{V^\pm/f}(z, Q^2) = \frac{C}{16\pi^2 z}\left[(g_V \pm g_A)^2 + (g_V \mp g_A)^2(1-z)^2\right]\log\left(\frac{Q^2}{m_V^2}\right), \tag{132}$$

$$f_{V^0/f}(z) = \frac{C}{4\pi}\left(g_V^2 + g_A^2\right)\frac{1-z}{z}. \tag{133}$$

The coefficients in the above PDFs for $V = W^\pm$ are

$$C = \frac{g^2}{8}, \quad g_V = -g_A = 1, \tag{134}$$

and the ones for $V = Z$ are

$$C = \frac{g^2}{\cos^2\theta_W}, \quad g_V = \frac{1}{2}T_f^3 - Q_f\sin^2\theta_W, \quad g_A = -\frac{1}{2}T_f^3, \tag{135}$$

where $g = e/\sin\theta_W$ is the weak coupling, θ_W is the electroweek mixing angle, Q_f and T_f^3 are respectively electric charge and the third component of weak isospin for the fermion f.

2.2 Electroweak parton distribution functions

Below the EW scale $Q < M_Z$, the effects of the $\mathrm{SU}(2)_L$ gauge bosons are suppressed by g^2/M_Z^2. The gauge boson radiation off a charged lepton beam ($\ell^\pm = e^\pm, \mu^\pm$) is essentially purely electromagnetic. At the EW scale and above, all electroweak states in the unbroken SM are dynamically activated. The massless states involved at the leading order are

$$\ell_R,\ \ell_L,\ \nu_L \ \text{ and } \ B, W^{\pm,3}. \tag{136}$$

We will not include the Higgs sector in the initial state partons since the Yukawa couplings to e, μ are not relevant for the current consideration. However, we must include the effects of longitudinally polarized gauge bosons characterized by power corrections of the order M_Z^2/Q^2. Denote an EW PDF as $f_i(x, Q^2)$ with i labeling a particle with an energy fraction x at a factorization scale Q. The EW PDFs evolve according to the full EW Dokshitzer–Gribov–Lipatov–Altarelli–Parisi (DGLAP) equations [12, 13]

$$\frac{\mathrm{d} f_i}{\mathrm{d}\ln Q^2} = \sum_I \frac{\alpha_I}{2\pi} \sum_j P^I_{i,j} \otimes f_j, \tag{137}$$

where I specifies the gauge group, and the P^I_{ij} are the splitting functions for $j \to i$. The complete list of the EW splitting functions for the SM chiral states are available in listed in Appx. B and can be found in Refs. [13, 14, 15]. The initial condition for a lepton beam is $f_\ell(x, m_\ell^2) \approx \delta(1-x) + \mathcal{O}(\alpha)$ and it evolves as $\ln(Q^2/m_\ell^2)$. At the electroweak scale, the matching conditions are $f_\gamma(x, M_Z^2) \neq 0, \quad f_Z(x, M_Z^2) = 0, \quad f_{\gamma Z}(x, M_Z^2) = 0$, with a general relation

$$\begin{pmatrix} f_B \\ f_{W^3} \\ f_{BW^3} \end{pmatrix} = \begin{pmatrix} c_W^2 & s_W^2 & -c_W s_W \\ s_W^2 & c_W^2 & c_W s_W \\ 2c_W s_W & -2c_W s_W & c_W^2 - s_W^2 \end{pmatrix} \begin{pmatrix} f_\gamma \\ f_Z \\ f_{\gamma Z} \end{pmatrix},$$

where $s_W = \sin\theta_W$ is the weak mixing angle. The mixed PDF $f_{\gamma Z}$ (or f_{BW^3}) represents a mix state and is important to account for the interference between the diagrams involving γ/Z (or B/W^3) [16, 15, 13]. Chiral couplings and their RGE running are fully taken into account including the correlation between the polarized PDFs and the corresponding polarized scattering amplitudes. With one-loop virtual corrections, our results are accurate at the leading-log (LL) order. In Fig. 5(a), we present EW PDFs for the states in Eq. (136) for $\ell = \mu$ with a scale Q =3 TeV and 5 TeV. For completeness, we have also included the quarks $q = \sum_{i=d}^{t}(q_i + \bar{q}_i)$ and gluons from the higher-order splittings. We give the averaged momentum fractions $\langle xf_i \rangle = \int xf_i(x)\mathrm{d}x$ carried by various parton species in Table 3. The two scale choices lead to less than 20% difference for the EW PDFs. As expected, the fermionic states sharply peak at $x \approx 1$, while the bosonic states peak at $x \approx 0$, reflecting the infrared behavior. It is noted that there is an enhanced rate at small x for the fermions, deviating from the leading order behavior $\sim 1/(1-x)$. This is from the soft $\gamma^*/Z^*/W^*$ splitting at higher orders. Owing to the large flux of photons at low scales, the neutral EW PDFs are largest. Unlike all the other EW PDFs that scale logarithmically with Q, the longitudinal gauge bosons (W_L, Z_L) do not scale with Q at the leading order [17, 15, 13] − an explicit example for Bjorken-scaling restoration.

Q	μ	$\gamma, Z, \gamma Z$	$W^\pm$	ν	$\ell_{\rm sea}$	q	g
M_Z	97.9	2.06	0	0	0.028	0.035	0.0062
3 TeV	91.5	3.61	1.10	3.59	0.069	0.13	0.019
5 TeV	89.9	3.82	1.24	4.82	0.077	0.16	0.022

Table 3: Momentum fractions (%) carried by various parton species. The sea leptons include $\ell_{\rm sea} = \bar{\mu} + \sum_{i\neq\mu}(\ell_i + \bar{\ell}_i)$ and $\nu = \sum_i(\nu_i + \bar{\nu}_i)$. The quark components include all the 6 flavors.

2.3 The evolution of the SM electroweak parton distribution functions

In this section, we present the full DGLAP equations for the quarks and gluons coupled to the EW sector in the SM. In dealing with the full SM spectrum, the physics is characterized by two scales, namely, $\Lambda_{\rm QCD} \sim 200$ MeV and $\Lambda_{\rm EW} \sim 250$ GeV. To assure perturbativity, we take $\mu_{\rm QCD} = 0.5$ GeV, inspired by the critical scale adopted in Ref. [18]. The different choice of $\mu_{\rm QCD}$ is ascribed to the non-perturbative uncertainty. The EW threshold is taken at $\mu_{\rm EW} = M_Z$ to excite the EW gauge bosons and the top quark. We solve DGLAP equations numerically and calculate the quark and gluon PDFs of a lepton at representative factorization scales. We find substantial quark and gluon luminosities resulting from an initial electron and a muon, especially in the relatively low invariant mass region.

Different from a proton beam, the parton contents inside of a lepton can be calculated perturbatively. The evolutions of parton distribution functions (PDFs) over a factorization scale Q are governed by the well-known DGLAP equations [19, 20, 21, 22]

$$\frac{\mathrm{d}f_i}{\mathrm{d}\log Q^2} = \sum_I \frac{\alpha_I}{2\pi} \sum_j P^I_{i,j} \otimes f_j, \tag{138}$$

where the index I loops the different SM interactions. The symbol $\otimes$ stands for a convolution

$$[f \otimes g](x) = \int_0^1 \mathrm{d}\xi \mathrm{d}\zeta \delta(x - \xi\zeta) f(\xi) g(\zeta) = \int_x^1 \frac{\mathrm{d}\xi}{\xi} f(\xi) g\left(\frac{x}{\xi}\right). \tag{139}$$

$P^I_{i,j}$ are the splitting functions for $j \to i$ under the SM interaction I, and x is the momentum fraction carried by the daughter particle i. The leading order QCD and QED splitting functions are known for decades and can be found in textbooks [23, 24]. They are extended to include mixed term $\mathcal{O}(\alpha\alpha_s)$ in Ref. [25] and next-to-leading order (NLO) QED in Ref. [26]. The pure QCD splittings are known up to next-to-next-to-leading order (NNLO) [27, 28], which are employed to determine the QCD PDFs of proton in several global fitting groups [29, 30, 31, 32, 33, 34]. The QED and QED mixed evolutions are adopted to determine the photon content in Refs. [35, 36, 37]. Recently, a more precise determination of the photon PDF of a proton in terms of the electromagnetic structure functions was proposed as the LUXqed formulation [38, 39], which are employed in the global PDF analysis [40, 41, 42]. The splitting functions are extended to the EW theory to involve the EW gauge bosons and chiral states in Refs. [12, 15], which are adopted to determine the proton EW PDFs [13, 43].

As discussed in the above section, for a leptonic beam, the DGLAP evolution equations in Eq. (138) run differently in three regions of the physical scales. The initial condition starts from the lepton mass, and the QED PDFs (including the photon, charged leptons, and quarks) run in terms of the QED gauge group. Starting at μ_{QCD}, the QCD interaction begins to enter. The QCD and QED evolutions run simultaneously until μ_{EW}, where the complete SM sector begins to evolve according to the unbroken SM gauge group. In such a way, we need two matchings, at $\mu_{\rm QCD}$ and $\mu_{\rm EW}$, respectively.[1] As the QED and QCD gauge groups conserve the charge and parity symmetry, the PDFs below $\mu_{\rm EW}$ can be treated with no polarization, as long as the initial lepton beams are unpolarized. As pointed out already in Refs. [43, 6], the polarization plays an important role in the EW PDFs above the EW scale, even for the unpolarized initial beams. Consequently, the photon and gluon become polarized due to the fermion chiral interactions.

2.3.1 PDF evolution in QED and QCD

For the sake of illustration, we take the electron beam as an example. The presentation is similarly applicable to the muon beam by recognizing a different mass. In solving the QED and QCD DGLAP equations, it is customary to define the fermion PDFs in a basis of gauge singlets and non-singlets. The singlet PDFs can be defined as

$$f_L = \sum_{i=e,\mu,\tau}(f_{\ell_i}+f_{\bar{\ell}_i}),\ f_U=\sum_{i=u,c}(f_{u_i}+f_{\bar{u}_i}),\ f_D=\sum_{i=d,s,b}(f_{d_i}+f_{\bar{d}_i}), \tag{140}$$

where the subscripts refer to the fermion flavors and we have excluded the top quark below the EW scale. The DGLAP equations in Eq. (138), involving the photon and gluon, can be written as

$$\frac{\mathrm{d}}{\mathrm{d}\log Q^2}\begin{pmatrix} f_L \\ f_U \\ f_D \\ f_\gamma \\ f_g \end{pmatrix} = \begin{pmatrix} P_{\ell\ell} & 0 & 0 & 2N_\ell P_{\ell\gamma} & 0 \\ 0 & P_{uu} & 0 & 2N_u P_{u\gamma} & 2N_u P_{ug} \\ 0 & 0 & P_{dd} & 2N_d P_{d\gamma} & 2N_d P_{dg} \\ P_{\gamma\ell} & P_{\gamma u} & P_{\gamma d} & P_{\gamma\gamma} & 0 \\ 0 & P_{gu} & P_{gd} & 0 & P_{gg} \end{pmatrix} \otimes \begin{pmatrix} f_L \\ f_U \\ f_D \\ f_\gamma \\ f_g \end{pmatrix}, \tag{141}$$

where the active flavors below the EW scale are

$$N_\ell = 3,\ N_u = 2,\ N_d = 3. \tag{142}$$

---

[1] In a realistic situation, one should perform a matching whenever crossing a heavy-flavor threshold, such as at m_τ, m_c, m_b, m_t. In practice, the multiple scales make the DGLAP evolution complicated, which is beyond the scope of this work. We defer the related aspects to a future dedicated study [44]. As long as the observables under consideration are not heavy-flavor sensitive and the physical scale is well above their mass thresholds, the heavy flavors just behave similarly to the light sea flavors that are all generated dynamically. Therefore, we treat them on the equal footing classified by the matching scales $\mu_{\rm QCD}$ and $\mu_{\rm EW}$, just for simplicity.

We remind that the splitting functions $P_{q\gamma}$ and P_{qg} ($q = u, d$) contain color factor implicitly. In this work, we only consider the leading order splittings. The P_{ij} defined here include the gauge couplings α and α_s in Eq. (138), which evolve with scale as well. The initial condition for an electron beam at the leading order is

$$f_{e/e}(x, m_e^2) = f_L(x, m_e^2) = \delta(1-x), \tag{143}$$

while all the other PDFs are zero at the initial scale $Q^2 = m_e^2$.

The non-singlet PDFs can be defined as

$$\begin{aligned} f_{\ell_i}^{\rm NS} &= f_{\ell_i} - f_{\bar{\ell}_i},\ f_{\ell,12} = f_{\bar{e}} - f_{\bar{\mu}},\ f_{\ell,13} = f_{\bar{e}} - f_{\bar{\tau}}, & (144)\\ f_{u_i}^{\rm NS} &= f_{u_i} - f_{\bar{u}_i}, f_{u,12} = f_u - f_c, & (145)\\ f_{d_i}^{\rm NS} &= f_{d_i} - f_{\bar{d}_i},\ f_{d,12} = f_d - f_s,\ f_{d,13} = f_d - f_b. & (146) \end{aligned}$$

The DGLAP equations for the non-singlet PDFs are written as

$$\frac{\rm d}{{\rm d}\log Q^2} f^{\rm NS} = P_{ff} \otimes f^{\rm NS}. \tag{147}$$

where $f = \ell, u, d$. At the starting scale $Q^2 = m_e^2$, the only non-trivial non-singlet PDF is

$$f_e^{\rm NS} = f_e - f_{\bar{e}} = \delta(1-x), \tag{148}$$

while all the other non-singlet PDFs are trivially zero and remain to be zero at high scales due to the zero initial conditions.

We can now construct the PDFs for each flavor in terms of the singlet and non-singlet PDFs. The valence flavor PDF is

$$f_e = \frac{f_L + (2N_\ell - 1) f_e^{\rm NS}}{2N_\ell}, \tag{149}$$

and the sea fermion PDFs are

$$\begin{aligned} f_{\bar{e}} = f_\mu = f_{\bar{\mu}} = f_\tau = f_{\bar{\tau}} &= \frac{f_L - f_e^{\rm NS}}{2N_\ell}, & (150)\\ f_u = f_{\bar{u}} = f_c = f_{\bar{c}} &= \frac{f_U}{2N_u}, & (151)\\ f_d = f_{\bar{d}} = f_s = f_{\bar{s}} = f_b = f_{\bar{b}} &= \frac{f_D}{2N_d}. & (152) \end{aligned}$$

A few remarks are in order.

- We would like to remind the reader that the relations of the sea flavor PDFs in Eqs. (150-152) are valid only when we ignore the fermion masses in accordance with the rigorous collinear factorization. The PDFs for heavy flavors will receive threshold corrections when their masses are taken into account, as already commented on with multiple scales. This would lead to finite corrections of the order $(\alpha/2\pi)\log\big(m_f^2/m_\ell^2\big)$ to the heavy-flavor PDFs [44]. More detailed studies for the threshold matching are beyond the scope of our current interests.
- Below $\mu_{\rm QCD}$, the QCD confinement sets in. As such, the picture of "vector-meson-dominance", *e.g.* $\gamma-\rho$ mixing, gives the leading contribution to the photonic interactions, as already included in most of the photon-PDFs. It is expected to be bounded by $\alpha^2\log^2(\mu_{\rm QCD}^2/m_\ell^2)$. In our practical treatment, we only run the QED gauge group in the DGLAP evolution. The $\gamma\to q\bar{q}$ splitting serves as a source of the initial conditions of the QCD PDFs at the matching scale $\mu_{\rm QCD}$, similar to the quark-parton model Ansätze adopted in Ref. [18].
- Above $\mu_{\rm EW}$, the unbroken SM gauge interactions come into play and the PDFs receive EW corrections. The EW gauge boson W/Z and top-quark parton become active,[2] and the complete EW PDFs become polarized due to the chiral couplings, as outlined in a previous publication [6]. We will properly include the EW effects in the rest of our calculations.

2.3.2 The complete SM running above $\mu_{\rm EW}$

The QED and QCD run up to the EW scale $\mu_{\rm EW}=M_Z$. Crossing the EW threshold $\mu_{\rm EW}$, the EW gauge bosons become active, which should be taken into account as partons as well. Meanwhile, the top quark is excited as well in the $b\to Wt$ splitting. That is to say, all the $N_g=3$ generations of fermions should evolve simultaneously above the EW scale. Due to the chiral nature of the EW theory, the parton should be polarized, as the left- and right-handed fermion couple to the gauge boson differently.

---

[2] Here, we ignore the threshold correction, $\log\big(M_t^2/\mu_{\rm EW}^2\big)$, to the top-quark PDFs, which is valid as long as the physical energy scale is far above the EW scale, *i.e.*, $Q^2\gg\mu_{\rm EW}^2$.

The initial conditions of the EW PDFs at $\mu_{\rm EW}$ is determined by a matching condition. Due to the unpolarized feature of the low energy QED⊗QCD running, the left- and right-handed components are equal at the matching scale $\mu_{\rm EW}$:

$$f_{f_L} = f_{f_R} = \frac{1}{2} f_f,\ \ f_{\bar{f}_L} = f_{\bar{f}_R} = \frac{1}{2} f_{\bar{f}}, \tag{153}$$

where $f = e, u, d$ for all the light generations. The neutrino and top quark PDFs are zeros at $\mu_{\rm EW}$:

$$f_\nu = f_t = 0. \tag{154}$$

Following the decomposition in Ref. [13, 43], we work in the isospin (T) and charge-parity (CP) basis. The PDFs for the leptonic doublets can be written as in the (T,CP) basis as

$$f_\ell^{0\pm} = \tfrac{1}{4}\left[(f_{\nu_L} + f_{\ell_L}) \pm (f_{\bar{\nu}_L} + f_{\bar{e}_L})\right], \quad f_\ell^{1\pm} = \frac{1}{4}\left[(f_{\nu_L} - f_{\ell_L}) \pm (f_{\bar{\nu}_L} - f_{\bar{e}_L})\right]. \tag{155}$$

Similarly, we have the quark doublet PDFs as

$$f_q^{0\pm} = \tfrac{1}{4}\left[(f_{u_L} + f_{d_L}) \pm (f_{\bar{u}_L} + f_{\bar{d}_L})\right], \quad f_q^{1\pm} = \frac{1}{4}\left[(f_{u_L} - f_{d_L}) \pm (f_{\bar{u}_L} - f_{\bar{d}_L})\right]. \tag{156}$$

The right-handed fermion PDFs are given by

$$f_e^{0\pm} = \frac{1}{2}[f_{e_R} \pm f_{\bar{e}_R}],\ f_u^{0\pm} = \frac{1}{2}[f_{u_R} \pm f_{\bar{u}_R}],\ f_d^{0\pm} = \frac{1}{2}[f_{d_R} \pm f_{\bar{d}_R}]. \tag{157}$$

Keep in mind that each fermion carries a generation index, which is implicitly left out for simplicity. We can combine them into singlet PDFs

$$f_L^{0,1\pm} = \textstyle\sum_i^{N_g} f_\ell^{0,1\pm}, \qquad f_Q^{0,1\pm} = \displaystyle\sum_i^{N_g} f_q^{0,1\pm}, \tag{158}$$

$$f_E^{0\pm} = \textstyle\sum_i^{N_g} f_e^{0\pm}, \qquad f_U^{0\pm} = \displaystyle\sum_i^{N_g} f_u^{0\pm}, \quad f_D^{0\pm} = \sum_i^{N_g} f_d^{0\pm}. \tag{159}$$

At $\mu_{\rm EW}$, the massive gauge boson PDFs (including the mixing) are also zeros:

$$f_{Z_\pm} = f_{\gamma Z_\pm} = f_{W_\pm^\pm} = 0. \tag{160}$$

In our notation, the upper sign on the gauge boson indicates the charge, while the lower sign specifies the polarization. The non-zero polarized PDFs for the massless gauge bosons are

$$f_{\gamma_+} = f_{\gamma_-} = \frac{1}{2} f_\gamma, \;\; f_{g_+} = f_{g_-} = \frac{1}{2} f_g, \tag{161}$$

due to the unpolarized QED⊗QCD evolution below $\mu_{\rm EW}$. We can rotate the neutral bosonic PDFs into the gauge basis as

$$\begin{pmatrix} f_{B_\pm} \\ f_{W^3_\pm} \\ f_{BW^3_\pm} \end{pmatrix} = \begin{pmatrix} c_W^2 & s_W^2 & -c_W s_W \\ s_W^2 & c_W^2 & c_W s_W \\ 2c_W s_W & -2c_W s_W & c_W^2 - s_W^2 \end{pmatrix} \begin{pmatrix} f_{\gamma_\pm} \\ f_{Z_\pm} \\ f_{\gamma Z_\pm} \end{pmatrix}, \tag{162}$$

where $s_W = \sin\theta_W$ and $c_W = \cos\theta_W$, and θ_W is the Weinberg mixing angle.

We also need to decompose the bosonic PDFs into the (T,CP) basis:

$$\begin{aligned}
f_W^{0\pm} &= \frac{1}{3}\left[\left(f_{W^+_+} + f_{W^-_+} + f_{W^3_+}\right) \pm \left(f_{W^+_-} + f_{W^-_-} + f_{W^3_-}\right)\right], && (163)\\
f_W^{1\pm} &= \frac{1}{2}\left[\left(f_{W^+_+} - f_{W^-_+}\right) \mp \left(f_{W^+_-} - f_{W^-_-}\right)\right], && (164)\\
f_W^{2\pm} &= \frac{1}{6}\left[\left(f_{W^+_+} + f_{W^-_+} - 2f_{W^3_+}\right) \pm \left(f_{W^+_-} + f_{W^-_-} - 2f_{W^3_-}\right)\right]. && (165)
\end{aligned}$$

The PDFs involving the hyper-charge gauge boson and gluon are given as

$$f_B^{0\pm} = f_{B_+} \pm f_{B_-}, \;\; f_{BW}^{1\pm} = f_{BW_+} \pm f_{BW_-}, \;\; f_g^{0\pm} = f_{g_+} \pm f_{g_-}. \tag{166}$$

Up to now, we can construct the DGLAP equations in the (T,CP) basis. For DGLAP evolution for the singlet 0± PDFs is

$$\frac{\mathrm{d}}{\mathrm{d}L} \begin{pmatrix} f_L^{0\pm} \\ f_Q^{0\pm} \\ f_E^{0\pm} \\ f_U^{0\pm} \\ f_D^{0\pm} \\ f_B^{0\pm} \\ f_W^{0\pm} \\ f_g^{0\pm} \end{pmatrix} = \begin{pmatrix} P_{LL}^{0\pm} & 0 & 0 & 0 & 0 & P_{LB}^{0\pm} & P_{LW}^{0\pm} & 0 \\ 0 & P_{QQ}^{0\pm} & 0 & 0 & 0 & P_{QB}^{0\pm} & P_{QW}^{0\pm} & P_{Qg}^{0\pm} \\ 0 & 0 & P_{EE}^{0\pm} & 0 & 0 & P_{EB}^{0\pm} & 0 & 0 \\ 0 & 0 & 0 & P_{UU}^{0\pm} & 0 & P_{UB}^{0\pm} & 0 & P_{Ug}^{0\pm} \\ 0 & 0 & 0 & 0 & P_{DD}^{0\pm} & P_{DB}^{0\pm} & 0 & P_{Dg}^{0\pm} \\ P_{BL}^{0\pm} & P_{BQ}^{0\pm} & P_{BE}^{0\pm} & P_{BU}^{0\pm} & P_{BD}^{0\pm} & P_{BB}^{0\pm} & 0 & 0 \\ P_{WL}^{0\pm} & P_{WQ}^{0\pm} & 0 & 0 & 0 & 0 & P_{WW}^{0\pm} & 0 \\ 0 & P_{gQ}^{0\pm} & 0 & P_{gU}^{0\pm} & P_{gD}^{0\pm} & 0 & 0 & P_{gg}^{0\pm} \end{pmatrix} \otimes \begin{pmatrix} f_L^{0\pm} \\ f_Q^{0\pm} \\ f_E^{0\pm} \\ f_U^{0\pm} \\ f_D^{0\pm} \\ f_B^{0\pm} \\ f_W^{0\pm} \\ f_g^{0\pm} \end{pmatrix} \tag{167}$$

The specific expressions for the splitting functions can be found in App. B. Similarly, we have the singlet 1± PDF evolution as

$$\frac{\mathrm{d}}{\mathrm{d}L}\begin{pmatrix} f_L^{1\pm} \\ f_Q^{1\pm} \\ f_W^{1\pm} \\ f_{BW}^{1\pm} \end{pmatrix} = \begin{pmatrix} P_{LL}^{1\pm} & 0 & P_{LW}^{1\pm} & P_{LM}^{1\pm} \\ 0 & P_{QQ}^{1\pm} & P_{QW}^{1\pm} & P_{QM}^{1\pm} \\ P_{WL}^{1\pm} & P_{WQ}^{1\pm} & P_{WW}^{1\pm} & 0 \\ P_{ML}^{1\pm} & P_{MQ}^{1\pm} & 0 & P_{MM}^{1\pm} \end{pmatrix} \otimes \begin{pmatrix} f_L^{1\pm} \\ f_Q^{1\pm} \\ f_W^{1\pm} \\ f_{BW}^{1\pm} \end{pmatrix} \tag{168}$$

where the symbol M indicates the mixing state BW. The 2± PDF evolution is simple as

$$\frac{\mathrm{d}}{\mathrm{d}L} f_W^{2\pm} = P_{WW}^{2\pm} \otimes f_{WW}^{2\pm}. \tag{169}$$

The non-singlet PDFs evolve independently,

$$\tfrac{\mathrm{d}}{\mathrm{d}L} f_{L,NS}^{0,1\pm} = P_{LL}^{0,1\pm} \otimes f_{L,NS}^{0,1\pm}, \quad \frac{\mathrm{d}}{\mathrm{d}L} f_{Q,NS}^{0,1\pm} = P_{QQ}^{0,1\pm} \otimes f_{Q,NS}^{0,1\pm}, \tag{170}$$

$$\tfrac{\mathrm{d}}{\mathrm{d}L} f_{E,NS}^{0\pm} = P_{EE}^{0\pm} \otimes f_{E,NS}^{0\pm}, \quad \frac{\mathrm{d}}{\mathrm{d}L} f_{U,NS}^{0\pm} = P_{UU}^{0\pm} \otimes f_{U,NS}^{0\pm}, \tag{171}$$

$$\tfrac{\mathrm{d}}{\mathrm{d}L} f_{D,NS}^{0\pm} = P_{DD}^{0\pm} \otimes f_{D,NS}^{0\pm}. \tag{172}$$

$$\tag{173}$$

The non-trivial non-singlet PDFs are defined as

$$f_{L,NS}^{0,1\pm} = f_{\ell_1}^{0,1\pm} - f_{\ell_2}^{0,1\pm}, \quad f_{Q,NS}^{0,1\pm} = f_{q_2}^{0,1\pm} - f_{q_3}^{0,1\pm}, \tag{174}$$

$$f_{E,NS}^{0\pm} = f_{e_1}^{0\pm} - f_{e_2}^{0\pm}, \quad f_{U,NS}^{0\pm} = f_{u_2}^{0\pm} - f_{u_3}^{0\pm},\ f_{D,NS}^{0\pm} = f_{d_2}^{0\pm} - f_{d_3}^{0\pm}. \tag{175}$$

The following non-singlet PDFs are trivially zero due to the zero initial conditions at μ_{EW},

$$f_{L,23}^{0,1\pm} = f_{E,23}^{0\pm} = 0, f_{Q,12}^{0,1,\pm} = f_{U,12}^{0\pm} = f_{D,12}^{0\pm} = 0, \tag{176}$$

where the index $12, 23$ specify the difference of the generations.

The PDFs in the (T,CP) basis for each generation can be reconstructed with singlet and non-singlet PDFs as:

$$f_{\ell_1}^{0,1\pm} = \tfrac{f_L^{0,1\pm} + (N_g - 1) f_{L,NS}^{0,1\pm}}{N_g}, \quad f_{\ell_2}^{0,1\pm} = f_{\ell_3}^{0,1\pm} = \frac{f_L^{0,1\pm} - f_{L,NS}^{0,1\pm}}{N_g}, \tag{177}$$

$$f_{q_1}^{0,1\pm} = f_{q_2}^{0,1\pm} = \tfrac{f_Q^{0,1\pm} + f_{L,NS}^{0,1\pm}}{N_g}, \quad f_{q_3}^{0,1\pm} = \frac{f_Q^{0,1\pm} - (N_g - 1) f_{Q,NS}^{0,1\pm}}{N_g} \tag{178}$$

Similarly for the right-handed components

$$f_{e_1}^{0\pm} = \tfrac{f_E^{0\pm}+(N_g-1)f_{E,NS}^{0\pm}}{N_g}, \qquad f_{e_2}^{0\pm} = f_{e_3}^{0\pm} = \frac{f_E^{0\pm} - f_{E,NS}^{0\pm}}{N_g}, \tag{179}$$

$$f_{u_1}^{0\pm} = f_{u_2}^{0\pm} = \tfrac{f_U^{0\pm}+f_{U,NS}^{0\pm}}{N_g}, \qquad f_{u_3}^{0\pm} = \frac{f_U^{0\pm} - (N_g-1)f_{U,NS}^{0\pm}}{N_g}, \tag{180}$$

$$f_{d_1}^{0\pm} = f_{d_2}^{0\pm} = \tfrac{f_D^{0\pm}+f_{D,NS}^{0\pm}}{N_g}, \qquad f_{d_3}^{0\pm} = \frac{f_D^{0\pm} - (N_g-1)f_{D,NS}^{0\pm}}{N_g}. \tag{181}$$

$$\tag{182}$$

Finally, all the chiral states for each generation can be determined in terms of PDFs in the (T,CP) basis, through the inversion of the Eqs. (155-157,162-166).

3.0 Standard Model physics at a high-energy muon collider

For future ultra-high-energy lepton colliders, such as a multi-TeV level muon collider, the collision energy is far above the electroweak scale thus the collinear splitting mechanism of the electroweak gauge bosons becomes the dominant phenomena via the initial state radiation and the final state showering. In this chapter, we will present the partonic picture at a possible multi-TeV level muon collider, where the electroweak PDFs formalism is employed as the proper description for partonic collisions of the initial states. The results in this chapter are reported in Ref. [6, 7, 45].

3.1 The physics picture of a high-energy muon collider

3.1.1 Introduction

With the discovery of the Higgs boson at the CERN Large Hadron Collider (LHC), the particle spectrum of the Standard Model (SM) is complete. The next target at the energy frontier will be to study the Higgs properties and to search for the next scale beyond the SM [46]. The physics potential for TeV-scale e^+e^- linear colliders, such as the International Linear Collider [47] and the CERN Compact Linear Collider (CLIC) [48], has been studied to great details. More recently, due to the breakthrough in the cooling technology for a muon beam [49], there has been renewed interest in constructing a $\mu^+\mu^-$ collider reaching a center-of-momentum energy (c.m. energy) $\sqrt{s} \sim \mathcal{O}(10\text{ TeV})$. Advancement of the wakefield electron acceleration technology [50] has also been encouraging to have stimulated our ambition for reaching multi-TeV threshold in leptonic collisions.

Lepton colliders provide a clean experimental environment for precision measurements of physical observables and for discovery of new particles. Near a mass threshold, the e^+e^- annihilation may produce a new particle singly in the s-channel, or a particle/anti-particle in pair. As the beam energy increases, the initial state radiation (ISR) becomes substantial.

It not only degrades the colliding energies of the leptons, but also generates new reactions of the radiation fields. The most familiar phenomenon is the collinear photon radiation off the high energy charged particles given by the Weizsäicker-Williams spectrum [8, 9],

$$\mathcal{P}_{\gamma,\ell}(x) \approx \frac{\alpha}{2\pi} P_{\gamma,\ell}(x) \ln \frac{E^2}{m_\ell^2}, \tag{183}$$

where the splitting functions are $P_{\gamma/\ell}(x) = (1+(1-x)^2)/x$ for $\ell \to \gamma$ and $P_{\ell/\ell}(x) = (1+x^2)/(1-x)$ for $\ell \to \ell$, with an energy xE off the charged lepton beam of energy E. This is the leading order effective photon approximation (EPA), which allows us to write the cross sections for photon initiated processes as

$$\begin{aligned} \sigma(e^-(p)a \to e^-(p')X) &= \frac{1}{2S}\overline{\Sigma}|\mathcal{M}|^2 \frac{d\vec{p}'}{(2\pi)^3 2E'}\, dPS_X \equiv \int dx\ P_{\gamma/e}(x)\ \sigma(\gamma a), & (184)\\ \sigma_{EPA}(e^- A \to e^- X) &= \int dx\ \mathcal{P}_{\gamma/e}(x)\ \hat{\sigma}(\gamma A). & (185)\end{aligned}$$

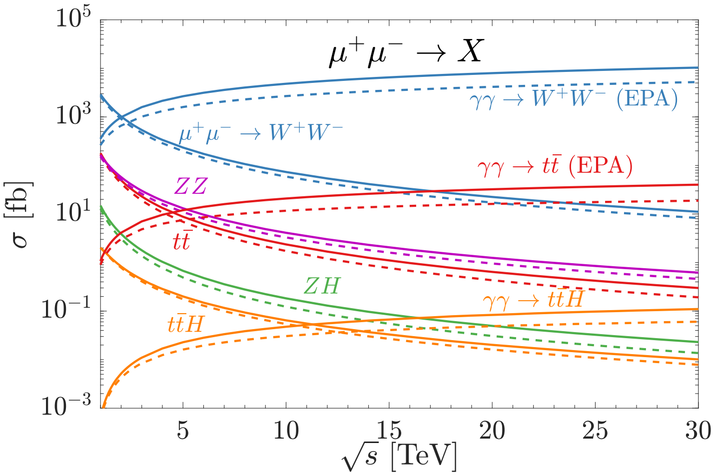

Figure 4: Production cross sections in $\mu^+\mu^-$ collisions versus the c.m. energy. The dashed falling curves are for the direct $\mu^+\mu^-$ annihilation, and the solid falling curves (slightly above the dashed) include the ISR effects. The solid rising curves are for $\gamma\gamma$-EPA by Eq. (190) and the dashed rising curves are from the leading-order γ-PDF at $Q = \sqrt{\hat{s}}/2$.

In Fig. 4, we show some representative production cross sections versus the $\mu^+\mu^-$ c.m. energy $\sqrt{s}$ for

$$\mu^+\mu^- \to W^+W^-,\ ZZ,\ t\bar{t},\ ZH \text{ and } t\bar{t}H. \tag{186}$$

The dashed (falling) curves are for the direct $\mu^+\mu^-$ annihilation, and the solid curves (slightly above the dashed) include the ISR effects [51]. We see the typical fall of the annihilation cross sections as $1/s$. The ISR reduces the c.m. energy at the collision and thus increases the cross section. At $\sqrt{s} = 10$ TeV (30 TeV), the cross section for $\mu^+\mu^- \to t\bar{t}$ production can be enhanced by 40% (60%) due to the ISR effects. Owing to the collinear enhancement, the two-photon ($\gamma\gamma$) fusion processes grow double-logarithmically. We calculate the total cross sections with the EPA spectrum in Eq. (190) for

$$\gamma\gamma \to W^+W^-,\ \ t\bar{t} \text{ and } t\bar{t}H. \tag{187}$$

Those processes take over the annihilation channels at higher energies $\sqrt{s} \approx 2.5, 4.5, 11$ TeV for W^+W^-, $t\bar{t}$ and $t\bar{t}H$ production, respectively, as shown in Fig. 4 by the rising solid curves labeled by EPA. At $\sqrt{s} \approx 30$ TeV, the production rate for $\gamma\gamma \to t\bar{t}$ is higher by two orders of magnitude than that for $\mu^+\mu^- \to t\bar{t}$ annihilation.

However, this description becomes inadequate at some high scales. First, at high energies $E \gg m_\ell$, the collinear logarithm $(\alpha/2\pi)\ln(E^2/m_\ell^2)$ may be sizeable and needs to be resummed for reliable predictions. This leads to the QED analogue of the Dokshitzer-Gribov-Lipatov-Altarelli-Parisi (DGLAP) equations [22, 20, 19], the concept of QED parton distribution functions (PDFs) for the photon and charged fermions [52, 53, 54]. To estimate the resummation effects, we plot the cross sections with the leading-order γ-PDF with a scale $Q = \sqrt{\hat{s}}/2$, where $\sqrt{\hat{s}}$ is the $\gamma\gamma$ c.m. energy. As shown in Fig. 4 by the dashed rising curves below those of EPA, we see that the rates are lowered as expected, and could be smaller by about a factor of two at 30 TeV.

More importantly, as pointed out in Refs. [15, 13, 43] and explored in details [6], at scales $Q^2 \gg M_Z^2$, the SM gauge symmetry $\mathrm{SU}(2)_L \otimes \mathrm{U}(1)_Y$ is effectively restored. Consequently, the four EW gauge bosons $(W^{\pm,3}, B)$ in the SM must be taken into account all together coherently with B-W^3 mixing and interference. The fermion interactions are chiral and the couplings and states evolve according to the SM unbroken gauge symmetry. One needs to invoke the picture of electroweak parton distribution functions (EW PDFs) [16, 14, 55] dynamically generated by the electroweak and Yukawa interactions. The longitudinally polarized gauge bosons capture the remnants of the EW symmetry breaking. The effects are governed by power corrections of the order M_Z^2/Q^2 [10, 11], a measure of the Goldstone-Boson Equivalence violation [15, 56], analogous to higher-twist effects in QCD.

3.1.2 The partonic picture of a high-energy muon collider

While a lepton collider has the great merit for a monochromatic energy spectrum at the designed center-of-momentum (c.m.) energy $\sqrt{s}$, it simultaneously offers a broad energy spectrum due to the enhanced collinear radiation of the electroweak (EW) gauge bosons. This leads to the familiar phenomena of the photon-photon collisions [57, 58]. In fact, the vector-boson fusion (VBF) mechanism dominates the physical processes in high-energy leptonic collisions [59, 60, 6]. To properly describe those reactions, it was emphasized recently [6] that it is appropriate to adopt the partonic picture by introducing the electroweak parton distribution functions (EW PDFs) [12, 15, 55, 61], which run according to the evolution equations of the unbroken gauge theory of $\mathrm{SU(2)_L \otimes U(1)_Y}$ at high energies above the EW scale. It is important to formulate the EW PDFs to predict the SM expectations at the ultra-high energies, before estimating the sensitivity for new physics searches.

We write the production cross section of an exclusive final state F and the unspecified remnants X in terms of the parton luminosity $\mathrm{d}\mathcal{L}_{ij}/\mathrm{d}\tau$ and the corresponding partonic sub-process cross section $\hat{\sigma}$

$$\begin{aligned} \sigma(\ell^+\ell^- \to F + X) &= \textstyle\int_{\tau_0}^1 \mathrm{d}\tau \sum_{ij} \frac{\mathrm{d}\mathcal{L}_{ij}}{\mathrm{d}\tau}\ \hat{\sigma}(ij \to F), \\ \frac{\mathrm{d}\mathcal{L}_{ij}}{\mathrm{d}\tau} &= \frac{1}{1+\delta_{ij}} \textstyle\int_\tau^1 \frac{\mathrm{d}\xi}{\xi} \left[f_i(\xi, Q^2) f_j\left(\frac{\tau}{\xi}, Q^2\right) + (i \leftrightarrow j)\right], \end{aligned} \tag{188}$$

where $\tau = \hat{s}/s$ with $\sqrt{s}$ ($\sqrt{\hat{s}}$) the collider (parton) c.m. energy. The production threshold is $\tau_0 = m_F^2/s$.

In presenting our results for production of SM particles at a high-energy lepton collider, for definitiveness, we consider a future $\mu^+\mu^-$ collider with multi-TeV energies. It is informative to first examine the parton luminosities as shown in Fig. 5(b) for $\sqrt{s} = 30$ TeV versus

$\sqrt{\tau}$, with a variety of partonic initial states. The upper horizontal axis labels the accessible $\sqrt{\hat{s}}$. Although we properly evolve the EW PDFs according to the unbroken SM gauge groups, we convert the states back for the sake of common intuition, shown in the figure for $\mu^+\mu^-$, $\nu_\mu\bar{\nu}_\mu$, $\gamma\gamma/ZZ/\gamma Z$, W_TW_T and W_LW_L. We see that the fermionic luminosities peak near the machine c.m. energy $\tau \approx 1$, while the gauge boson luminosities, generically called vector boson fusion (VBF) dominate at lower partonic energy $\sqrt{\hat{s}}$. As noted earlier, the neutral gauge boson luminosities are the largest, followed by W_T and W_L.

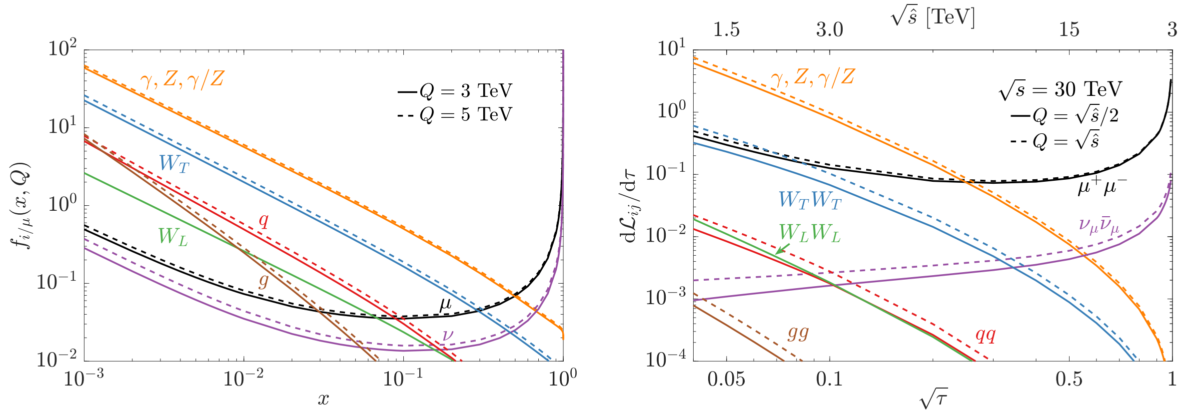

Figure 5: Distributions for (a) EW PDFs $f_i(x)$ and, (b) parton luminosities $\mathrm{d}\mathcal{L}_{ij}/\mathrm{d}\tau$ versus $\sqrt{\tau}$ for $\sqrt{s} = 30$ TeV with a factorization scale $Q = \sqrt{\hat{s}}/2$ (solid) and $\sqrt{\hat{s}}$ (dashed).

We emphasize the "inclusiveness" of the production processes. For example, for an exclusive final state of $t\bar{t}$ production, one needs to sum over all the observationally indistinguishable partonic contributions in the initial state $\mu^+\mu^-, \gamma\gamma, \gamma Z, ZZ, W^+W^- \to t\bar{t}$. Contributions from the quark and gluon initial states are sub-leading as seen in the parton luminosities in Fig. 5(b), and we do not include them in the cross section calculations throughout this letter. Since the collinear remnants are not observationally resolved, one cannot separate the $\mu^+\mu^-/\nu_\mu\bar{\nu}_\mu$ annihilations from the VBF. For this reason, we call such processes, *i.e.*, $\mu^+\mu^- \to t\bar{t}$ "semi-inclusive". This is analogous to the $t\bar{t}$ production at hadron colliders from the partonic sub-processes $q\bar{q}, gg \to t\bar{t}$.

In Fig. 6(a), we show the semi-inclusive production cross sections at a $\mu^+\mu^-$ collider versus the collider c.m. energy $\sqrt{s}$ from 1 TeV to 30 TeV. We choose the factorization scale

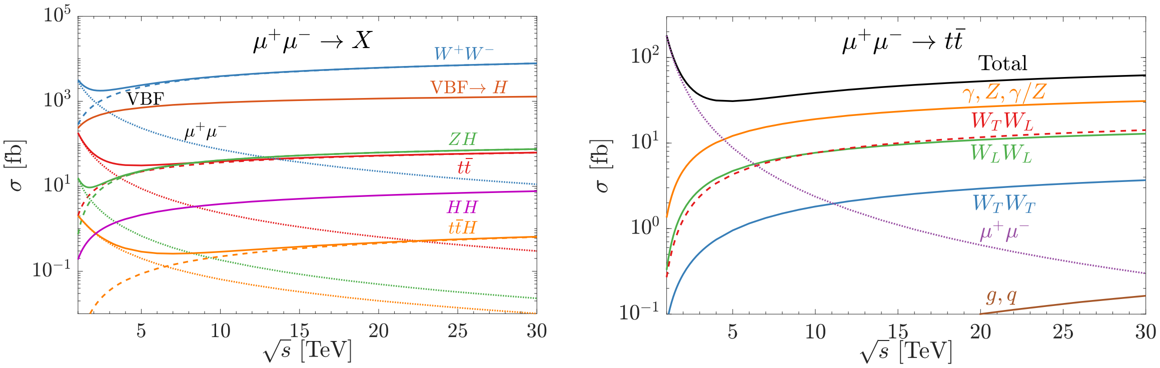

Figure 6: Production cross section for semi-inclusive processes at a $\mu^+\mu^-$ collider versus the c.m. energy. The solid curves are for (a) the total cross sections and the dashed (dotted) curves from VBF ($\mu^+\mu^-$ annihilation) with EW PDF, and (b) for $t\bar{t}$ production decomposed to the underlying contributions from $\mu^+\mu^-, \gamma/Z/\gamma Z, W_TW_L$, W_LW_L and W_TW_T.

$Q = \sqrt{\hat{s}}/2$ in calculating the EW PDFs.[1] The solid curves are the total cross sections for the semi-inclusive processes for

$$\mu^+\mu^- \to W^+W^-,\ H,\ ZH,\ t\bar{t},\ HH\ \text{ and }\ t\bar{t}H, \tag{189}$$

combining the contributions from both fermionic initial states and the VBF. We indicate the VBF contributions by the dashed curves,[2] and the fermionic contributions by the dotted curves, respectively, below the solid curves. It is important to note that, although there is no logarithmic evolution for the W_L PDF, the partonic sub-process cross sections are much enhanced for $W_LW_L, Z_LZ_L \to t\bar{t}, t\bar{t}H$ and H, ZH, HH, due to the Goldstone-boson interactions. The VBF processes take over the annihilation channels at higher energies $\sqrt{s} \approx 2.3, 3.5, 6.5$ TeV for W^+W^-, $t\bar{t}$ and $t\bar{t}H$, respectively. To appreciate the individual contributions from the underlying partonic subprocesses, we decompose them for the

---

[1] To validate the EW PDF approximation, we have imposed an angular cutoff for the W/Z initiated processes in the c.m. frame $\cos\theta < 1 - m^2/\hat{s}$, where m is the relevant particle mass involved in the process. We have included a tighter cut $\cos\theta < 0.99$ and $\sqrt{\hat{s}} > 500$ GeV for the W^+W^-, ZH final states.

[2] Many of the VBF processes have been calculated recently in Ref. [62] at the tree-level. We have good agreements with theirs where ever they overlap.

process $\mu^+\mu^- \to t\bar{t}$ versus the c.m. energy, as shown in Fig. 6(b) for $\mu^+\mu^-$, $\gamma\gamma/\gamma Z/ZZ$, W_TW_L, W_LW_L as well as W_TW_T. As expected, the QED contribution remains to be the leading channel. Not well appreciated, the W_TW_L/W_LW_L contributions become as significant.

We now examine the kinematic distributions for the final state $t\bar{t}$ system, for the individual contributions $\mu^+\mu^-, \gamma/Z, W_TW_L, W_LW_L$ and W_TW_T. Shown in Fig. 7(a) are the normalized invariant mass distributions $m_{t\bar{t}}$. We see that, for the $\mu^+\mu^-$ annihilation, the distribution is sharply peaked at the collider c.m. energy, with a tail due to the radiative return. For the VBF, they are peaked after the $2m_t$ threshold. We show in Fig. 7(b) the normalized rapidity distributions of the system $y_{t\bar{t}}$. Again, events from the $\mu^+\mu^-$ annihilation are sharply central, while those from VBF are spread out, reflecting the boost due to the momentum imbalance between the two incoming partons.

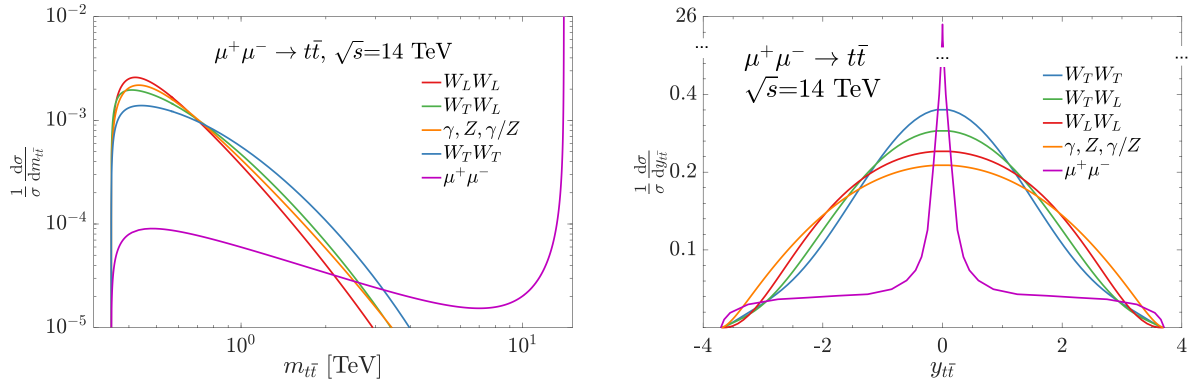

Figure 7: Normalized differential distributions for the final state $t\bar{t}$ system (a) the invariant mass $m_{t\bar{t}}$ and (b) the rapidity $y_{t\bar{t}}$.

We summarize our results utilizing the EW PDFs in Table 4 for a few characteristic processes for a muon collider with a few representative energies 3, 6, 10, 14 and 30 TeV. For the sake of illustration, we once again separate the partonic sub-processes by the fermionic annihilation and by VBF.

$\sqrt{s}$ (TeV)	3		6		10		14		30	
σ (fb)	VBF	$\mu\mu$	VBF	$\mu\mu$	VBF	$\mu\mu$	VBF	$\mu\mu$	VBF	$\mu\mu$
W^+W^-	1300	540	2500	170	3800	73	4900	41	7800	11
$t\bar{t}$	13	23	25	6.2	36	2.4	43	1.3	61	0.30
ZH	12	1.8	26	0.48	41	0.18	51	0.097	75	0.023
HH	1.2	–	2.5	–	3.8	–	4.8	–	7.6	–
$t\bar{t}H$	0.036	0.45	0.12	0.15	0.22	0.065	0.32	0.037	0.64	0.010

Table 4: Production cross sections at a muon collider in units of fb by VBF utilizing the EW PDF and by direct $\mu^+\mu^-$ annihilation with ISR effects.

3.1.3 Discussions and conclusions

Some comments are in order:

- The naive EPA is inadequate at high scales. The QED evolution of $\ln(Q^2/m_\ell^2)$ in the γ-PDF should capture the dominant effect at an appropriate physical scale Q^2. Although the Z contribution is typically small until reaching a very high scale, the mixed state $\gamma Z(BW^3)$ needs to be taken into account that often interferes destructively.
- The EW PDF approach allows for calculating individual contributions from the polarized initial state partons, with correlations to the corresponding sub-process matrix elements. This is an important feature when polarization is needed for exploring a certain type of underlying dynamics. This option would be unavailable with the fixed order (FO) diagrammatic calculations [63, 64, 62]. In addition, the FO calculations may face a tremendous challenge for numerical stability dealing with the large collinear logs $\ln(Q^2/m_\ell^2)$.
- Although no logarithmic growth for the longitudinally polarized gauge boson PDFs, the large Yukawa coupling to the top quark and the scalar self-interaction of the Goldstone bosons make the sub-processes substantially enhanced, as seen for the VBF production of $t\bar{t}, t\bar{t}H, ZH$ and HH.

- For the PDFs of fermions with a bare SU(2) charge, due to the incomplete cancellation of the infrared divergence, they are not exactly factorizable. This is known as the violation of the Bloch-Nordsieck theorem [14, 15]. This does not pose a problem to the beam (valence) lepton because it is a numerically small higher-order correction. This could lead to an unphysical solution to the dynamically generated neutrinos. We impose an infrared cutoff as a regulator $\tau^{\max} = 1 - M_Z/Q$, which assures the resummation to a double-log accuracy [13].
- We have not taken into account the effects of the final-state radiations (FSR). This could become one of the dominant features at very high energies, properly described by the "fragmentation functions" [15, 65]. We leave this topic for future explorations.
- We did not quantify the potentially large corrections near the threshold $Q^2 \geq 4m^2$. On the one hand, our formalism aims to address the physics far above the threshold $Q^2 \gg M_Z^2$. On the other hand, the infrared behavior of the gauge boson radiation tends to populate the events in the low-Q^2 region. We leave this topic for future investigations.
- Although we focused on a $\mu^+\mu^-$ collider in our presentation, the EW PDF formalism is equally applicable for e^+e^- colliders. The only difference is the QED radiation effects, further enhanced by a factor $\ln\left(m_\mu^2/m_e^2\right)$. It is also straightforward to apply our formalism to the high energy hadron colliders, although the photon PDF of the proton at a low scale is more subtle [38, 61].

In summary, we advocated that all particles accessible under the SM interactions should be viewed as EW partons in high energy leptonic collisions well above the EW scale. We presented a systematic approach to define the EW PDFs for leptons and gauge bosons accurate to the order of LL under the unbroken gauge symmetry. We calculated the production cross sections for some characteristic SM processes at a high-energy muon collider in the EW PDF formalism. Polarized partonic cross sections can be evaluated individually that are desirable for exploring new physics beyond the Standard Model at future high energy colliders.

3.2 Colored partons of high-energy leptons

In the subsequent splitting of the EW gauge bosons, quarks enter the picture of the EW partons from $\gamma/Z, W^\pm \to q\bar{q}'$. The strong QCD interactions of quarks and gluons take over and the coupled DGLAP equations of the full Standard Model must be invoked [13, 43]. This would yield QCD contributions in leptonic collisions and thus lead to new mechanisms for the production of colored states [66]. In fact, quark contributions to QCD jet production in e^+e^- collisions were considered in the literature [18]. They are the dominant phenomena in the kinematical region with forward-backward scattering and lower energy transfer. It is thus important to have a clear understanding of the events and the characteristics taking into account the EW and QCD interactions of the partons in high-energy lepton collisions. Motivated by the recent discussions on the future high-energy e^+e^- or $\mu^+\mu^-$ colliders, we consider a collider with the c.m. energies

$$\sqrt{s} = 3 \text{ TeV} - 15 \text{ TeV},$$

with a few benchmark points as 3 TeV, 6 TeV, 10 TeV, and 14 TeV. The 3-TeV c.m. energy is the benchmark for the Compact Linear Collider [67] and the higher energies are those under discussion for future muon colliders [68]. The total integrated luminosity is assumed to be in the range of $(1-10)$ ab^{-1}.

3.2.1 PDFs and partonic luminosities at a lepton collider

With the formalism in Chapter 2, we can compute the parton distribution functions of quarks and the gluon in a high-energy lepton, along with leptons and the photon. At the low energy below $\mu_{\rm EW}$, the massive gauge bosons, neutrinos, and the top quark are inactive. We only have the PDFs for the flavors specified in Eq. (142) plus the photon and gluon. We show the PDFs for an electron beam ($e^\pm$) in Fig. 8(a) and a muon beam ($\mu^\pm$) in Fig. 8(b) for the factorization scales $Q = 30$ (50) GeV.

The initial condition for a valence lepton PDF is set as in Eq. (143). Including the leading soft radiation near $x \to 1$, it behaves as $1/(1-x)$. In the low-x limit ($x \to 0$),

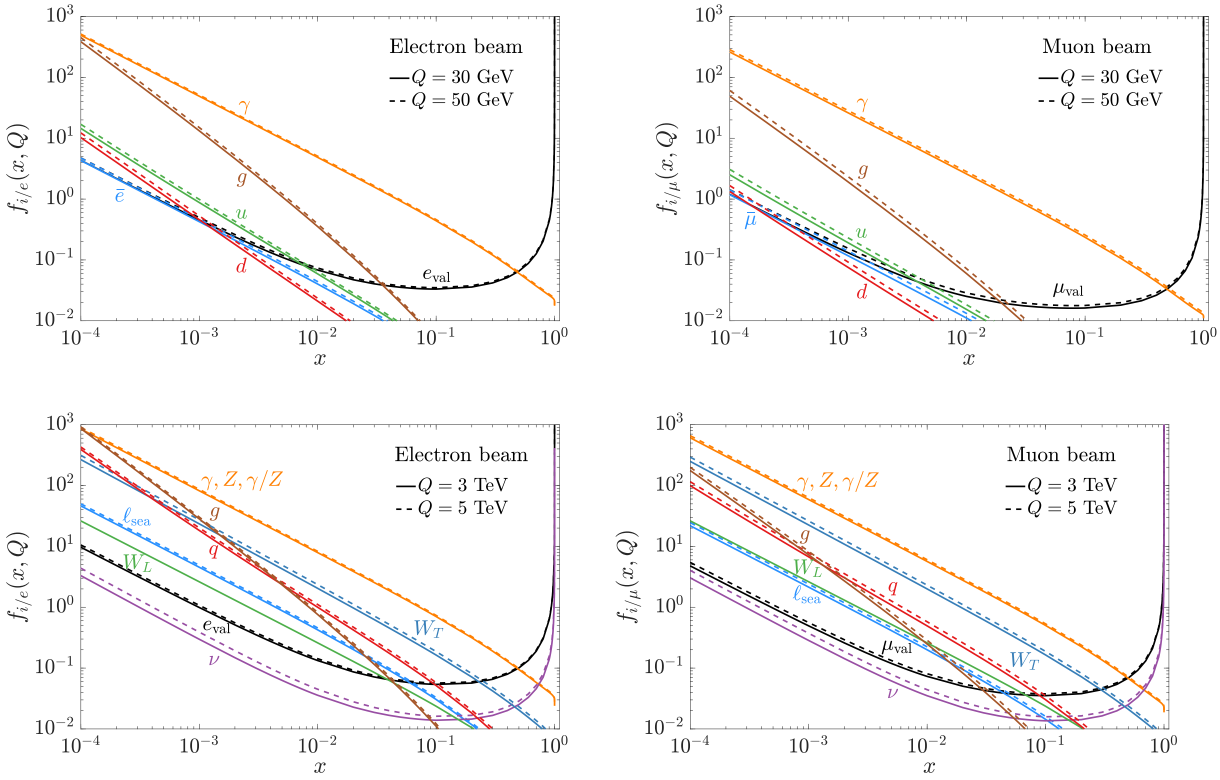

Figure 8: PDFs in a high-energy lepton for (a) an electron and (b) a muon below the EW scale at $Q = 30$ (50) GeV; and for (c) an electron and (d) an muon above the EW scale at $Q = 3$ (5) TeV.

the valence PDF deviates from the leading $1/(1-x)$ behavior, and receives $1/x$ (and $\log x$) enhancement from higher order splitting $\gamma \to \ell^+\ell^-$. It coincides with sea flavor $f_{\ell_{\text{val}}} \sim f_{\bar{\ell}_{\text{val}}}$ shown explicitly in Fig. 8, because $\gamma \to \ell^+\ell^-$ splitting gives the same amount of ℓ^+ and ℓ^-.

The photon is generated dynamically through the splitting of charged particles, $\ell(q) \to \ell(q)\gamma$. The leading order splitting gives the traditional Equivalent Photon Approximation (EPA) [8, 9]

$$f_{\gamma/\ell,\text{EPA}}(x_\gamma, Q^2) = \frac{\alpha}{2\pi}\frac{1+(1-x_\gamma)^2}{x_\gamma}\log\frac{Q^2}{m_\ell^2}, \tag{190}$$

with a suitably chosen scale Q associated with the physical process.[3] All the sea fermions, including leptons and quarks, are generated through $\gamma \to \ell^+\ell^-, q\bar{q}$, while gluon comes from $q \to qg$ splitting. In the low-x limit, the generated PDFs behave as $1/x$ plus $\log^p x$ corrections.

Including higher orders, the valence PDF receives threshold corrections of the form $1/(1-x)$ and $\log^p(1-x)$. The precise determination of the PDFs in the $x \to 1$ limit requires all orders of resummation. It can be only achieved for the valence non-singlet PDF under the fixed coupling assumption when x asymptotically approaches 1. A smooth transition to the $x \to 1$ asymptotic form requires a consistent matching [70]. In our practical treatment, we take the valence lepton PDF as a functional form as

$$f_{\ell/\ell}(x, Q^2) = \begin{cases} f_{\text{resum}}(x, Q^2), & x < 1-\epsilon, \\ L(Q^2)\delta(1-x), & x \geq 1-\epsilon, \end{cases} \tag{191}$$

where ϵ serves as a regulator.[4] Within $x < 1-\epsilon$, the $f_{\text{resum}}(x, Q^2)$ is obtained through the DGLAP resummation, which will converge to the all-order resummation form with a sufficient higher order of iterations. Beyond the cutoff, the dynamically generated PDFs are negligible, while the valence PDF is taken as the form of a local form, $L(Q^2)\delta(1-x)$. The coefficient $L(Q^2)$ is determined through the momentum conservation [13, 43],

$$\sum_i \langle x_i \rangle = 1, \text{ where } \langle x_i \rangle = \int x f_i(x, Q^2)\mathrm{d}x. \tag{192}$$

---

[3] For consistency of the evolution and simplicity, we have only kept the leading-log term for the photon splitting. The non-log term corrections [57, 69] may be sizable and become relatively more relevant for a muon collider.

[4] Below the EW scale, we take $\epsilon = 10^{-6}$. For EW PDFs above μ_{EW}, we apply a more severe truncation $\epsilon = M_Z/Q$ to assure the correct double-log behavior in the $f \to fZ(f'W)$ splitting [13, 6].

The index i runs through all the flavors, including the leptons, photon, light quarks, and gluon below $\mu_{\rm EW}$, as well as neutrinos, weak gauge bosons $W^\pm/Z$ and top quark above $\mu_{\rm EW}$. The momentum conservation in Eq. (192) ensures a cancellation of the regulator ϵ between the local term $L(Q^2)$ and the integration over $x < 1-\epsilon$ in a physical observable computation.

As discussed in Sec. 2.3.1, degeneracies exist for the sea leptons, up-type and down-type quarks as in Eqs. (150-152). The leading splittings $\gamma \to \ell^+\ell^-, q\bar{q}$ result in the approximate ratio for one flavor in the moderate x region

$$f_{\bar{\ell}_{\rm val}} : f_u : f_d \sim 1 : N_c e_u^2 : N_c e_d^2 = 1 : \frac{4}{3} : \frac{1}{3}, \tag{193}$$

where $N_c = 3$. At small x, the light-quark (u- and d-type) PDFs merge due to the resummation of large and universal QCD logarithmic terms ($\alpha_s \log x$). In the relatively large x region ($x \gtrsim 0.5$), the energetic quarks tend to radiate more than leptons and f_u even becomes slightly smaller than $f_{\bar{e}}$, as a result of the additional QCD splitting $q \to qg$. For a muon beam ($\mu^\pm$), $\log(Q^2/m_e^2)/\log\big(Q^2/m_\mu^2\big) \sim 2$ at $Q \sim 30$ (50) GeV. The QCD partons (quark and gluon) in the electron beam are significantly larger than those in the muon beam, because of the accumulation of the large QCD log terms. We also note that the PDF uncertainties due to the scale choices of 30 GeV and 50 GeV are moderate, about 10% for $f_{g/e}$ and 20% for $f_{g/\mu}$. Besides, we have also estimated the QCD threshold uncertainty by varying the matching scale as $\mu_{\rm QCD} = 0.7$ GeV [18], which is less than 20% (10%) for an electron (muon) beam [45].

It is informative to consider the PDF evolution above the EW scale. We thus also show the full EW PDFs at high scales of 3 (5) TeV in Figs. 8(c) and (d). In these plots, we have summed over the non-valence fermions as

$$f_{\ell_{\rm sea}} = f_{\bar{\ell}_{\rm val}} + \sum_{i\neq\ell_{\rm val}}^{N_\ell} (f_{\ell_i} + f_{\bar{\ell}_i}),\quad f_\nu = \sum_i^{N_\ell} (f_{\nu_i} + f_{\bar{\nu}_i}),\quad f_q = \sum_i^{N_u} (f_{u_i} + f_{\bar{u}_i}) + \sum_i^{N_d} (f_{d_i} + f_{\bar{d}_i}). \tag{194}$$

Here, $N_u = 3$ as the top quark becomes active as well. The neutral-current EW PDFs include γ, Z, and γZ-mixing. The longitudinal PDFs (W_L, Z_L) were known at the leading order as the Effective W Approximation [10, 11, 71], which do not run with the scale Q, as an explicit realization of the Bjorken-scaling restoration. We find that the EW corrections from W/Z to the light particle PDFs at a high scale above TeV can be as large as 50%

(100%) for $f_{d/e}$ ($f_{d/\mu}$), due to the relatively large $\mathrm{SU(2)_L}$ gauge coupling compared with the electromagnetic one. The scale choices of 3 TeV and 5 TeV give uncertainty about 15% (20%) in the electron (muon) beam. The detailed comparison and potential physical impacts are left for a future publication [72].

It is interesting to ask how much momentum each parton species carries along the longitudinal beam direction. We explicitly show the average momentum fractions $\langle x_i \rangle$ carried by a parton i in Table 5. Our results are shown for both an electron beam in (a) and a muon beam in (b). Naively, the momentum ratio for the sea leptons and quarks may be estimated by Eq. (193) as

$$\frac{\langle x_q \rangle}{\langle x_{\ell_{\rm sea}} \rangle} \lesssim \frac{N_c \left[\sum_i (e_{u_i}^2 + e_{\bar{u}_i}^2) + \sum_i (e_{d_i}^2 + e_{\bar{d}_i}^2)\right]}{e_{\ell_{\rm val}}^2 + \sum_{i \neq \ell_{\rm val}} (e_{\ell_i}^2 + e_{\bar{\ell}_i}^2)} = \frac{22/3}{5}. \tag{195}$$

The actual numbers in Table 5 are smaller than this estimation, as pointed out that gluon takes part of the quark momentum fractions. After adding the gluon contribution, we obtain an improved estimation

$$\frac{\langle x_q \rangle + \langle x_g \rangle}{\langle x_{\ell_{\rm sea}} \rangle} \simeq \frac{22/3}{5}. \tag{196}$$

Table 5 gives us the relative size of each parton species and the variation at a few representative scales. In addition, we see that there is less radiation and thus less sea quark contribution for a muon beam than an electron beam.

$Q(e^\pm)$	$e_{\rm val}$	γ	$\ell_{\rm sea}$	q	g	$Q(\mu^\pm)$	$\mu_{\rm val}$	γ	$\ell_{\rm sea}$	q	g
30 GeV	96.6	3.20	0.069	0.080	0.023	30 GeV	98.2	1.72	0.019	0.024	0.0043
50 GeV	96.5	3.34	0.077	0.087	0.026	50 GeV	98.0	1.87	0.023	0.029	0.0051
M_Z	96.3	3.51	0.085	0.097	0.028	M_Z	97.9	2.06	0.028	0.035	0.0062

Table 5: The averaged momentum fractions [%] carried by each parton species for (a) an electron beam and (b) a muon beam with a few representative values of the factorization scale Q.

To make the connection with the physical scattering processes, we next compute the partonic luminosities for the initial states

$$\ell^+\ell^-,\ \gamma\ell,\ \gamma\gamma,\ qq,\ \gamma q,\ \gamma g,\ gq \text{ and } gg, \tag{197}$$

for $\sqrt{s} = 3$ TeV and 10 TeV, as shown in Fig. 9 versus $\sqrt{\tau} = \sqrt{\hat{s}/s}$, the ratio of the partonic c.m. energy and the collider energy, where the sea fermion species are summed as in Eq. (194). We see that a high-energy lepton collider can offer a broad spectrum of initial state particles. Of our particular interests, the QCD parton luminosities involving quarks and gluons increase significantly at low $\sqrt{\tau}$. The parton luminosities of $\gamma g + \gamma q$ are about 50% (20%) of that of $\gamma\gamma$ for an e^+e^- ($\mu^+\mu^-$) collider. The QCD parton luminosities of qq, gq and gg are about 2% (0.5%) of that of $\gamma\gamma$ for an e^+e^- ($\mu^+\mu^-$) collider. Correspondingly, given the stronger coupling over QED, we may expect sizable QCD cross sections at low $\sqrt{\tau}$. Our standard choice for the factorization scale is

$$Q = \sqrt{\hat{s}}/2. \tag{198}$$

Varying the scale from this default choice (solid curves) to $Q = \sqrt{\hat{s}}$ may result in a luminosity uncertainty of 20% (50%) for a photon-initiated (gluon initiated) process.

3.2.2 The standard processes and jet production

3.2.2.1 EW processes

In high-energy e^+e^- collisions, one would expect that the leading reactions are of the QED and electroweak nature, including Bhabha scattering $e^+e^- \to e^+e^-$, Compton scattering $\gamma e \to \gamma e$, and the s-channel annihilation processes for pair production $e^+e^- \to \mu^+\mu^-, q\bar{q}$ and W^+W^- once above the threshold. While the cross sections for the annihilation processes fall with the c.m. energy as $\sigma \sim \alpha^2/s$, the t-channel processes receive the collinear enhancement. Nevertheless, with a detector angular acceptance θ_{min}, the cross sections for the $2 \to 2$ t-channel processes still fall as $\sigma \sim \alpha^2/(s\,\theta^2_{\text{min}})$. Going beyond the fixed-order calculations, the potentially large collinear logarithms ($\log\theta^2$) need to be resummed, leading to the appropriate description of the parton distribution functions (PDFs), as presented

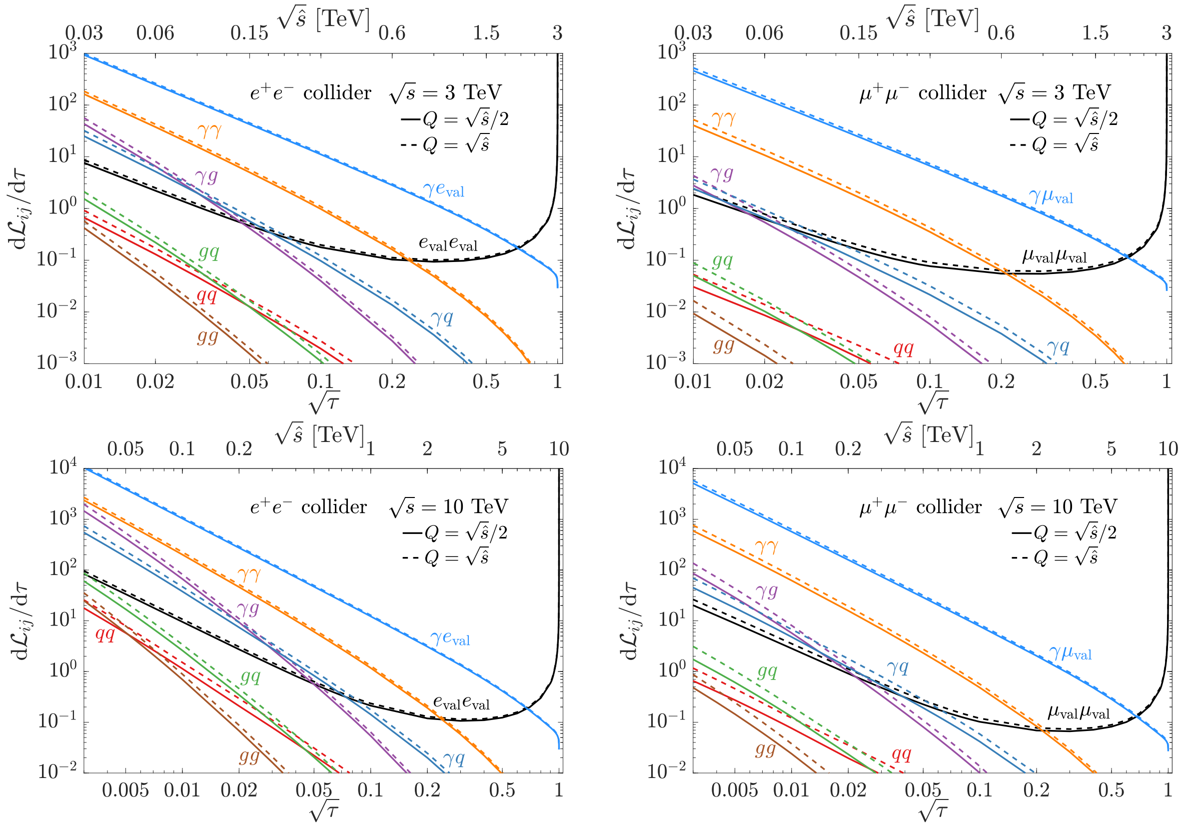

Figure 9: Parton luminosities $\mathrm{d}\mathcal{L}_{ij}/\mathrm{d}\tau$ for (a) an e^+e^- collider at $\sqrt{s} = 3$ TeV, (b) a $\mu^+\mu^-$ collider at $\sqrt{s} = 3$ TeV, (c) an e^+e^- collider at $\sqrt{s} = 10$ TeV, and (d) a $\mu^+\mu^-$ collider at $\sqrt{s} = 10$ TeV. The factorization scale is chosen as $Q = \sqrt{\hat{s}}/2$ (solid curves) and $\sqrt{\hat{s}}$ (dashed curves).

in the previous section. As such, there will be substantial contributions coming from partonic scattering processes initiated by those in Eq. (197), far below the collider c.m. energy. Throughout this work, the partonic cross sections are calculated at the leading order with the general purpose event generator MadGraph5 v2.6.7 [63]. The annihilation processes with the initial-state radiation (ISR) are calculated with Whizard v2.8.5 [64].

We first present some leading order production cross sections of typical electroweak processes in Fig. 10 versus the collider c.m. energy for both an e^+e^- collider (left panels) and a $\mu^+\mu^-$ collider (right panels), including the effects of ISR [73]. In Fig. 10, the dashed (falling) curves represent the Bhabha scattering and annihilation processes

$$\ell^+\ell^- \to \ell^+\ell^-,\ \tau^+\tau^-,\ q\bar{q} \text{ and } W^+W^-. \tag{199}$$

The cross sections scale as $1/s$, with the characteristic kinematics of the final-state pair invariant mass close to the collider energy $m_{ij} \approx \sqrt{s}$. At high energies, the ISR effects reduce the effective partonic collision energy $\hat{s}$ and thus increase the cross sections $\sim 1/\hat{s}$. For illustration, we compare the result without ISR for $\ell^+\ell^- \to \tau^+\tau^-$ by the dotted curves in the panels. Typically, the effective reduction is about a factor of 20%−80% (10%−40%) for an electron (muon) collider. The radiative returns to the Z resonant production also enhance the light-particle cross sections significantly. The ISR effects for light-particle production ($\tau^+\tau^-$, $q\bar{q}$) are thus larger than the massive one (W^+W^-), because of the lower threshold, *i.e.*, $\hat{s} > m_{ij}^2$ versus $\hat{s} > (2M_W)^2$.

In considering the QED fusion processes, the initial state partons present an infrared enhancement at low m_{ij} and the two-parton cross section scales as

$$\sigma \sim \frac{\alpha^2}{m_{ij}^2}\left(\frac{\alpha}{2\pi}\log\frac{Q^2}{m_\ell^2}\right)^2. \tag{200}$$

To separate the hadronic activities with the low-momentum transfer from the hard processes of our current interests, we impose the following basic acceptance cuts on the outgoing particles in the transverse momentum (p_T^j), the di-jet invariant mass and the pseudo-rapidity (η_j) in the lab frame

$$p_T^j > \left(4 + \frac{\sqrt{s}}{3\ \text{TeV}}\right)\ \text{GeV}, \quad m_{ij} > 20\ \text{GeV}, \quad |\eta_j| < 3.13\ (2.44). \tag{201}$$

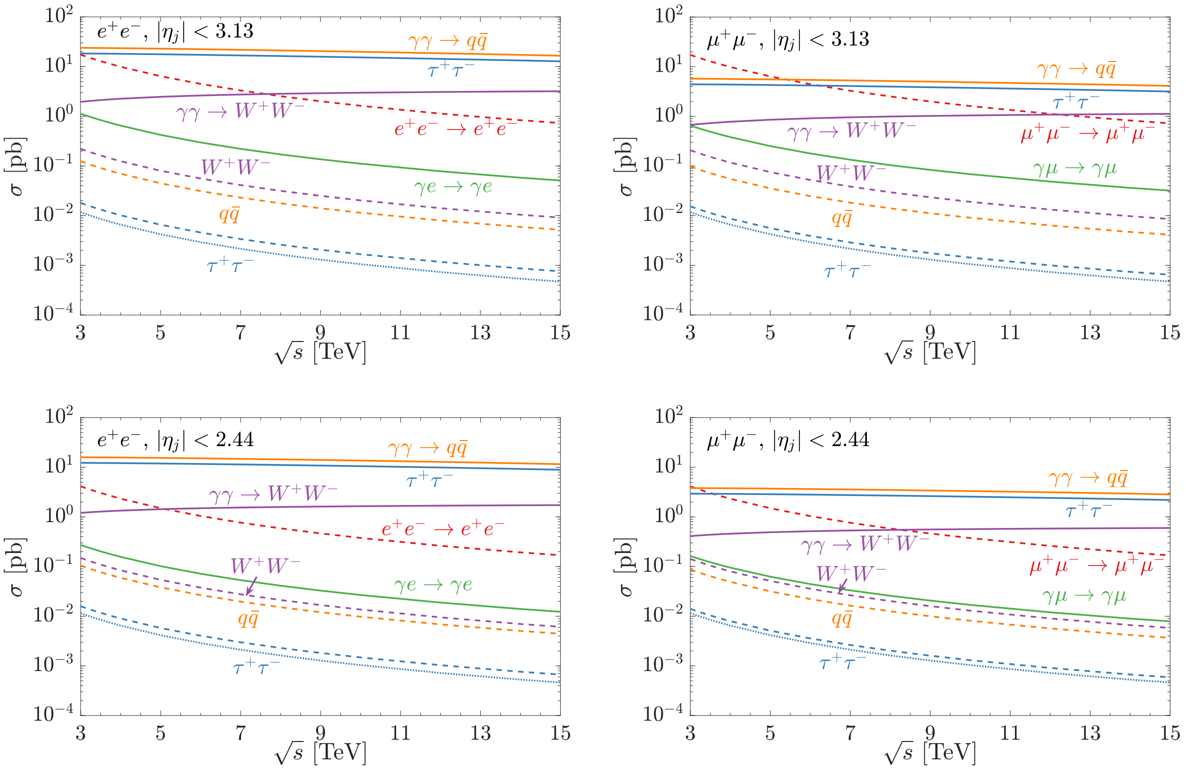

Figure 10: Cross sections for the annihilation processes versus the collider c.m. energy for an e^+e^- collider (left panels) and a $\mu^+\mu^-$ collider (right panels) with basic acceptance cuts in Eq. (201). The downward dashed (dotted for $\tau^+\tau^-$) curves indicate the corresponding Bhabha scattering and $\ell^+\ell^-$ annihilation processes with (without) ISR.

The energy-dependent cut on the final state p_T^j is to uniformly control the collinear logs of the form $(\alpha_s/\pi)\log\big(p_T^j/\sqrt{s}\big)$, numerically motivated by a CLIC study [74]. The pseudo-rapidity cut corresponds to an angle with respect to the beam in the lab frame $\theta_j \sim 5(10$, in accordance with the detector coverage. For an equal footing comparison, the same acceptance cuts have been applied to the Bhabha scattering and annihilation processes in Fig. 10 as well.

In Fig. 10, the solid lines show the Compton scattering and the fusion processes

$$\gamma\ell \to \gamma\ell; \quad \gamma\gamma \to \ell^+\ell^-,\ q\bar{q}\ (u,d,c,s,b),\ \text{and } W^+W^-, \tag{202}$$

by exploiting the EPA in Eq. (190). The upper panels and lower panels are with a different rapidity (angle) cut as in Eq. (201). The cross section for the Compton scattering ($\gamma\ell$) also falls as $\alpha^2/(s\,\theta^2)$, as evidenced from the figures. The cross sections for the other fusion processes increase with energy logarithmically and decreases with p_T (or m_{ij}) as in Eq. (200). The angular dependence is much weaker than $1/\theta^2$ and becomes roughly like η^2 due to the boost factor. We see that the fermion pair production can be larger than that of the WW channel, which is known to be one of the leading channels for high-energy leptonic collisions. For the sake of illustration, we have only included the leading contributions from $\gamma\gamma$ fusion in Fig. 10. We remind the reader that for the W^+W^- production at these energies, the sub-leading channel $\gamma Z \to W^+W^-$ contributes to about 20% (40%), and $ZZ, W^+W^- \to W^+W^-$ about 10% (30%) concerning the $\gamma\gamma$ contribution at an e^+e^- ($\mu^+\mu^-$) collider. They are neglected in our comparison for simplicity, which does not change the conclusion [72].

3.2.2.2 Jet production

Before predicting the jet production rate, it is important to remind the reader that at the low-momentum transfer, the majority of the events come from the hadronic production of the photon-induced processes, constituting the substantial backgrounds at the detector. This was pointed out in Refs. [75, 76] for e^+e^- collisions in the context of beamstrahlung, and have been since extensively studied [77, 78]. Similar to the behavior of the total cross sections in hadronic collisions [79, 80], the photon-induced hadronic cross section moderately increases with energy. Due to the non-perturbative nature of the low-energy reactions, one would have to model the scattering. We estimate the total cross sections by adopting the two well-studied parameterizations for $\gamma\gamma \to$ hadrons in Pythia [81, 82],

$$\hat{\sigma}_{\gamma\gamma}(\hat{s}) \approx (211 \text{ nb})\ \hat{s}^{0.0808} + (215 \text{ nb})\ \hat{s}^{-0.4525}, \tag{203}$$

and by a SLAC group [77],

$$\hat{\sigma}_{\gamma\gamma}(\hat{s}) \approx \begin{cases} 490 \text{ nb} & (0.3 \text{ GeV} < \sqrt{\hat{s}} < 1.5 \text{ GeV}), \\ 200 \text{ nb}\ [1 + 0.0063(\ln \hat{s})^{2.1} + 1.96\ \hat{s}^{-0.37}] & (\sqrt{\hat{s}} \geq 1.5 \text{ GeV}), \end{cases} \tag{204}$$

where $\hat{s}$ is the c.m. energy squared for the $\gamma\gamma$ collisions in units of GeV^2. We show the results for the photon-induced cross sections in Fig. 11. We see that the $\gamma\gamma$ cross section may reach the order of micro-barns (μb) at the TeV c.m. energies. Folding in the $\gamma\gamma$ luminosity in electron/muon collisions,[5] this brings the cross section down to the level of one hundred or a few tens of nano-barns at high-energy electron or muon colliders. The axis on the right indicates the event rate in kHz, assuming an instantaneous luminosity of 10^{35}/cm^2/s. Those hadronic final states dominate the event shape in this low energy regime. However, those events are typically populated at very small scattering angles and low transverse momenta below a few GeV [74]. While they should be taken into account for the detector design and the experimentation, they would not have much impact on the high-p_T physics of our current consideration.

Particularly important channels of our current interests are the jet production via the fusion mechanism, which would be the dominant phenomena at low $\sqrt{\hat{s}}$. The production channels include

$$\gamma\gamma \to q\bar{q},\ \gamma g \to q\bar{q},\ \gamma q \to gq, \tag{205}$$

$$qq \to qq\ (gg),\ gq \to gq \text{ and } gg \to gg\ (q\bar{q}), \tag{206}$$

where q includes d, u, s, c, b and the possible anti-quarks as well. The PDFs and the corresponding partonic luminosities are already shown in Figs. 8 and 9 with the full DGLAP

---

[5] Here we have neglected the effects of beamstrahlung. This is justifiable for the large muon mass and for the circular collider designs.

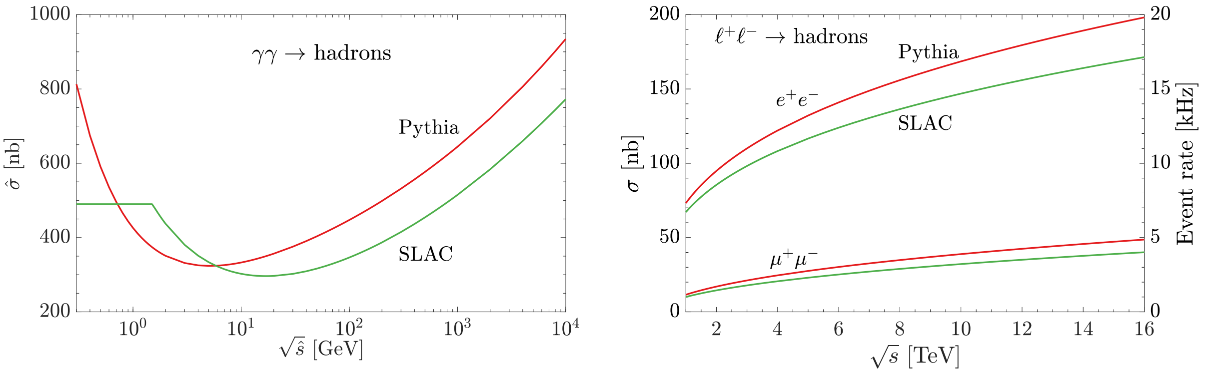

Figure 11: The photonic (a) and leptonic (b) cross sections for photon-induced hadronic production at high-energy lepton colliders. We adopted the models by Pythia [81, 82] or SLAC [77] parameterizations as stated in the text.

evolution at a double-log accuracy. We present the cross sections for di-jet production from initial states of photons, quarks, and gluons versus the collider c.m. energy $\sqrt{s} = 3 - 15$ TeV at an e^+e^- collider (left panels) and a $\mu^+\mu^-$ collider (right panels) in Fig. 12, subject to the acceptance cuts in Eq. (201) shown by the upper and lower panels. The patonic QCD jet cross sections are calculated at the leading order with MadGraph5 v2.6.7 [63] and cross-checked with MCFM v9.1 [83] and Sherpa v2.2.10 [84].

The standard factorization scale is chosen to be $Q = \sqrt{\hat{s}}/2$, while varying the scale to $Q = \sqrt{\hat{s}}$ gives a 6∼15% (30∼40%) enhancement of the cross sections for an e^+e^- ($\mu^+\mu^-$) collider, which characterizes the scale uncertainty. The rather large difference resulting from the scale choice is owing to the large $\alpha_s \log(Q^2)$ resummation. It is important to note that, even originated from the photon splitting to quarks and then subsequently to gluons, the gluon and quark initiated processes exceed the photon fusion in the di-jet production rates by two (one) orders of magnitude for the electron (muon) collider. This is the result of large QCD resummation and the g/q multiplicity. Depending on the acceptance cuts, the crossover of the gg fusion to the gq scattering happens around $3 - 4$ TeV for the electron collider and $8 - 12$ TeV for the muon collider. For the same reason, the $\gamma g \to jj$ process

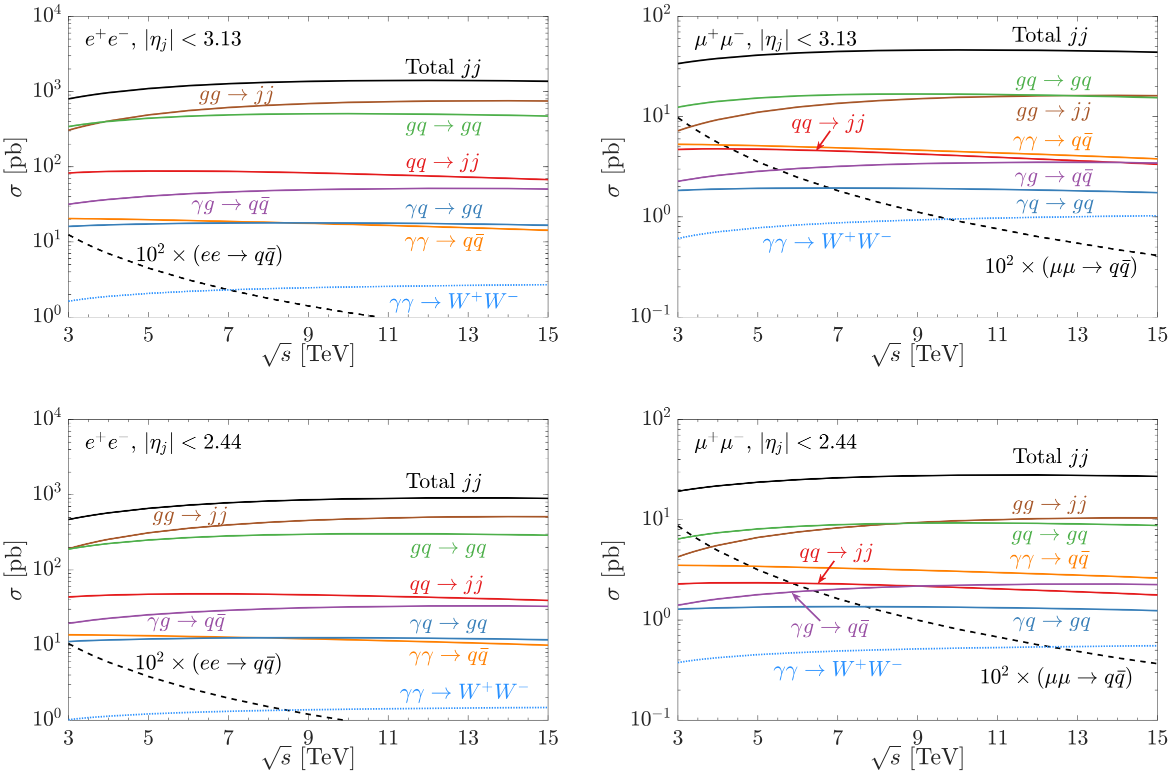

Figure 12: Cross sections for di-jet (or W^+W^-) production ($j = q, g$) versus the collider c.m. energy for an e^+e^- collider (left panels) and a $\mu^+\mu^-$ collider (right panels) with basic acceptance cuts in Eq. (201).

grows faster over the energy than the $\gamma\gamma \to jj$ fusion and takes over for the electron collider. Compared with the photon-initiated processes, the angular dependence of the QCD jet cross sections is much stronger, due to the large QCD collinear logarithms $\alpha_s \log \theta^2$ effectively resummed by the DGLAP equations.

There are a number of improvements for the results shown here with respect to the QED calculations by EPA as in Fig. 10. First, the higher-order cascade splittings $\gamma \to \ell^+\ell^-, q\bar{q}$ have been included, which will carry away a part of the momentum fraction from the initial photon and is roughly 5% for an electron beam, and 3% for a muon beam, estimated from Table 5. Second, in our treatment of the full DGLAP evolution, the running effect of the QED coupling $\alpha(Q)$ is properly taken into account, with the boundary condition at the lepton mass set to be $\alpha(m_e^2) = 1/137$ ($\alpha(m_\mu^2) = 1/136$) and proper matching cross the mass thresholds. As expected, both effects tend to reduce the rate for photon-initiated processes with respect to the naive EPA calculations. As such, the cross section for $\gamma\gamma \to q\bar{q}$ receives about 16% (8%) reduction over the EPA results for electron (muon) colliders evaluated with the fixed value $\alpha = 1/132.5$. Finally, we note that the other EW VBF contributions such as $\gamma Z, W^+W^-, W^\pm Z \to q\bar{q}'$ are sub-leading and contribute less than 1%, due to the suppression of the EW threshold above M_Z or $2M_W$.

One of the most striking aspects for a high-energy lepton collider is the combination of two characteristically different production mechanisms: the direct $e^+e^-/\mu^+\mu^-$ annihilation channels and the fusion processes. The former carries the full collider energy to reach a high threshold and the latter starts from the low energy to scan over the full spectrum. These distinctive kinematic features can be best shown by the invariant mass (m_{ij}) of the final state di-jet system as in the upper panels of Fig. 13 at $\sqrt{s} = 3$ TeV for e^+e^- and 10 TeV for $\mu^+\mu^-$, respectively. We see the clear separation of events from these two classes of reactions, peaked around the low threshold in m_{ij} for the partonic fusion processes, and sharply peaked at the beam collision energy $\sqrt{s}$ for the annihilation process (a factor of 100 is multiplied here because of the smaller production rate). The long tail in low m_{ij} for the annihilation process is due to the ISR, followed by another peek around the Z resonance from the radiative return $\ell^+\ell^- \to Z \to jj$. In the 10 TeV $\mu^+\mu^-$ collider case, the m_{ij} distribution has a threshold kink around $m_{ij} \sim \sqrt{s}e^{-\eta} \approx 870$ GeV, which is from the effect

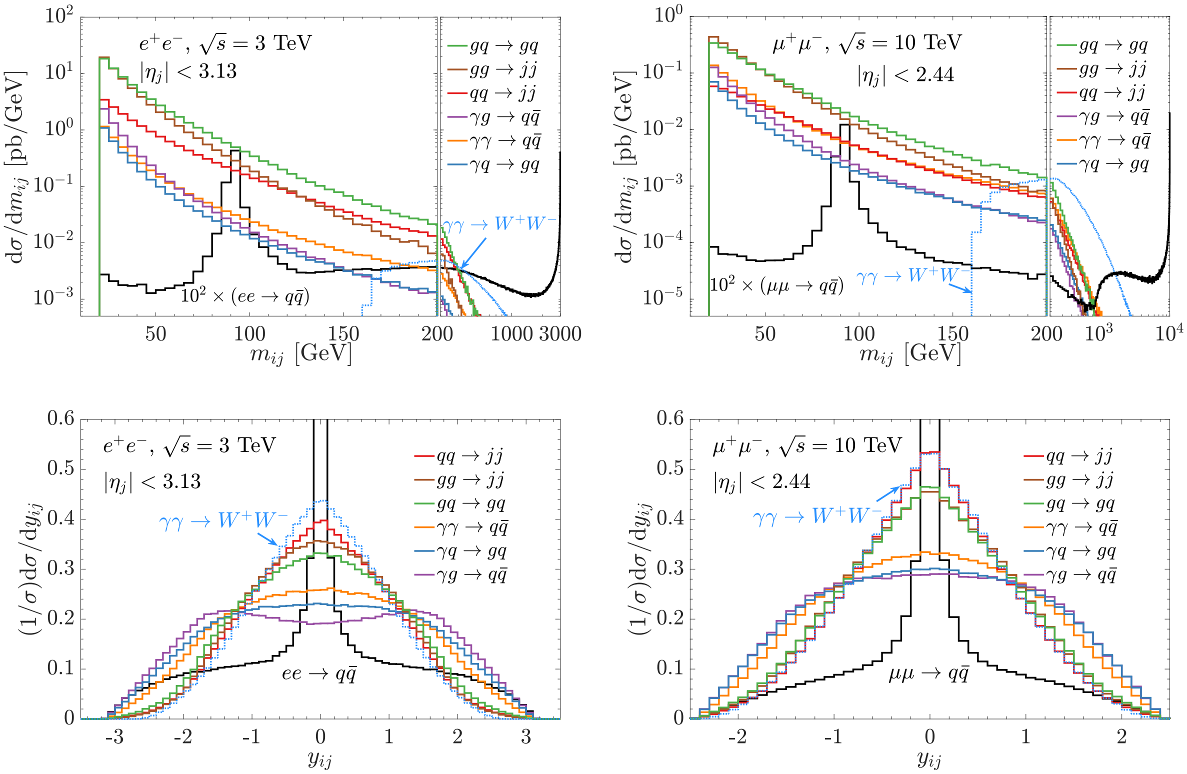

Figure 13: Invariant mass (m_{ij}, upper panels) and rapidity (y_{ij}, lower panels) distributions for the di-jet (or W^+W^-) system from various sub-processes for an e^+e^- collider at $\sqrt{s} = 3$ TeV (left panels), and a $\mu^+\mu^-$ collider at $\sqrt{s} = 10$ TeV (right panels), respectively.

of the angular cut. This is not notable in the e^+e^- collider case with the cut $|\eta| < 3.13$, because the location $m_{ij} \sim \sqrt{s}e^{-\eta} = 130$ GeV is diluted by the falling from the resonant Z peak. We also include a leading production channel $\gamma\gamma \to W^+W^-$ in high-energy leptonic collisions for comparison. We see that the jet production is overwhelmingly larger until the kinematical region with a high invariant mass $m_{ij} \gtrsim 200$ GeV. The second distinctive kinematic feature manifests itself in the rapidity distributions of the di-jet system shown in the lower panels of Fig. 13 for e^+e^- and $\mu^+\mu^-$, where the annihilation process is very central with back-to-back di-jets peaked at $y_{ij} \sim \log(x_1/x_2) \approx 0$, spreading out by the ISR. In comparison, the fusion process spread out, especially for the processes involving a photon due to the large imbalance between x_1 and x_2. The distribution for $\gamma\gamma \to W^+W^-$ is also relatively more central.

Finally, we present some kinematic distributions of the inclusive jets in Fig. 14, the transverse momentum (p_T^j, upper panels), the jet energy (E_j, middle panels), and the pseudo-rapidity (η_j, lower panels), at a 3 TeV e^+e^- (left panels) and a 10 TeV $\mu^+\mu^-$ (right panels) collider, respectively.[6] The p_T^j distributions in Fig. 14 resemble very similar features as those of m_{ij} in Fig. 13, with the Jacobian peaks around the $p_T^j \sim m_{ij}/2$ for the fusion processes, and peaked sharply at $\sqrt{s}/2$ and $M_Z/2$ for the annihilation processes. We once again see the dominant QCD jet production over the W^+W^- channel until the kinematical region with a high transverse momentum $p_T^j > 60$ GeV. We note that there is a peculiar peak structure in the p_T^j distribution for the annihilation processes. After the peak at $\sqrt{s}/2$, it falls and rises again around $p_T^j \sim \sqrt{s}e^{-\eta} = 130$ (870) GeV, the same location as the m_{ij} kink. The dip around 300 GeV for the 10 TeV $\mu^+\mu^-$ collider case is just the cross point between the falling from the Jacobi peak $M_Z/2$ and rising to the cut point $\sqrt{s}e^{-\eta}$. Furthermore, we see from the energy distributions that the W^+W^- channel takes over after its energy above 400 GeV (200 GeV) for the e^+e^- collider ($\mu^+\mu^-$ collider). The inclusive pseudo-rapidity distributions in Fig. 14 demonstrate that the QCD partonic contributions are mostly forward-backward, while those of $\gamma\gamma$ and $\gamma q(g)$ are more isotropic, and the 2-body annihilation process via an s-channel vector boson exchange presents the typical $(1 + \cos^2\theta)$ distribution.

---

[6] We remind the reader that inclusive jets include any jets in an event. That is to say, each di-jet event is counted twice.

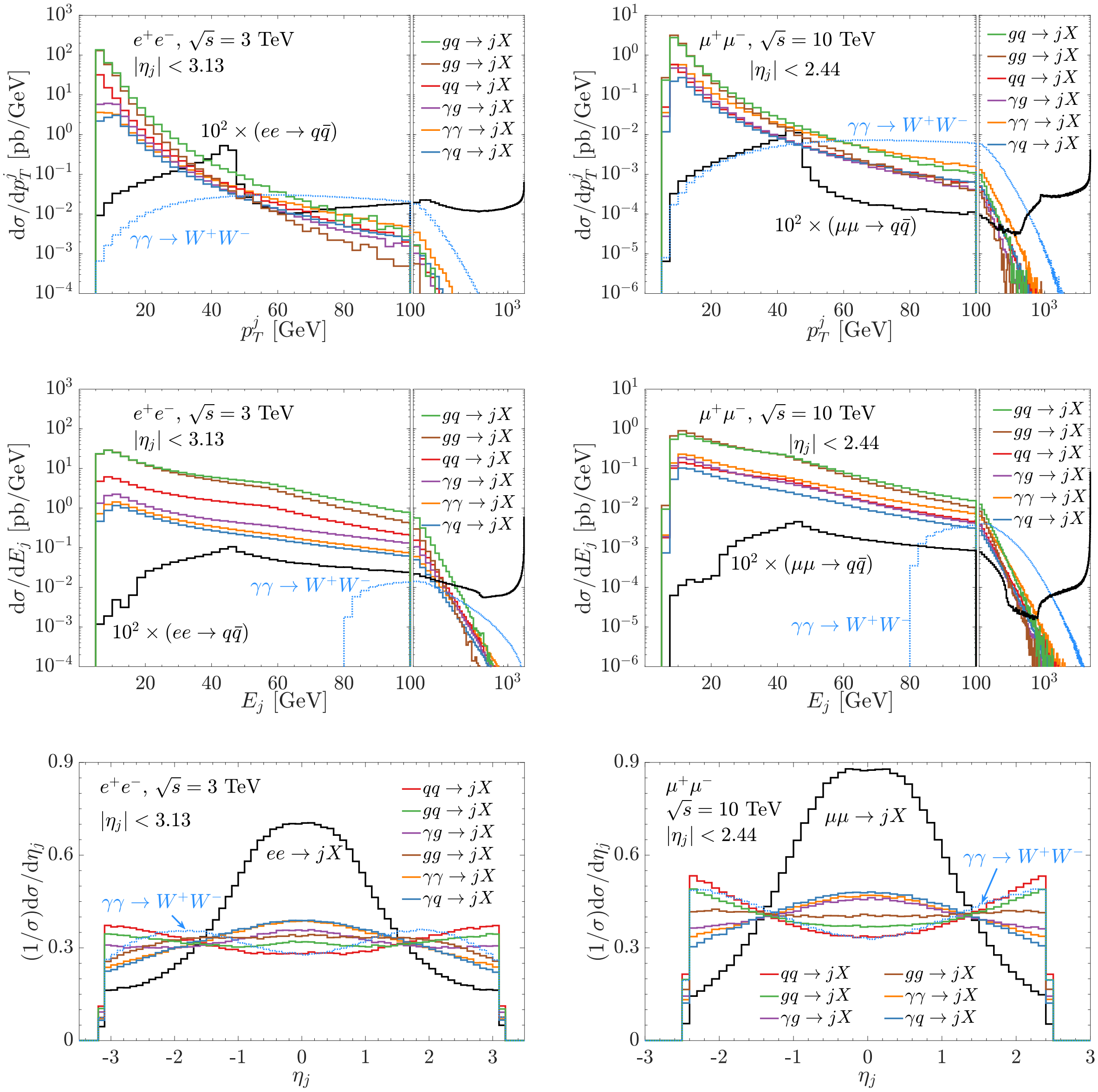

Figure 14: Inclusive jet (or W) distributions for transverse momentum (p_T^j, upper panels), jet energy (E_j, middle panels) and the normalized pseudo-rapidity (η_j, lower panels) in various sub-processes for an e^+e^- collider at $\sqrt{s} = 3$ TeV (left panels), and a $\mu^+\mu^-$ collider at $\sqrt{s} = 10$ TeV (right panels), respectively.

3.2.3 Summary

In high-energy leptonic collisions, such as at a multi-TeV muon collider, the collinear splittings of electroweak gauge bosons and leptons are the dominant phenomena, and thus the scattering processes should be formulated in terms of the EW parton distribution functions (EW PDFs). We complete this formalism in the Standard Model to include the QCD sector and evaluate the quark and gluon PDFs inside a lepton by solving the fully-coupled DGLAP equations at the double-log accuracy, as presented in Chapter 2. We see that, dominantly from the photon splitting, there are significant gluon and quark contents in high energy lepton beams as shown in Figs. 8 and 9. In comparison, while the photon PDF in an electron is larger than that in a muon by about a factor of two below the EW scale, the quark/gluon PDFs are substantially larger in an electron than that in a muon due to the large log resummation from QCD splittings. The subsequent splittings also make a notable effect as ISR on the lepton beam profile. The initial state of quarks and gluons will lead to QCD processes with large cross sections and will dominate the overall event shape in high-energy leptonic collisions with low and moderate transverse momenta. They may also induce the production of new colored particles [66].

In Sec. 3.2.2, we studied the production cross sections in our PDF framework. We compared the standard QED processes in leptonic collisions at multi-TeV energies and showed the dominance of the fusion mechanism in Fig. 10. We then gave the prediction for jet production of quarks and gluons in Fig. 12. We found that, as expected, the QCD jet production initiated by q/g yields the dominant processes, about two orders (one order) of magnitude larger than the EW fermion pair production at an e^+e^- ($\mu^+\mu^-$) collider, reaching a large production rate of about 1 nb (50 pb), with a moderate acceptance cut. We summarize some representative cross sections in e^+e^- ($\mu^+\mu^-$) collisions for a variety of energies in Table 6. The total cross sections include both annihilation and fusion processes. The fusions to W^+W^- and $t\bar{t}$ only include the dominated $\gamma\gamma$ initialized processes [6]. The kinematic cuts in Eq. (201) are employed to the W boson and top quarks, as well. To have a more complete picture with respect to the hadronic production at low scattering energies, we also calculated the total cross section for the photon-induced hadronic production adopting two

e^+e^- $[\sqrt{s}]$	σ [pb] jj	e^+e^-	$\tau^+\tau^-$	W^+W^-	$t\bar{t}$
3 TeV	800(470)	33(15)	16(11)	1.9(1.2)	0.035(0.032)
6 TeV	1200(730)	19(11)	15(10)	2.3(1.3)	0.023(0.019)
10 TeV	1400(880)	15(9.5)	13(9.1)	2.5(1.4)	0.023(0.017)
14 TeV	1400(910)	12(8.2)	11(8.0)	2.7(1.5)	0.024(0.017)

$\mu^+\mu^-$ $[\sqrt{s}]$	σ [pb] jj	$\mu^+\mu^-$	$\tau^+\tau^-$	W^+W^-	$t\bar{t}$
3 TeV	34(19)	21(6.9)	4.1(2.7)	0.82(0.52)	0.027(0.025)
6 TeV	43(25)	8.3(3.7)	3.9(2.6)	0.89(0.51)	0.012(0.011)
10 TeV	46(28)	5.1(2.7)	3.5(2.4)	0.97(0.54)	0.010(0.0078)
14 TeV	45(28)	3.8(2.3)	3.0(2.1)	1.0(0.56)	0.010(0.0073)

Table 6: Some representative cross sections in e^+e^- and $\mu^+\mu^-$ collisions including both annihilation and fusion for a variety of energies. We have included the ISR for the annihilation processes. The fusion to $W^+W^-, t\bar{t}$ cross sections only include the dominated $\gamma\gamma$ initialized processes with the resummed γ PDF. The acceptance cuts in Eq. (201) are applied to the final-state particles, including the W^+W^- and $t\bar{t}$ as well. The numbers outside (inside) of the parentheses correspond cross sections with the acceptance cut $|\eta_j| < 3.13$ ($|\eta_j| < 2.44$).

models: Pythia and “SLAC”, as shown in Fig. 11. We see that the cross sections can reach the level of one hundred (a few tens) of nano-barns at high-energy electron (muon) colliders. Although the rate for the hadronic production is high, the events populate in the low p_T region typically below a few GeV.

Of particular interests are the differential distributions for di-jet system in Fig. 13, and for jet-inclusive in Fig. 14. The general features emerge again that the e^+e^- ($\mu^+\mu^-$) annihilation is mostly central with $\hat{s} \approx s$, the fusion processes populate at $\sqrt{\hat{s}} \approx m_{ij}$, and QCD jet production dominates up to $p_T^j \approx 60$ GeV. Since the events tend to populate near the threshold, the photon splitting governs the fate, especially below the EW scale, while the heavy EW gauge bosons do lead to substantial contribution at high scales.

As a final remark, our approach to the quark/gluon PDFs induced by the EW interactions is equally applicable to hadronic collisions with quarks as the radiation source. Since the simulations for photon-induced high-p_T jet events from perturbative QCD calculations do not exist in the current event-generator packages, our formalism should be adopted by the event generators to simulate SM processes and the leading QCD backgrounds at lepton colliders.

4.0 Yukawa couplings of the second generation fermions

The Standard Model (SM) of elementary particle physics is constructed based on a non-Abelian gauge theory of $\mathrm{SU(3)_C} \otimes \mathrm{SU(2)_L} \otimes \mathrm{U(1)_Y}$, that has been experimentally verified with a high accuracy to the highest energies accessible to date [85]. On the other hand, there is mounting evidence from observations for the need of new physics beyond the SM, such as the dark matter, neutrino mass generation, and the matter/antimatter asymmetry. The Higgs boson, which is directly related to the SM mass generation mechanism, is believed to be the portal to new physics. In this chapter, I suggest two approaches to measure the Muon-Higgs coupling and the Charm-Higgs coupling. The results are reported in Ref. [86, 87].

4.1 Precision test of the Muon-Higgs coupling at a high-energy muon collider

4.1.1 Introduction

Unlike the past decades, at the moment we are lacking well-defined traces of where to look for new physics. While there are many loose ends in the SM of particle physics and cosmology, however, there is no clear indication at what energy scales new phenomena would appear below the Planck scale. This gives us the task to use all available tools to search for new phenomena, particularly all the discovered particles as vehicles for our searches. Especially, the scalar boson discovered in 2012 [2, 88] which closely resembles the SM Higgs boson is very well suited for beyond the Standard Model (BSM) searches [89]. Currently, the couplings of the Higgs boson to the third generation SM fermions have been established with a precision of $10\% - 20\%$ (for an overview of the current status and projections, see *e.g.* [90]). The high-luminosity phase of the LHC will study the properties of this particle and its couplings to a precision at a few percent level [91, 92]. The next collider facility will most likely be a Higgs factory [93, 94] in the form of an electron-positron collider running at or slightly above the ZH threshold, such as the International Linear Collider (ILC) [95, 96], the Future Circular Collider (FCC-ee) [97], the Circular Electron-Positron Collider (CEPC) [98], or the Compact Linear Collider (CLIC) at higher energies [99, 100] to achieve a per-mille level accuracy for the Higgs couplings to $W^+W^-, ZZ, \gamma\gamma, gg$ and $b\bar{b}, \tau\bar{\tau}, c\bar{c}$, as well as the invisible decay mode.

However, there will still be parts of the Higgs sector left unexplored or measured with low precision because it can only be probed with very rare processes for which there are too low rates at a Higgs factory and the LHC measurements (or searches) suffer from large systematic uncertainties due to the challenging experimental environment. To this class belong the couplings to the first and second generations of fermions. The Higgs mechanism in the SM provides the mass for all elementary particles, and thus specifies the form of their interactions associated with the electroweak symmetry breaking (EWSB). With only a single $\mathrm{SU}(2)_L$ Higgs doublet and the minimal set of interactions at the renormalizable level, the Yukawa couplings of SM fermions are proportional to the respective particle masses, and thus exhibit a large hierarchy. It would be desirable to achieve a better precision for the measurement of the Yukawa couplings of the light fermions, since this would be a direct and important test whether the Higgs mechanism as implemented in the SM provides the masses for all SM fermions, or whether it is a mixture of two (or more) mechanisms. Because of the small Yukawa couplings for light fermions predicted in the SM, any small deviation due to BSM physics may result in a relatively large modification to those couplings.

The next target is the Higgs-muon coupling. The recent evidence for the $H \to \mu^+\mu^-$ decay at ATLAS and CMS indicates that the Yukawa coupling is present within the predicted order of magnitude [101, 102]. However, the results are not yet at the 5σ level for discovery, and thus leaves room for $O(100\%)$ corrections. Also, the measurement is insensitive to the sign of the coupling. According to the current experimental projections, by the end of the high-luminosity runs of the LHC in the late 2030s the muon Yukawa coupling could be measured with an accuracy of about several tens of percent [103] in a model-dependent way. This situation might not be improved very much neither at the Higgs factory due to the limited rate, nor at a high-energy hadron collider like the FCC-hh [104, 105], due to the systematics and the model-dependence. Thanks to the technological development [68], a renewed idea that has recently gathered much momentum is the option of a high-energy muon collider that could reach the multi-(tens of) TeV regime with very high luminosity [106, 107, 108]. It has been demonstrated in the recent literature that a high-energy muon collider has great potential for new physics searches at the energy frontier from direct $\mu^+\mu^-$ annihilation and a broad reach for new physics from the rich partonic channels [6, 60, 109, 7, 45], as well as precision measurements for SM physics [110] and beyond [111, 112, 113, 114, 115, 116, 117, 118, 119]. Of particular importance is the connection between the muon collider expectation and the tantalizing hint for new physics from the muon $g-2$ measurement [120, 121].

In this section, we propose one unique measurement and BSM search in the Higgs sector which serves as a paradigm example for exploiting a high-energy muon collider, namely the direct measurement of the muon Yukawa coupling. At a high-energy $\mu^+\mu^-$ collider, one probes the coupling at a much higher energy scale and it may reach some sensitivity to new physics with scale-dependent effects. Unlike the precision measurements at low energies where one probes the virtual quantum effects, our proposal is to directly measure the muon coupling associated with its mass generation. Our search strategy is generally applicable to other new physics searches involving final states of charged leptons and jets, that may provide general guidance for future considerations.

4.1.2 EFT Description of an Anomalous Muon Yukawa Coupling

In a purely phenomenological ansatz, if small modifications of the SM Lagrangian exist, they should be detectable most easily in interactions which are accidentally suppressed in the SM, and at the same time are unaffected by large radiative corrections. The muon mass and the associated production and decay processes perfectly fit this scenario[1]. In this spirit, we introduce representative new interactions in form of a modification of this muon mass parameter, without referencing a specific model context. The modification is supposed to be tiny in absolute terms, but nevertheless becomes significant if compared with the SM muon Yukawa coupling which has a numerical value of less than 10^{-3}. A few well-motivated physics scenarios with a modification of the SM can be constructed as we will discuss next. They may describe rather different underlying dynamics, but represent physically equivalent

---

[1] For illustration, we show the effect of the running of the muon Yukawa coupling in Appx. C

calculational frameworks in the perturbative regime.

4.1.2.1 The Yukawa interaction in the HEFT parameterization

In the Higgs Effective Theory (HEFT) [122, 123, 124, 125, 126, 127] or non-linear chiral-Lagrangian description, the scalar sector consists of a physical singlet Higgs boson together with unphysical triplet Goldstone bosons associated with the EW symmetry breaking. The latter isolate the contributions of longitudinally polarized vector bosons. This property can be formalized as the Goldstone-boson Equivalence Theorem (GBET) [71, 128]:

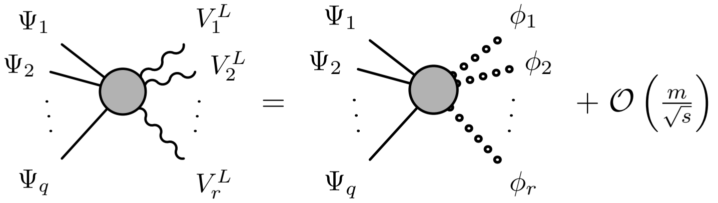

Here, V_k^L denotes a longitudinal EW vector boson, ϕ_k the corresponding Goldstone boson, and Ψ_k any possible SM fermion. This denotes that fact that matrix elements for multi-boson final states including vector bosons are dominated in the high-energy limit by their longitudinal component

$$\varepsilon_L^\mu(p) = \frac{p^\mu}{m} + v_p^\mu \quad , \tag{207}$$

where $v_p^\mu \sim \mathcal{O}(m/\sqrt{s})$ is a four-vector depending on the boson momentum. According to [129] the GBET in an EFT framework takes the form

$$\begin{aligned}\mathcal{M}(V_1^L, \dots, V_r^L, \mathbf{\Phi}) = &\left(\prod_j^r \pm i\omega_j\right) \mathcal{M}^0(\phi_1, \dots, \phi_r, \mathbf{\Phi}) \\ &+ \mathcal{O}\left(\frac{m}{\sqrt{s}}\right) + \mathcal{O}\left(\frac{\sqrt{s}}{\Lambda}\right)^{N+1} + \mathcal{O}\left(g, g'\right) \quad ,\end{aligned} \tag{208}$$

where $\mathcal{M}^0$ is the leading order of the matrix element in g, g', and $\mathcal{O}\left(g, g'\right)$ denotes terms, which are suppressed by g, g' in comparison to this leading term. The ω_j are specific phases that differ between initial and final states within the amplitude. In this framework, the matrix elements appear not only as series expansions in the gauge couplings, but also in $\sqrt{s}/\Lambda$, which are usually truncated after some finite order N. The high-energy scale Λ of any such bottom-up EFT corresponds to a specific scale of BSM models, e.g. a reference mass of a single heavy new particle. All longitudinal gauge bosons V_i^L can be replaced by the corresponding Goldstone bosons ϕ_i at high energies within the accuracy goal of the EFT. The results will match at the leading order in g and g'.

In the present context, we can rewrite a modified muon Yukawa coupling as a gauge-invariant operator in the HEFT Lagrangian, and conclude that this new interaction should cause extra contributions to the production of multiple vector bosons in association with the Higgs boson which rise with energy. By construction, these contributions exactly reproduce the effect of spoiled gauge cancellations in unitary gauge, as computed by automated programs.

In the non-linear representation we introduce a field U

$$U = e^{i\phi^a\tau_a/v} \quad \text{with} \quad \phi^a\tau_a = \sqrt{2}\begin{pmatrix} \frac{\phi^0}{\sqrt{2}} & \phi^+ \\ \phi^- & -\frac{\phi^0}{\sqrt{2}} \end{pmatrix} \quad , \tag{209}$$

and its covariant derivative

$$D_\mu U = \partial_\mu U + igW_\mu U - i\frac{g'}{2}B_\mu U\tau_3 \quad \text{with} \quad W_\mu = \frac{1}{2}\tau_a W_\mu^a \quad , \tag{210}$$

where τ_a denote the usual Pauli matrices and $\{\phi^+, \phi^-, \phi^0\}$ are the Goldstone bosons to the corresponding gauge bosons $\{W^+, W^-, Z\}$. The most general extension of the SM Lagrangian can be written as

$$\begin{aligned} \mathcal{L}_{\text{EW}} = &-\frac{1}{2}\operatorname{tr} W_{\mu\nu}W^{\mu\nu} - \frac{1}{4}B_{\mu\nu}B^{\mu\nu} + \sum_{f\in\{\ell_L,\ell_R\}} i\bar{f}^i \not{D} f^i \\ &+ \mathcal{L}_{UH} + \mathcal{L}_{\text{gauge-fix}} \quad . \end{aligned} \tag{211}$$

The Higgs and Goldstone sector is given by

$$\begin{aligned} \mathcal{L}_{UH} = &\frac{v^2}{4}\operatorname{tr}[D_\mu U^\dagger D^\mu U]F_U(H) + \frac{1}{2}\partial_\mu H\partial^\mu H - V(H) \\ &- \frac{v}{2\sqrt{2}}\left[\bar{\ell}_L^i \tilde{Y}_\ell^{ij}(H)U(1-\tau_3)\ell_R^j + \text{h.c.}\right] \quad , \end{aligned} \tag{212}$$

where we defined the right-handed doublets as $\ell_R^i = (\nu_R^i, e_R^i)^T$, and i, j are the lepton-flavor indices. In the SM, the functions $F_U(H)$, $V(H)$ and $Y_e^{ij}(H)$ are simple polynomials in H/v that can be generalized to

$$F_U(H) = 1 + \sum_{n\geq 1} f_{U,n} \left(\frac{H}{v}\right)^n , \tag{213}$$

$$V(H) = v^4 \sum_{n\geq 2} f_{V,n} \left(\frac{H}{v}\right)^n \qquad \text{and} \tag{214}$$

$$\tilde{Y}_\ell^{ij}(H) = \sum_{n\geq 0} \tilde{Y}_{\ell,n}^{ij} \left(\frac{H}{v}\right)^n . \tag{215}$$

We do not assume CP violation in this sector, hence the coefficient of these different series are real, $\tilde{f}_{U,n}, f_{V,n}, \tilde{Y}_{\ell,n}^{ij} \in \mathbb{R}$. They are general parameters that can be obtained by a matching procedure from a possible underlying physical model, and in principle can be measured in appropriate physical processes.

We are primarily interested in the Higgs-lepton couplings. So we read off the mass matrix for the leptons

$$\tilde{M}_\ell^{ij} = \frac{v}{\sqrt{2}} \tilde{Y}_{\ell,0}^{ij} \quad , \tag{216}$$

which is non-diagonal in general. As its eigenvalues are assumed to be positive, we can perform the usual polar decomposition $\tilde{M}_\ell = U_L M_\ell U_R^\dagger$ with some unitary matrices $U_{L/R}$ and compensate this by the rotation to the physical fields $\ell_L \mapsto U_L \ell_L$ and $\ell_R \mapsto U_R \ell_R$. Furthermore this defines $Y_{\ell,n} = U_L^\dagger \tilde{Y}_{\ell,n} U_R$, where, again, $n+1$ is the number of Higgs fields involved in the corresponding vertex. We will focus on the physical basis from now on. Note, that these equations all are still matrix equations, with the (2,2)-components $Y_{\ell,0}^{2,2} := y_\mu$, $Y_{\ell,n}^{2,2} := y_n$ and $M_\ell^{2,2} := m_\mu$ denoting the muon. Selecting the muon term and requiring the physical muon mass to equal its observed value, we observe an effective correction of the observable Yukawa coupling by the factor

$$\kappa_\mu = \frac{v}{\sqrt{2} m_\mu} y_1, \tag{217}$$

which, for $y_1 = y_0 = y_\mu$, would correspond to the SM case $\kappa_\mu = 1$. A priori, the size of the coupling coefficients is unknown as it depends on the underlying dynamics. From the "naive dimensional analysis" [130, 131], one would expect the modification as $y_n \sim y_\mu(g^2/16\pi^2)^n$, with $g \sim 1$ for a weakly coupled theory and $g \sim \mathcal{O}(4\pi)$ a strongly coupled theory.

New operators in the series expansion in H/v introduce contact terms which couple the muon to n Higgs or Goldstone bosons. These contact terms are proportional to y_m, where $m \leq n$ denotes the number of Higgs bosons and they are the leading contributions to $\mu^+\mu^- \to n\varphi$ scattering in the high energy limit. Hence, via the GBET, a modification of y_μ is generically accompanied by new large contributions to multi-boson production in the high-energy limit.

4.1.2.2 The Yukawa interaction in the SMEFT parameterization

In the SMEFT framework, the SM gauge invariance is represented in linear form, and the Higgs boson combines with the Goldstone bosons as a complex $SU(2)$ doublet. The pure effect of a modified muon Yukawa coupling can be reproduced by an infinite series of higher-dimensional operators in the SMEFT Lagrangian [132, 133, 134, 135], where all coefficients are related to the original coupling modification. The results will be again identical to the unitary-gauge calculation.

However, if we furthermore assume a *decoupling* property of the new interactions, *i.e.*, their parameters are not intrinsically tied to the electroweak scale, we should expect higher-order terms in the SMEFT series to be suppressed by a new heavy physics scale v^2/Λ^2, such that truncation after the first term is permissible. In that case, we have to discard the former relation between all orders, and accept that the resulting amplitudes will differ from the unitary-gauge results for an anomalous Yukawa coupling. In concrete terms, in a decoupling new-physics scenario we expect anomalous production of multiple vector bosons to be accompanied by anomalous production of multiple Higgs bosons. The clean environment of a muon collider is optimally suited to separate such final states irrespective of their decay modes, and thus to guide model building in either direction, depending on the pattern actually observed in data. The formalism set up here is very similar to the one used in [136] for searching deviations in the charm and strange Yukawa couplings in multi-boson production at the LHC and FCC-hh.

In the linear representation of the Higgs doublet,

$$\varphi = \frac{1}{\sqrt{2}} \begin{pmatrix} \sqrt{2}\phi^+ \\ v + H + i\phi^0 \end{pmatrix} \quad , \tag{218}$$

the most general bottom-up extension of the SM Lagrangian,

$$\begin{aligned} \mathcal{L}_{\text{EW}} = &-\frac{1}{2}\operatorname{tr} W_{\mu\nu}W^{\mu\nu} - \frac{1}{4}B_{\mu\nu}B^{\mu\nu} + (D_\mu\varphi)^\dagger(D^\mu\varphi) + \mu^2\varphi^\dagger\varphi - \frac{\lambda}{2}(\varphi^\dagger\varphi)^2 \\ &+ \sum_{f\in\{\ell_L,e_R\}} i\bar{f}^i \not{D} f^i - \left(\bar{\ell}^i_L \tilde{Y}^{ij}_\ell \varphi e^j_R + \text{h.c.}\right) + \mathcal{L}_{\text{gauge-fix}} \end{aligned} \tag{219}$$

that leads to a modification of the Yukawa coupling, reads

$$\mathcal{L} = \mathcal{L}_{\text{EW}} + \left[\sum_{n=1}^{N} \frac{\tilde{C}^{(n)ij}_{\ell\varphi}}{\Lambda^{2n}} (\varphi^\dagger\varphi)^n \bar{\ell}^i_L \varphi e^j{}_R + \text{h.c.}\right] \quad . \tag{220}$$

Operators of higher mass dimension are as usual suppressed by a large scale Λ that can be understood as an energy cutoff for the validity of the theory, as it will lead to an expansion of the scattering matrix elements in $\sqrt{s}/\Lambda$. Again, we do not consider CP violation, hence the Wilson coefficients are real $\tilde{C}^{(n)}_{\ell\varphi} \in \mathbb{R}$. They can be obtained by a matching procedure from an underlying physical model, and in principle can be measured.[2] For further calculations, we absorb the large scale $1/\Lambda^2$ in the Wilson coefficients.

We can read off the (non-diagonal) mass matrix for the charged leptons

$$\tilde{M}^{ij}_\ell = \frac{v}{\sqrt{2}} \left(\tilde{Y}^{ij}_\ell - \sum_{n=1}^{N} \tilde{C}^{(n)ij}_{\ell\varphi} \frac{v^{2n}}{2^n}\right) \quad . \tag{221}$$

In the same way as for the non-linear representation, we can diagonalize the mass matrix by redefinitions of the physical fields $e_L \mapsto U_L e_L$, $e_R \mapsto U_R e_R$. This defines $Y_\ell = U_L^\dagger \tilde{Y}_\ell U_R$ and $C^{(n)}_{\ell\varphi} = U_L^\dagger \tilde{C}^{(n)}_{\ell\varphi} U_R$.

As already discussed for the non-linear case, the operator coefficients $C^{(n)}_{\ell\varphi}$ can shift the muon Yukawa coupling away from its SM value. Because of its intrinsically small value, a moderate new physics contribution could lead to a drastic effect, driving it to zero or reversing its sign. The extreme case of a vanishing muon Yukawa coupling has the significant consequence that multi-Higgs production, $\mu^+\mu^- \to H^M$ would be absent at tree level, while

---

[2] One rather measures form factors, which are linear combinations of the Wilson coefficients.

production of up to $k \in \{1, \ldots, M-1\}$ Higgs bosons associated with $M-k$ vector bosons would be allowed. As a paradigm example, we show how to embed this in our SMEFT framework: we require all lepton couplings to k Higgs bosons, $\Lambda_{(k)}$, $k \in \{1, \ldots, M-1\}$, to vanish while the mass of the measured muon mass m_μ is fixed as an input. This leads to the conditions

$$M_\ell = \frac{v}{\sqrt{2}} \left[Y_\ell - \sum_{n=1}^{M-1} C_{\ell\varphi}^{(n)} \frac{v^{2n}}{2^n} \right] \quad , \tag{222}$$

$$\Lambda_{(k)} := -i \frac{k!}{\sqrt{2}} \left[Y_\ell \delta_{k,1} - \sum_{n=n_k}^{M-1} C_{\ell\varphi}^{(n)} \begin{pmatrix} 2n+1 \\ k \end{pmatrix} \frac{v^{2n+1-k}}{2^n} \right] = 0 \quad , \tag{223}$$

where $n_k = \max(1, \lceil \frac{k-1}{2} \rceil)$.

For the general case, we define the following modification of the SM Yukawa coupling, still matrix-valued in flavor space, as

$$K_\ell = 1 - \frac{v}{\sqrt{2}} M_\ell^{-1} \sum_{n=1}^{M-1} C_{\ell\varphi}^{(n)} \frac{n v^{2n}}{2^{n-1}} \quad . \tag{224}$$

Again, we can project to the muon via $Y_\ell^{2,2} := y_\mu$, $C_{\ell\varphi}^{(n)2,2} := c_{\ell\varphi}^{(n)}, M_\ell^{2,2} := m_\mu$, as well as $K_\ell^{2,2} := \kappa_\mu$.

As usual, we will consider the linear SMEFT expansion up to the first non-trivial order, which adds to the dimension-4 SM Yukawa coupling operator, $\mathcal{L}_{\text{Yuk.}} = -(\bar{\ell}_L Y_\ell e_R)\varphi$ at dimension-6 a single operator that modifies the static Higgs coupling to leptons:

$$\mathcal{O}_{\ell\varphi} = C_{\ell\varphi} (\varphi^\dagger \varphi)(\bar{\ell}_L e_R)\varphi \; . \tag{225}$$

Here, both Γ_ℓ as well as $C_{\ell\varphi}$ are matrices in lepton-flavor space. On dimensional grounds, $C_{\ell\varphi} \sim 1/\Lambda^2$, where Λ is the scale at which new physics sets in. Inserting the Higgs vev, we obtain at dimension-4 the SM value of the lepton mass matrix, $M_\ell^{(4)} = \frac{v}{\sqrt{2}} Y_\ell$, while at dimension-6 we get a modified mass matrix

$$M_\ell^{(6)} = \frac{v}{\sqrt{2}} \left(Y_\ell - \frac{v^2}{2} C_{\ell\varphi} \right) . \tag{226}$$

Specializing to the muon term and requiring the physical muon mass to equal its measured value, we observe an effective modification of the observable Yukawa coupling by the factor

$$\kappa_\mu^{(6)} = 1 - \frac{v^3}{\sqrt{2}\, m_\mu} c_{\ell\varphi}^{(1)}. \tag{227}$$

Expanding the Higgs field, the new operator induces contact terms which couple the muon to $n = 1, 2$, or 3 Higgs or Goldstone bosons. The contact terms are all proportional to the operator coefficient $c_{\ell\varphi}^{(1)}$, either scalar or pseudoscalar. Squaring this interaction, we obtain local contributions to $\mu^+\mu^- \to n\varphi$ scattering, in analogy with the HEFT description. The physical final states are Higgs or longitudinal W, Z gauge bosons. The $d = 6$ contributions to their production cross sections with multiplicity $n = 3$ rise with energy, $\sigma \propto s$, while the SM contribution falls off like $1/s$. There is no interference, since – for these final states – the SM requires a vector exchange while the new contact term is scalar. We obtain a deviation from the SM prediction which is determined by the EFT contribution alone, which becomes leading above some threshold which depends on $\kappa_\mu^{(6)} - 1$. The decomposition of the anomalous contribution into particle types (WWZ, WWh, etc.) is fixed by electroweak symmetry and the particular SMEFT operator content, such that the exclusive channels are related by simple rational factors beyond the threshold where the new-physics part starts to dominate the production rates.

If the correction was large enough to render $\kappa_\mu = 0$, we would obtain the unitarity bound for $d = 6$, *i.e.* three-boson emission, as discussed in the next subsection. Generally speaking, the modification from the SM Yukawa coupling could reach an order of 100% if $c_{\ell\varphi}^{(1)} \sim 0.1/(10v)^2$. We emphasize that these two sample scenarios – a pure modified Yukawa coupling, and a modified Yukawa coupling combined with truncation of the SMEFT series – are to be understood as mere representatives of a potential new class of SM modifications that are difficult to observe at lower energy. As our results indicate, there is a great redundancy in the analysis of exclusive multi-boson final states, which should translate into significant discrimination power regarding more detailed models of the Higgs-Yukawa sector beyond the SM. If we translate an experimental bound on $\Delta\kappa_\mu$ to the SMEFT coefficient $c^{(1)} \sim g/\Lambda^2$, we obtain a bound on the scale of new physics as

$$\Lambda > 10 \text{ TeV} \sqrt{\frac{g}{\Delta\kappa_\mu}} \quad . \tag{228}$$

4.1.2.3 Unitarity bounds on a nonstandard Yukawa sector

In the SM, the high-energy asymptotics of the multi-boson production cross sections universally fall off with rising energy, manifesting themselves in delicate gauge cancellations which become huge at high energies. A modification of the muon Yukawa coupling from the SM prediction would show up as spoiling such cancellations, and thus eventually causes specific scattering amplitudes to rise again, without limits. While in theory, such a unitary-gauge framework does not do justice to the built-in symmetries of the SM, it is nevertheless the baseline framework for any tree-level evaluations such as the ones that we use in this work.

In Ref. [137], generic models have been investigated where the leading contribution to a fermion mass originates from a dimension-d EFT operator that couples the fermion to the SM Higgs field. Using the GBET, they computed the energy scale Λ_d where unitarity is violated by multiple emission of Goldstone bosons, representing longitudinally polarized weak vector bosons, and Higgses.

$$\Lambda_d = 4\pi\kappa_d \left(\frac{v^{d-3}}{m_f}\right)^{1/(d-4)}, \quad \text{where} \quad \kappa_d = \left(\frac{(d-5)!}{2^{d-5}(d-3)}\right)^{1/(2(d-4))}. \tag{229}$$

For any given $d > 4$, the most relevant bound corresponds to a final state that consists of $n = d - 3$ Goldstone or Higgs bosons in total. For $m_f = m_\mu$ and $d = 6, 8, 10$, the numeric values of the unitarity bound are 95 TeV, 17 TeV, and 11 TeV, respectively. For $d \geq 8$, the values of these bounds lie within the energy range that is accessible at a future muon collider. They imply large amounts of observable multi-boson production. The strong suppression of the corresponding SM processes enables a study already significantly below those upper bounds. Furthermore, we expect observable effects even if only a fraction of the muon mass is due to the new-physics contributions that are parameterized by those operators.

In the previous subsection, we have discussed an analogous sequence of phenomenological scenarios within the SMEFT framework, where we require that local Higgs-fermion couplings are absent up to a given Higgs multiplicity n. This requirement enforces a specific choice of the SMEFT operator coefficients $C_{\ell\varphi}^{(n)}$ up to dimension $d = 2n + 4$, as defined by Eq. (222). The limit $d \to \infty$ corresponds to the case of no local Higgs-fermion couplings of any multiplicity. We emphasize that this peculiar choice is merely an extreme case of a generic anomalous muon Yukawa sector. The generic case is parameterized within the SMEFT or HEFT formalisms, allowing the coefficients of the higher-dimensional couplings to vary freely within the constraints imposed by unitarity.

In quantitative terms, the unitarity constraint for the total inelastic cross section $\sigma_{\mu^+\mu^-\to X}$, where $X \neq \mu^+\mu^-$, is given by the inequality

$$\sum_X \sigma_{\mu^+\mu^-\to X}(s) \leq \frac{4\pi}{s}. \tag{230}$$

In Fig. 15 we display the total cross section for this sequence of scenarios, including operators up to dimension $d = 6, 8, 10, \ldots$ and compare it with the upper bound in Eq. (230). The cross section has been evaluated using the GBET, summing over all final states. The SM contribution ($d = 4$) can be neglected for this purpose, and the boson masses are set to zero. The multiplicity of the Higgs and Goldstone bosons extends up to $n = d-3$, which evaluates to $n = 3, 5, 7, \ldots$, respectively.

We observe that for $d \leq 10$ (i.e., $n \leq 7$), the sum over cross sections does not touch the unitarity bound before 15 TeV, while for higher dimension and multiplicity, the curves cross already at collider energies within the range considered for a muon collider. In the $d \to \infty$ case, the multiplicity of extra Goldstone-boson production becomes unbounded, and the unitarity limit for the sequence of scenarios in Eq. (222) formally drops towards the original electroweak scale [137]. Even if we account for finite vector-boson masses, such a scenario should be qualified as strongly interacting, and finite-order predictions in the multi-TeV range become invalid. Of course, we do not expect the actual operator coefficients to strictly follow such a pattern, so the argument should rather be understood as a guideline regarding the inherent limitations of the EFT in the current context.

For this reason, we consider lower-dimensional operators in the SMEFT or HEFT expansions individually. The presence of extra Higgs bosons in the gauge-invariant SMEFT operators of fixed dimension delays the potential onset of new (strong) interactions to higher energy. While in the tables and plots of the subsequent sections we will frequently refer to the $d = \infty$ limit for illustration, in our phenomenological study we work with Higgs–Goldstone multiplicities $n \leq 4$ and limit the dimensions of the included SMEFT operators

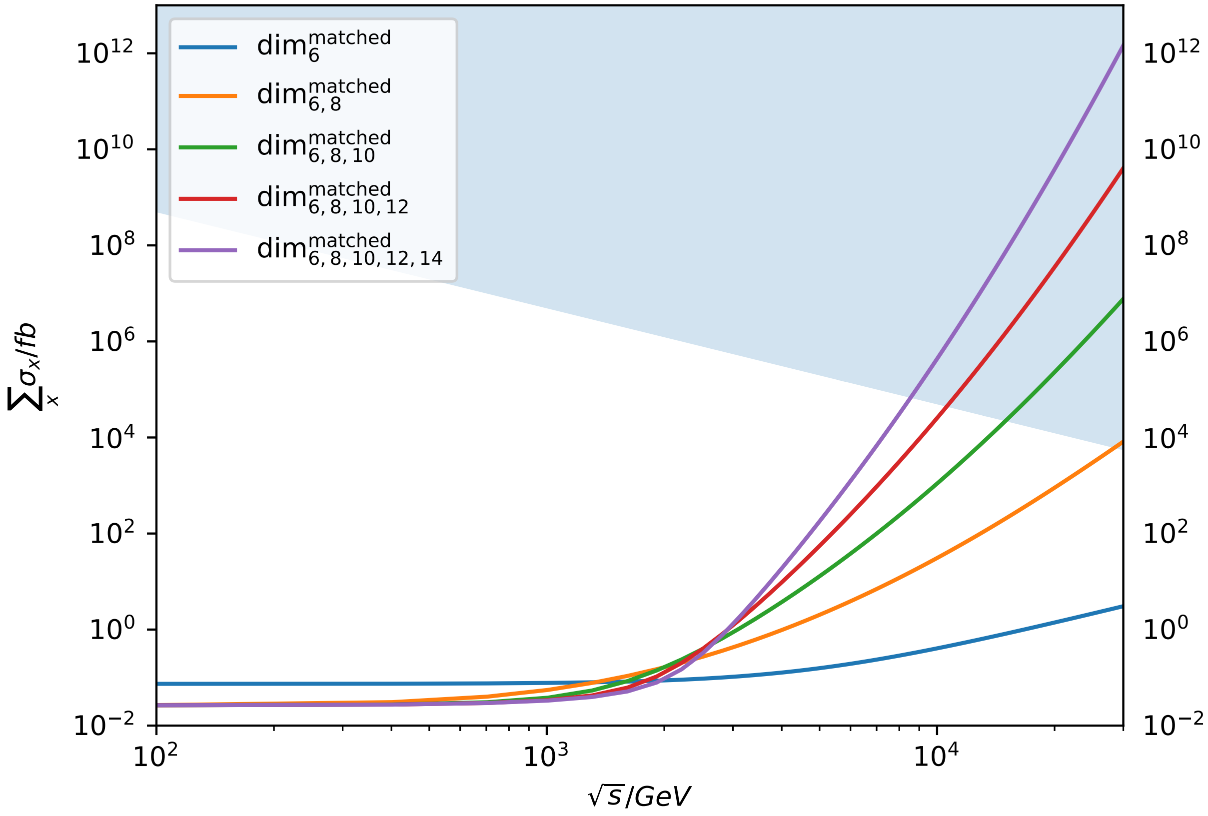

Figure 15: Inclusive inelastic cross section $\mu^+\mu^- \to X$ for multiple Goldstone and Higgs-boson production in the GBET approximation. We show the result for the sequence of SMEFT scenarios defined by the conditions in Eq. (222), truncated at dimension $d = 6, 8, 10, 12, 14$, respectively. The maximal multiplicity of the final state is $n = 3, 5, 7, 9, 11$, respectively. The shaded area indicates the region that is excluded by the universal unitarity bound for the inclusive cross section in Eq. (230).

to $d = 6, 8, 10$. For those final states, Fig. 15 indicates that unitarity is not yet relevant at a muon collider as proposed, even if we adopt one of the extreme scenarios described above. Clearly, higher multiplicities may yield even stronger effects, but their contributions depend on further coefficients in the EFT expansion and should therefore be regarded as model-dependent. In fact, if in Eq. (230) we restrict the sum over final states to $n \leq 4$, there is no problem with unitarity for any of the parameter sets shown in Fig. 15. The numerical results of our study below will rely on the lowest multiplicities and analyze small deviations from the SM where the actual effect is at the limit of the collider sensitivity, orders of magnitude below the unitarity bound.

4.1.3 Phenomenology of Muon-Higgs Coupling at a high-energy Muon Collider

In this section, we explore the phenomenology of multi-boson production for the sensitivity to the muon Yukawa coupling at a muon collider with collision energy in the range $1 < \sqrt{s} < 30$ TeV, with an integrated luminosity, which scales with energy quadratically as [68, 106],

$$\mathcal{L} = \left(\frac{\sqrt{s}}{10 \text{ TeV}}\right)^2 10 \text{ ab}^{-1}. \qquad (231)$$

4.1.3.1 Multi-boson production

To numerically determine the different multi-boson production cross sections and later on assess the sensitivity to the muon Yukawa coupling, we parameterize the EFT contributions discussed in the last section with a model-independent coupling κ_μ, *e.g.*, Eq. (217) or Eq. (227), and implement it into the multi-purpose event generator WHIZARD 2.8.5 [64, 138, 139] using its plugin to external models [140]. This is building upon the EFT frameworks used for multi-boson production and vector-boson scattering at hadron [141, 142, 143, 144] and electron-positron colliders [145, 146], which we adapted here for the muon collider. The QED initial-state radiation (ISR), resummed to all orders in soft photons and up to third order in hard-collinear radiation, is equally applicable to the muon collider. Beam spectra for multi-TeV muon colliders are much less complicated than for electron-positron colliders

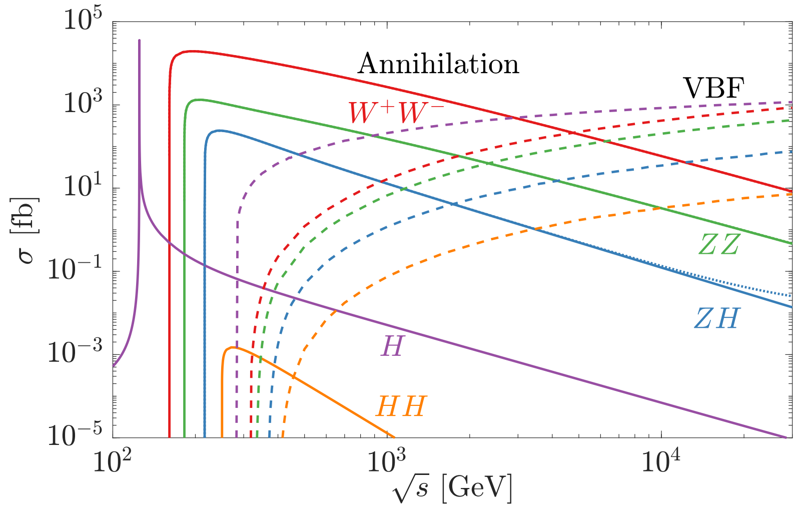

Figure 16: The cross sections of diboson production at a $\mu^+\mu^-$ collider as a function of the c.m. energy $\sqrt{s}$. The solid and dotted lines are for the direct annihilation with muon Yukawa coupling as $\kappa_\mu = 1$ and $\kappa_\mu = 0$ (2) (hardly visible), respectively. The dashed rising curves are the (charged) vector boson fusions (VBF), $\mu^+\mu^- \to \nu_\mu \bar{\nu}_\mu X$, calculated using the fixed-order (FO) approach with a cut on the invariant mass of $\nu_\mu \bar{\nu}_\mu$ pair $M_{\nu_\mu \bar{\nu}_\mu} > 150\,\text{GeV}$. All calculations are carried out with WHIZARD 2.8.5.

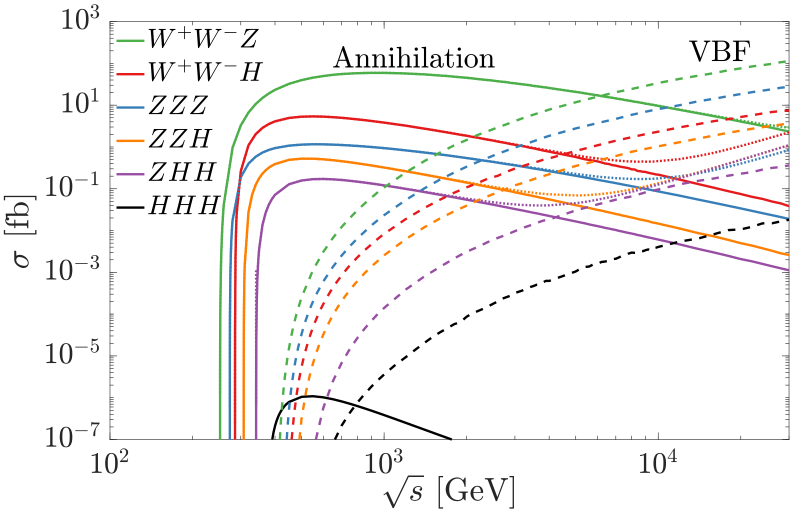

Figure 17: Similar to Fig. 16, the cross sections of three-boson production at a $\mu^+\mu^-$ collider as a function of the c.m. energy $\sqrt{s}$.

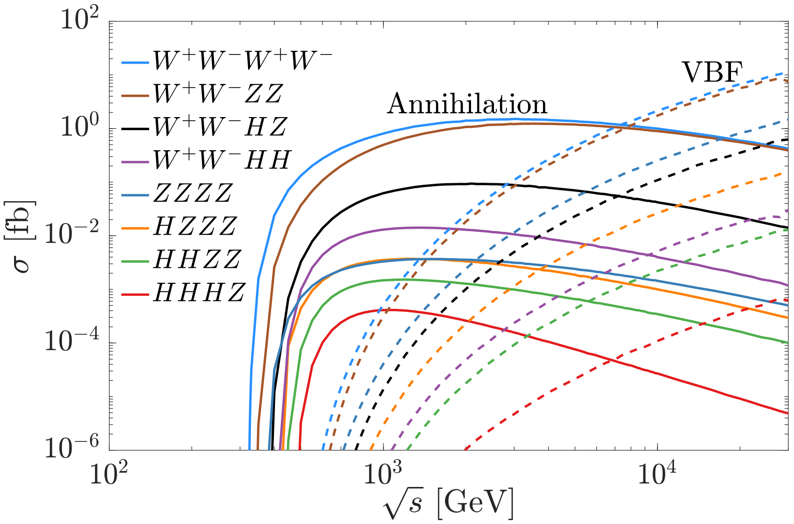

Figure 18: Similar to Fig. 16, the cross sections of four-boson production at a $\mu^+\mu^-$ collider as a function of the c.m. energy $\sqrt{s}$, for SM $\kappa_\mu = 1$ only.

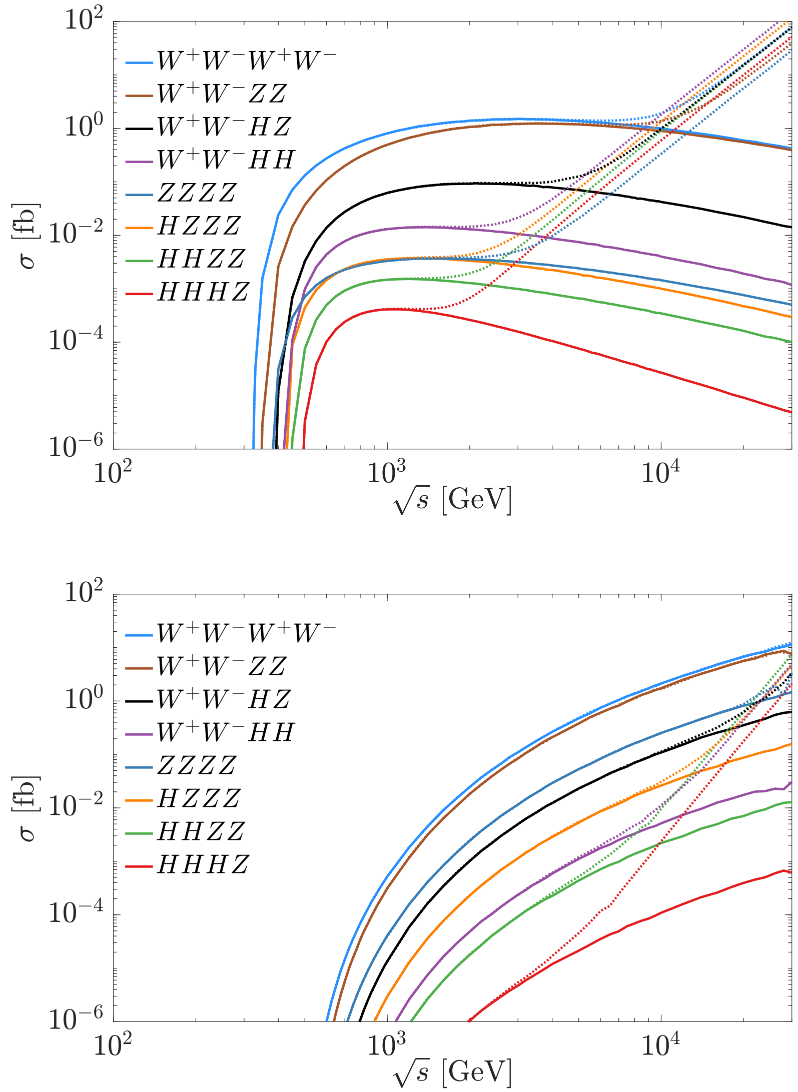

Figure 19: The cross sections of four-boson production at a $\mu^+\mu^-$ collider via (a) annihilation $\mu^+\mu^- \to 4B$ and (b) the (charged) vector boson fusions (VBF), $\mu^+\mu^- \to \nu_\mu\bar{\nu}_\mu X$ as functions of the c.m. energy $\sqrt{s}$. The solid and dotted lines are for the results with muon Yukawa coupling as $\kappa_\mu = 1$ and $\kappa_\mu = 0$ (2), respectively.

and can be easily described with a Gaussian beam spread of 0.1%. They are, however, not relevant at the level of this study.

In Figs. 16, 17 and 18, we first present the Standard Model (with $m_\mu = y_\mu v/\sqrt{2}$) cross sections for the production of two, three and four bosons, respectively, including the Higgs and the EW gauge bosons. The cross sections – in each case decreasing in size – are for two-boson production,

$$WW,\ ZZ,\ ZH,\ HH \tag{232}$$

for three-boson production,

$$WWZ,\ WWH,\ ZZZ,\ ZZH,\ ZHH,\ HHH \tag{233}$$

and for four-boson production,

$$WWWW,\ WWZZ,\ WWHZ,\ WWHH,\ ZZZZ,\ HZZZ,\ HHZZ,\ HHHZ \tag{234}$$

respectively. The single Higgs (H) production is also illustrated in Fig. 16, which are obtained through $\mu^+\mu^- \to H$ recoiled by ISR. We present two classes of production mechanisms, namely, the direct $\mu^+\mu^-$ annihilation and the vector boson fusion (VBF) resulting from the initial-state radiation off the muon beams[3]. Representative Feynman diagrams for these production mechanisms are shown in Fig. 20 for the W^+W^-H final state. Near the threshold, the annihilation cross sections dominate. With the increase of collision energy, they are suppressed by $1/s$. The VBF mechanisms, on the other hand, increase with energy logarithmically [60, 6] and eventually take over above a few TeV. The $\mu^+\mu^-$ annihilation to multiple Higgs bosons is induced by the Yukawa and possible Higgs self interactions, while no gauge couplings. The corresponding cross sections are highly suppressed compared with the channels involving gauge boson(s), with examples of HH and HHH demonstrated in Fig. 16 and 17. Therefore, there is no need to include four-Higgs production in Eq. (234)

---

[3] If no specific indication, we only include the charged vector boson ($W^\pm$) in VBF, *i.e.*, $W^+W^- \to X$. The Z boson fusion, $ZZ \to X$, is sub-leading due to its smaller vector coupling to leptons, with the example of ZHH production demonstrated in Table 7. The final states involving charged particles, *e.g.*, W^+W^-H, can be produced through photon or photon-Z fusion as well, which are mostly collinear to the initial beams. This background is largely excluded when a reasonable angular cut (*e.g.*, $10^\circ < \theta < 170^\circ$) is imposed, also illustrated in Table 7.

or Fig. 19, and the corresponding phenomenological study of the pure Higgs production is largely left for the future.

In the presence of anomalous couplings, the characteristic high-energy behavior shown in these figures is modified, as we discussed above in Sec. 4.1.2. At asymptotically high energy, for each final state the new-physics contribution dominates over the SM and exhibits a simple and uniform power law as shown in Figs. 16, 17 and 19 by the dotted curves, which behave as straight lines in double-logarithmic plots.

In Sec. 4.1.2 we provided a description within the EFT framework, in which the muon Yukawa coupling can receive contributions from new physics beyond the SM. Given real data, measuring those ratios at various energy values will allow us to deduce the underlying pattern. In particular, the absence of pure multi-Higgs states is a special feature for the extreme scenario $d \to \infty$ which we used for the plots in Fig. 17 and 19, *i.e.*, there are no direct muon-Higgs couplings at any order. In a more generic scenario, multi-Higgs states will appear with a sizable rate, and the observable ratios of vector-boson and Higgs final states are related to the operator structure in the SMEFT expansion.

We now discuss the phenomenology of a modified muon Yukawa coupling in more detail. In the effective approach discussed above, the muon Yukawa coupling gets a modification like Eq. (217) or Eq. (227). In such a way, $\kappa_\mu = 1$ corresponds to the SM case. The deviation of κ_μ from 1 quantifies the new physics contribution, which serves as the signal in this work. In Figs. 17-19, we showed two such benchmark cross sections for $\kappa_\mu = 0$ and 2 as dotted curves. They coincide with each other, which reflects a symmetry of the annihilation cross sections such that

$$\sigma|_{\kappa_\mu=1+\delta} = \sigma|_{\kappa_\mu=1-\delta}, \tag{235}$$

where δ is the deviation from the SM muon Yukawa prediction, with an exception for the pure Higgs production.

With $\kappa_\mu = 0$ (2) at a high energy, the annihilation cross sections of the ZZH and ZHH channels merge in Fig. 17(a), which is a result of the Goldstone equivalence between the longitudinal Z boson and the Higgs. A similar situation happens to the four-boson case at a higher collision energy in Fig. 19(b). When compared with the Standard Model annihilation, we find that the $\kappa_\mu = 0$ (2) cross sections agree at low collision energies, but gradually diverge

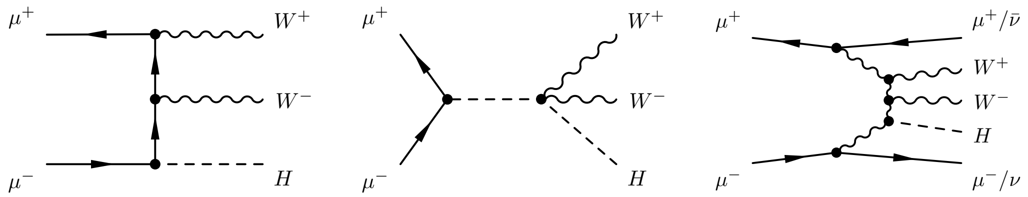

Figure 20: Representative diagrams for the signal annihilation process $\mu^+\mu^- \to W^+W^-H$ (left and middle), and for the VBF background process (right).

as the collision energy increases. At $\sqrt{s} = 30$ TeV, the relative cross section deviation can be three orders of magnitude for the ZHH case, while it amounts to 20% for WWZ case. This big difference provides us a good opportunity to test the muon Yukawa coupling at a multi-TeV $\mu^+\mu^-$ collider.

As discussed above, and pointed out in [6, 60], the annihilation process, in our particular case here for three-boson production, is overcome at high energies by the vector-boson fusion (VBF) production which becomes dominant at all high-energy (lepton) colliders. Here we show the VBF cross sections as dashed lines in Fig. 17, as well. They are calculated with the fixed-order approach for fusion processes $\mu^+\mu^- \to \nu_\mu \bar{\nu}_\mu X$, where X represents the desired final-state particles. We have imposed a cut on the invisible neutrinos, $M_{\nu_\mu \bar{\nu}_\mu} > 150$ GeV [147, 148], to suppress the on-shell decay $Z \to \nu_\mu \bar{\nu}_\mu$. We see that at an energy as high as 30 TeV, the VBF cross sections are generally $2 \sim 3$ magnitudes larger than the annihilation processes for three-boson production. The relative size is even larger for the four-boson case. These channels will serve as backgrounds for the annihilation multi-boson productions when we measure the muon Yukawa coupling.

4.1.3.2 Kinematic distributions

As we know, the kinematic distributions for the annihilation and VBF processes behave very differently. We take the WWH and ZHH production at a $\sqrt{s} = 10$ TeV $\mu^+\mu^-$ collider

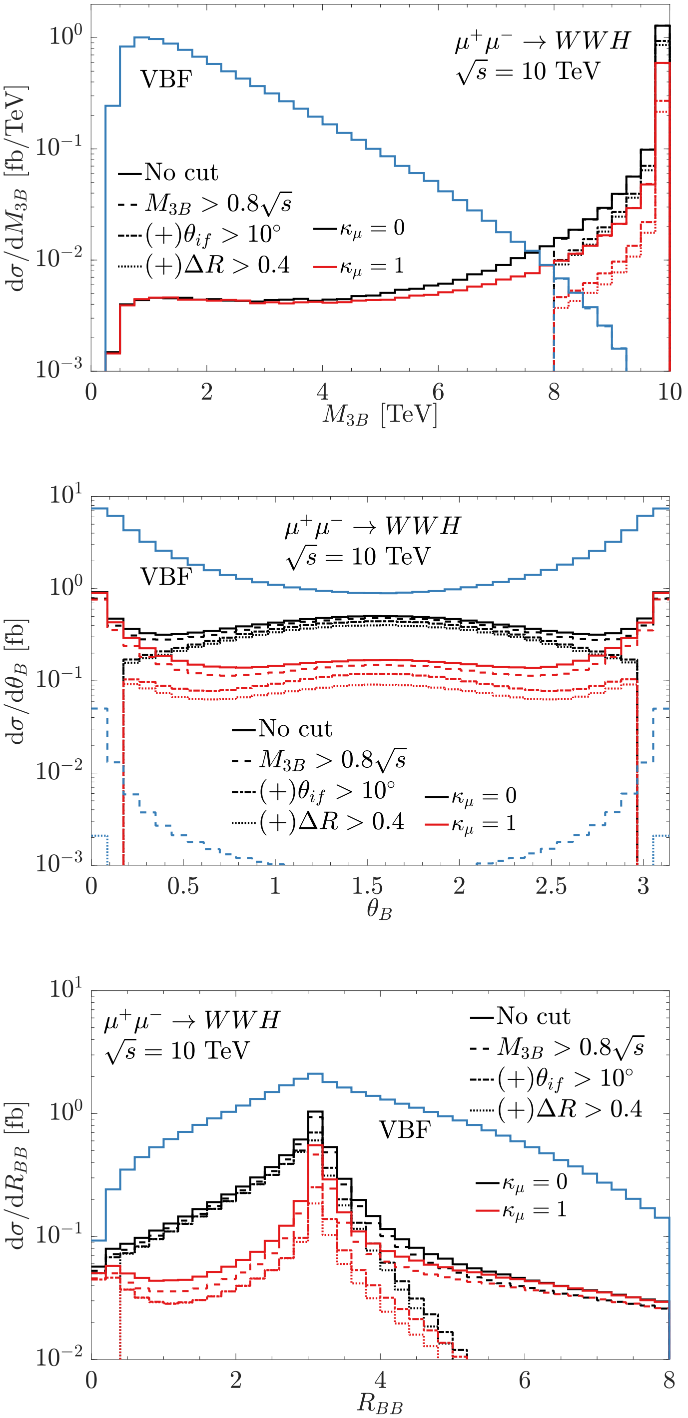

Figure 21: The kinematic distributions of the boson angle θ_B, the diboson distance R_{BB}, and the triboson invariant mass M_{3B} ($B = W, H$), respectively, in the WWH production at a $\sqrt{s} = 10$ TeV $\mu^+\mu^-$ collider.

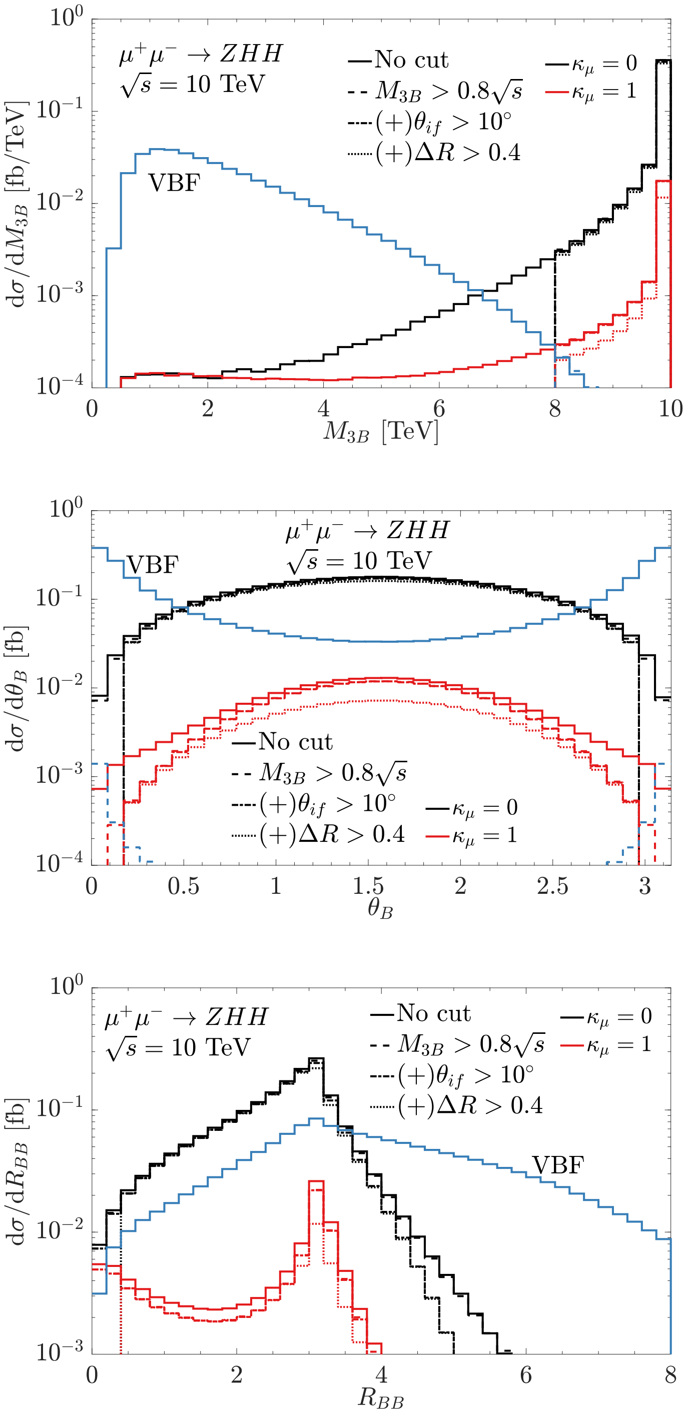

Figure 22: The kinematic distributions for θ_B, R_{BB}, and M_{3B} as in Fig. 21, but for ZHH production at a $\sqrt{s} = 10$ TeV $\mu^+\mu^-$ collider.

as benchmark examples[4] and show the distributions of boson angles θ_B ($B = W, Z, H$), the diboson separation distances $R_{BB} = \sqrt{(\Delta\eta)^2 + (\Delta\phi)^2}$ in the rapidity-azimuthal angle plane, and triboson invariant masses M_{3B}, respectively, in Fig. 21 and 22. We see two main differences. First, the invariant mass M_{3B} for the annihilation process is sharply peaked at the collision energy $\sqrt{s}$ seen in Fig. 21(a) and 22(a), with a small spread due to the initial-state radiation (ISR). In contrast, in vector-boson fusion, the M_{3B} is mainly peaked around the threshold. This feature enables us to efficiently separate these two processes and reduce the VBF background with an invariant mass cut. More specifically, with the $M_{3B} > 0.8\sqrt{s}$ cut, the VBF background is reduced by three orders of magnitudes, with the absolute differential cross sections falling below the lower axis limits in Figs. 21 and 22. In comparison, the signal, $\kappa_\mu = 0$ (2), almost remains the same size, with specific numbers listed in Table 7. We also include the cut flow for the cross sections of SM annihilation to WWH and ZHH without including the ISR effect in Table 7. We see the invariant mass cut does not impact at all in this case, because the $M_{3B} = \sqrt{s}$ is exact as a result of the momentum conservation. Another important observation is that the invariant mass cut $M_{3B} > 0.8\sqrt{s}$ together with the ISR effect gives roughly the same cross sections without ISR, which justifies neglecting the ISR effect when necessary.

Second, the final-state particles produced in the vector boson fusion are very forward, shown in Fig. 21(b) and 22(b). In comparison, the annihilation-produced particles are much more central, especially for the events induced by a Yukawa interaction with $\kappa_\mu = 0$ (2). With an angular cut, such as $10° < \theta_B < 170°$ based on the detector design [106], we are able to reduce the VBF background by more than another factor of 10. The SM annihilation cross section will be suppressed by a factor of 2 for WWH, while the signal events with $\kappa_\mu = 0$ (2) are only reduced by 30%. As for the case of the ZHH processes, the impact of the angular cut is small both for the VBF background and for the annihilation process.

Finally, in order to reasonably resolve the final states within the detector, we need to require a basic separation among the reconstructed final-state bosons. The distributions of separation distance R_{BB} in the WWH and ZHH production are shown in Fig. 21(c) and

---

[4] In triboson production, we choose WWH as a demonstration example considering its large production rate, and ZHH as another one for its relatively large deviation from the anomalous coupling. The WWZ channel has an even larger cross section, while it suffers from a small relative deviation.

Cut flow	$\kappa_\mu = 1$	w/o ISR	$\kappa_\mu = 0$ (2)	CVBF	NVBF
σ [fb]	WWH				
No cut	0.24	0.21	0.47	2.3	7.2
$M_{3B} > 0.8\sqrt{s}$	0.20	0.21	0.42	$5.5 \cdot 10^{-3}$	$3.7 \cdot 10^{-2}$
$10° < \theta_B < 170°$	0.092	0.096	0.30	$2.5 \cdot 10^{-4}$	$2.7 \cdot 10^{-4}$
$\Delta R_{BB} > 0.4$	0.074	0.077	0.28	$2.1 \cdot 10^{-4}$	$2.4 \cdot 10^{-4}$
# of events	740	770	2800	2.1	2.4
S/B	2.8				
σ [fb]	ZHH				
No cut	$6.9 \cdot 10^{-3}$	$6.1 \cdot 10^{-3}$	0.119	$9.6 \cdot 10^{-2}$	$6.7 \cdot 10^{-4}$
$M_{3B} > 0.8\sqrt{s}$	$5.9 \cdot 10^{-3}$	$6.1 \cdot 10^{-3}$	0.115	$1.5 \cdot 10^{-4}$	$7.4 \cdot 10^{-6}$
$10° < \theta_B < 170°$	$5.7 \cdot 10^{-3}$	$6.0 \cdot 10^{-3}$	0.110	$8.8 \cdot 10^{-6}$	$7.5 \cdot 10^{-7}$
$\Delta R_{BB} > 0.4$	$3.8 \cdot 10^{-3}$	$4.0 \cdot 10^{-3}$	0.106	$8.0 \cdot 10^{-6}$	$5.6 \cdot 10^{-7}$
# of events	38	40	1060	–	–
S/B	27				

Table 7: The cut-flow for the cross sections of WWH and ZHH production through annihilation (SM with $\kappa_\mu = 1$) with and without ISR, and the BSM signal models for $\kappa_\mu = 0$ (2) (i.e., $\Delta\kappa_\mu = \pm 1$). The last two columns are the SM backgrounds from charged (CVBF) and neutral vector boson fusion (NVBF), respectively. All cross sections are at a $\sqrt{s} = 10$ TeV $\mu^+\mu^-$ collider. The event numbers correspond to an integrated luminosity $\mathcal{L} = 10$ ab^{-1}. The signal and background are defined in Eq. (236).

22(c). Besides the peak around $R_{BB} \sim \pi$ due to the back-to-back configuration, we obtain another minor peak around $R_{BB} \sim 0$ for the SM annihilations, which reflects the collinear splitting behaviors, such as $W \to WH$ or $Z \to ZH$. With a reasonable separation cut $R_{BB} > 0.4$, the SM annihilation to ZHH is reduced by roughly 30% due to the removal of radiation patterns with collinear splitting $Z \to ZH$. In comparison, both signal and backgrounds for WWH production are only reduced slightly, with specific numbers presented in Table 7. In this case, the collinear splitting coincides with the forward beam region, which is already cut away by the angular acceptance.

4.1.3.3 Statistical sensitivity on the Muon Yukawa Coupling

With the integrated luminosity in Eq. (231), we obtain the event numbers for annihilation and VBF for WWH and ZHH, listed in Table 7. We see a big visible deviation from the SM backgrounds ($\kappa_\mu = 1$) if we assume the muon Yukawa coupling varying within a range $\kappa_\mu = 0 \ldots 1 \ldots 2$. We can obtain the signal and background events as

$$S = N_{\kappa_\mu} - N_{\kappa_\mu=1},\ B = N_{\kappa_\mu=1} + N_{\text{VBF}}, \tag{236}$$

with a large signal-to-background ratio S/B for WWH and ZHH shown in Table 7. We can define the corresponding statistical sensitivity to the anomalous (non-SM) muon Yukawa coupling as

$$\mathcal{S} = \frac{S}{\sqrt{B}}. \tag{237}$$

We would like to emphasize that $\mathcal{S}$ is always positive due to $N_{\kappa_\mu} \geq N_{\kappa_\mu=1}$, so we can define it without a modulus. We would expect a big sensitivity under the assumption $\kappa_\mu = 0$ (2) for both WWH and ZHH channels, with the specific values even beyond the applicability of Gaussian approximation adopted in Eq. (237).

We want to know how precisely we can measure the muon Yukawa coupling at a high-energy muon collider. For this task, we perform a scan of the annihilation cross sections over the collision energy $\sqrt{s}$ and the effective coupling κ_μ, with results in the band of curves shown in Fig. 23. We do not include the WWZ channel as the corresponding sensitivity is small resulting from the relatively small deviation shown in Fig. 17. The ISR effect is safely

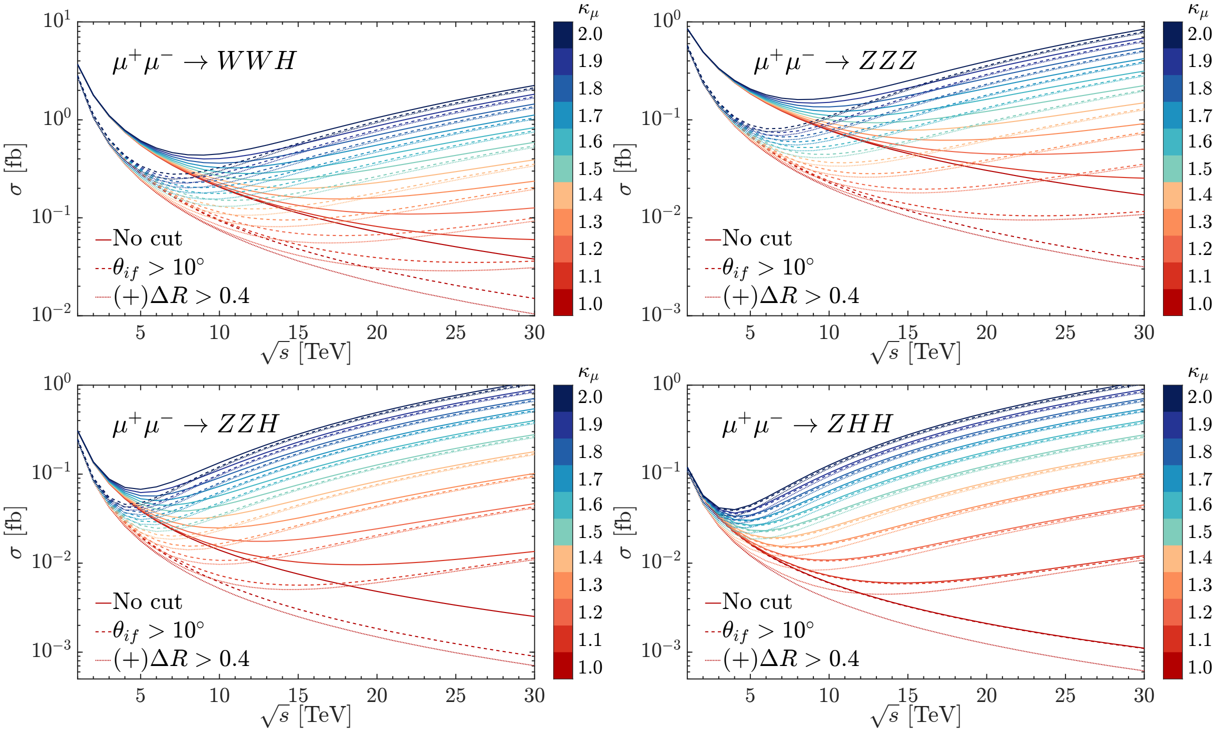

Figure 23: The cross sections of annihilation without ISR for the three-boson production channels $\mu^+\mu^- \to WWH, ZZZ, ZZH, ZHH$ versus the $\mu^+\mu^-$ c.m. energy $\sqrt{s}$ and the effective coupling κ_μ. The lower two clusters of curves correspond the flow cut: $\theta_{if} > 10^\circ$ and the accumulated $\Delta R > 0.4$.

discarded in this scan, thanks to the balance of the invariant mass cut, illustrated by the example of WWH and ZHH production in Table 7. In Fig. 23, we present three clusters of curves to illustrate the impact of the cut flow. The solid lines indicate the annihilation cross sections without any cuts. The lower clusters of dashed and dotted curves correspond to the angular cuts $10^\circ < \theta_B < 170^\circ$ and the accumulated $\Delta R_{BB} > 0.4$. We see that at large collision energy, the signal cross sections corresponding to $\kappa_\mu \neq 1$ are not hampered by the kinematic cuts compared to the SM annihilation ones ($\kappa_\mu = 1$). Especially at a large κ_μ deviation, such as $\kappa_\mu = 0(2)$, the cross sections with and without selection cuts are more or less the same. The angular cut almost has no impact on the ZHH channel, because both the Z and H boson are predominantly central in this channel, as mentioned above and shown in Fig. 22 (b). Instead, the separation distance cut reduces the SM annihilation rate by a factor of 30%∼40%, due to the removal of collinear splittings of $Z \to ZH$.

At this stage, we are able to obtain the sensitivity of a high-energy muon collider on the muon Yukawa coupling, by combining the cross sections with the corresponding integrated luminosity. In Fig. 24, we show two type of contours, corresponding to $\mathcal{S} = 2$ and 5 respectively, with an integrated luminosity as given in Eq. (231). We recall that the sensitivity respects a symmetry that $\mathcal{S}|_{\kappa_\mu=1+\delta} = \mathcal{S}|_{\kappa_\mu=1-\delta}$, due to the nature of the symmetric cross sections in Eq. (235). The channels – in decreasing size of sensitivity – are ZHH, ZZH, WWH, and ZZZ, respectively. At the low energy end, around 3 TeV, we are able to probe the muon Yukawa coupling about 100% by means of the ZHH channel, if we take the criterion $\mathcal{S} = 2$. At a 10 (30) TeV muon collider, we are able to test the muon Yukawa coupling to a precision of up to 10% (1%), mostly because of two factors: large signal-to-background ratios and large integrated luminosity. In addition, we see the sensitivity of the ZZH is very close to the ZHH channel, as a result of the Goldstone equivalence theorem. Again, in the SMEFT formalism, the anticipated precision of $10\% - 1\%$ would translate to the sensitivity of the scale as $\Lambda \sim 30 - 100$ TeV.

So far in this paper, we have focused on the sensitivity to the muon Yukawa coupling from triboson production measurements at a high-energy muon collider. Similar analyses can be performed in the two- and four-boson channels. However, the sensitivities from the two-boson channels are expected to be weaker, due to the relatively smaller sizes of the cross-

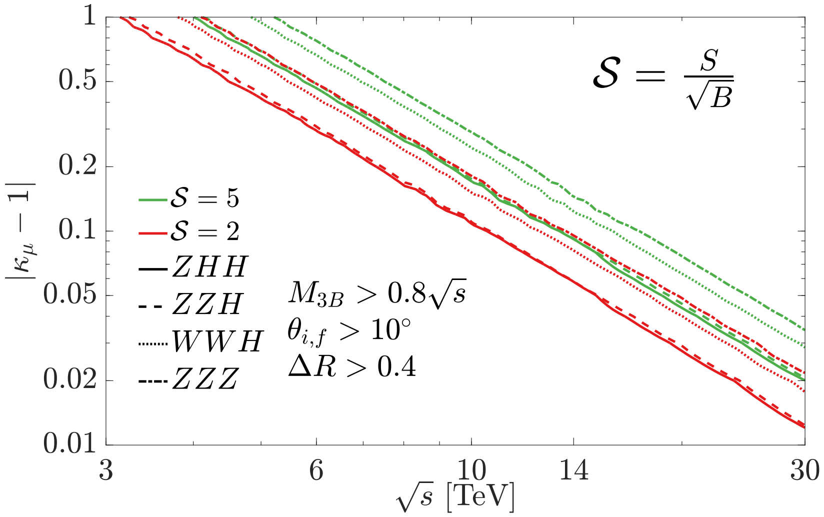

Figure 24: The statistical sensitivity of a high-energy muon collider to the muon Yukawa coupling κ_μ from the measurements of three-boson production.

section deviations from anomalous couplings, shown in Fig. 16. Though in the four-boson channels, the signal-to-background ratios can be larger than that for the triboson channels, the production rates become significantly smaller compared to the three-boson channels. This elevates in our opinion the triple production to the "golden channels" for this kind of measurement. Our event selection is based on imposing an invariant mass cut $M_{3B} > 0.8\sqrt{s}$ in our analysis to enrich the annihilation channels. An opposite selection cut could likewise yield enriched samples of VBF processes; this is also expected to have some sensitivity on anomalous muon-Higgs couplings, based on the deviations shown in Fig. 19(b). As a final remark, annihilation cross sections of (pure) multi-Higgs production do not respect the symmetry in Eq. (235), which provides an opportunity to determine the sign of the deviation $\delta = \kappa_\mu - 1$. Nevertheless, the production rate is so small that not even a single expected event survives the event selection, given the luminosity in Eq. (231). The only chance lies in the single Higgs production with collision energy right on the Higgs mass threshold. We leave all these possibilities to future dedicated studies.

To summarize our results, a high-energy muon collider in the range of $10 - 30$ TeV, combining multi-TeV resolution power with the well-defined and clean leptonic environment, allows probing a tiny and elusive parameter of the SM like the muon Yukaww coupling to the single-digit percent level.

4.1.4 Summary

Motivated by the recent proposal for a multi-TeV muon collider, we explored the sensitivity of testing the muon-Higgs coupling at such a collider. Owing to the small muon-Yukawa coupling in the SM, any new physics contributions to the muon mass generation different from the SM Yukawa formalism would result in relatively large deviations from the SM prediction, and thus deserve special scrutiny at future collider experiments. We claim that a muon collider would be unique in carrying out such explorations. Our results are summarized as follows.

After presenting the scale-dependence of the muon Yukawa coupling in the SM and in an extra-dimensional theory, we discussed parameterizations for deviations of the muon-Yukawa coupling from its SM values within the frameworks of HEFT and SMEFT effective descriptions, and considered the implications on such anomalous couplings from perturbative unitarity bounds. As paradigm observables, we applied this EFT formalism to multi-boson production at a muon collider, particularly the production of two, three and four electroweak gauge bosons associated with a Higgs boson. Our studies show that the sensitivity reach to such anomalous muon-Higgs couplings rises with the number of gauge bosons as the onset of the deviation from the SM is at lower energies. This is due to the fact that processes with higher multiplicities are involved in more insertions of the operators generating the deviations (and of higher operators) with high-energy enhancements and sizeable coupling coefficients.

With the approach of a model independent effective coupling κ_μ, we further performed detailed numerical analyses in Sec. 4.1.3, and found that two-boson production processes have less sensitivity to the muon-Yukawa coupling, while those for four-boson production have lower production rates. Therefore, to demonstrate the feasibility of such a study, we identified the optimal processes of triboson production $\mu^+\mu^- \to W^+W^-H, ZHH$ as prime examples and showed how to isolate this from its most severe background, the same final state produced in vector-boson fusion. Typical observables are diboson correlations, either their invariant masses, their angular distributions or their ΔR distances. In this scenario, a muon collider with up to 30 TeV center-of-mass energy has a sensitivity to deviations of the muon-Yukawa coupling from its SM value of the order of 1%∼4%. This can be interpreted in the SM as a measurement of the muon Yukawa coupling with this precision. In the SMEFT formulation, if we assume an order-1 coupling, this precision would correspond to a probe to a new physics scale of about $\Lambda \sim 30 - 100$ TeV.

There are many ways such an analysis can be improved, *e.g.,* by combining different channels, performing measurements at different energy stages of the machines, by combining final states with different multiplicities, by using multivariate analyses instead of simple cut-based analyses and by using polarization information on the final-state vector bosons. All of this is beyond the scope of this paper and is left for future investigations.

This paper highlights the tantamount possibilities to study one of the most elusive parameters within particle physics, the Higgs-muon coupling, and it also shows in more general context how effective field theories can be utilized to make the utmost use of a discovery facility like the muon collider.

4.2 Higgs boson decay to charmonia via charm quark fragmentation

The milestone discovery of Higgs boson (H) at the CERN Large Hadron Collider (LHC) in 2012 [2, 3] was a remarkable success of the Standard Model (SM) of elementary particle physics and the Electroweak Symmetry Breaking mechanism (EWSB). The outstanding results of the Higgs boson studies by the ATLAS and CMS collaborations at the LHC are consistent with the SM prediction within the current accuracy for the gauge boson final states of $\gamma\gamma, ZZ$ and WW [149, 150, 151], the third generation of fermions for the top quark coupling [152, 153], and the decays to $\tau\bar{\tau}$ [154, 155] and $b\bar{b}$ [156, 157, 158, 159, 160, 161]. The Higgs decays to the second generation fermions, however, are much more challenging to observe because of the much weaker Yukawa couplings. While it is promising to observe $H \to \mu^+\mu^-$ with enough integrated luminosity [91, 92] because of the clean signature [162, 163], the $H \to c\bar{c}$ channel would be extremely difficult to dig out of the data because of the daunting SM di-jet background at the hadron colliders. At present, ATLAS and CMS give the upper limit on Higgs direct decay to charm quark mode of $\sigma(pp \to ZH) \times \mathrm{BR}(H \to c\bar{c}) < 2.7\,\mathrm{pb}$ and $\sigma(VH) \times \mathrm{BR}(H \to c\bar{c}) < 4.5\,\mathrm{pb}$, which are about 100 and 70 times greater than the SM prediction, respectively [164, 165]. Many dedicated efforts have been made to tackle the problem from different directions [166, 167, 168, 169, 170, 171, 172, 164, 173, 174, 175, 165, 176, 177, 178], with limited successes.

A potentially promising method to separate the large QCD background is to consider the decay of the Higgs boson into charmonium associated with a photon, $H \to J/\psi + \gamma$, with effective triggers of $J/\psi \to \mu^+\mu^-$ plus a photon. The branching fraction for this decay mode has been calculated to be $\mathrm{BR}(H \to J/\psi + \gamma) \simeq 2.8 \times 10^{-6}$, within the non-relativistic quantum chromodynamics (NRQCD) framework [167, 168]. Even though the final state from this decay mode is quite distinctive with $J/\psi \to e^+e^-, \mu^+\mu^-$, the branching fraction is still rather small, far below the currently accessible limits 3.5×10^{-4} and 7.6×10^{-4}, given by ATLAS [179] and CMS [180], respectively. In addition, the dominant J/ψ production is from the "vector meson dominance" contribution $\gamma^* \to J/\psi$, rendering this process insensitive to the $Hc\bar{c}$ Yukawa coupling. Other similar processes have been proposed to study the nature Higgs boson [181, 182, 183, 184].

To take advantage of the clear decay of J/ψ, we study another channel with a charmonium production in the Higgs decay

$$H \to c + \bar{c} + J/\psi \text{ (or } \eta_c). \tag{238}$$

The dominant contribution to these decay processes is the fragmentation mechanism built upon the initial decay $H \to c\bar{c}$, where the enhancements from the fragmentations result in a relatively high rate. Within the NRQCD formalism, some diagrams for this process have been previously calculated in the literature [185, 186]. In this paper, we calculate the full leading-order contributions of the charmonium production in Eq. (238) via the fragmentation mechanism, including both QCD and QED contributions. We consider J/ψ and η_c production through both the color-singlet and the color-octet Fock states. We find power/logarithmic enhancements to the total decay width due to the fragmentations of the c quark, the photon splitting and the gluon splitting. We also properly take into account the running mass effect for the charm quark and the electroweak (EW) correction to the Higgs decay width, which have been often neglected in the literature. We find that the decay branching fractions can be about 2×10^{-5} for $H \to c\bar{c} + J/\psi$, and 6×10^{-5} for $H \to c\bar{c} + \eta_c$.

In the light of the upcoming LHC Run 3 and the High-Luminosity LHC (HL-LHC) [187], we comment on the perspective on searching for the Higgs boson to J/ψ transition for testing the charm-quark Yukawa coupling, in terms of the signal statistics and the significant background contamination. The higher rate and a clean $J/\psi \to \mu\bar{\mu}$ signal could make this channel searchable by using the existing LHC data or in the future HL-LHC, and potentially improve the sensitivity on testing the Higgs-Charm Yukawa coupling.

4.2.1 Calculational Formalism

NRQCD is an effective theory derived from QCD in the non-relativistic approximation to describe the behavior of bound states made of heavy quark-antiquark pairs ($Q\bar{Q}$) [188]. It is valid when the velocity v of Q ($\bar{Q}$) in the $Q\bar{Q}$ center of mass frame is nonrelavistic ($v \ll 1$). In the NRQCD framework, the decay width of the Higgs boson can be factorized as

$$\Gamma = \sum_{\mathbb{N}} \hat{\Gamma}_{\mathbb{N}}(H \to (Q\bar{Q})[n] + X) \times \langle \mathcal{O}^h[\mathbb{N}] \rangle, \tag{239}$$

where $\mathbb{N}$ stands for the involved $Q\bar{Q}$ Fock state with quantum numbers $n({}^{2S+1}L_J^{[\text{color}]})$. $\hat{\Gamma}_{\mathbb{N}}$ is the perturbatively calculable short-distance coefficient (SDC), which can be expressed in a differential form

$$\mathrm{d}\hat{\Gamma}_{\mathbb{N}} = \frac{1}{2m_H} \frac{|\mathcal{M}|^2}{\langle \mathcal{O}^{Q\bar{Q}} \rangle} \mathrm{d}\Phi_3, \tag{240}$$

where m_H is the Higgs boson mass, $\langle \mathcal{O}^{Q\bar{Q}} \rangle$ is the long-distance matrix element (LDME) for a free $Q\bar{Q}$ pair Fock state. $\mathcal{M}$ is the perturbative matrix elements from the QCD dynamics and all the spin, color and polarizations are summed over. $\mathrm{d}\Phi_3$ is the 3-body phase space. The last factor in Eq. (239), $\mathcal{O}^h[\mathbb{N}]$ represents the long-distance matrix elements for an exclusive

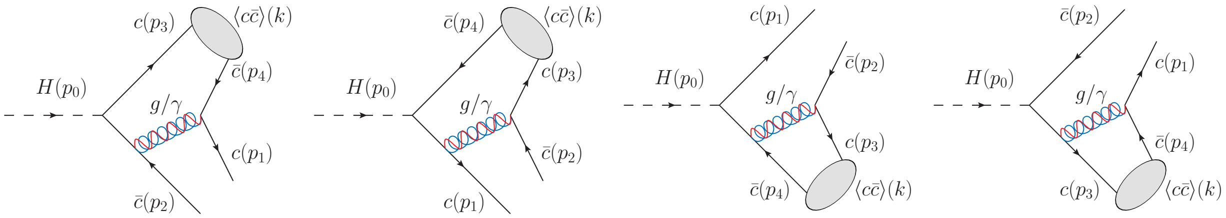

Figure 25: Feynman diagrams for a charmonium Fock state $\langle c\bar{c}\rangle$ production from Higgs decay via charm-quark fragmentation.

hadronic quarkonium state h, that contains all the non-perturbative hadronization information. The leading order color-singlet LDMEs can be related to the wave function at the origin and scale as v^3: $\langle \mathcal{O}^{J/\psi}[^3S_1^{[1]}]\rangle$ and $\langle \mathcal{O}^{\eta_c}[^1S_0^{[1]}]\rangle$. Current phenomenological applications for J/ψ and η_c also include color-octet LDMEs up to order v^7: $\langle \mathcal{O}^{J/\psi}[^3S_1^{[8]}]\rangle$, $\langle \mathcal{O}^{J/\psi}[^1S_0^{[8]}]\rangle$, $\langle \mathcal{O}^{J/\psi}[^3P_J^{[8]}]\rangle$, $\langle \mathcal{O}^{\eta_c}[^3S_1^{[8]}]\rangle$, $\langle \mathcal{O}^{\eta_c}[^1P_1^{[8]}]\rangle$. We next present the calculations according their color quantum numbers of singlet and octet.

4.2.1.1 Color-singlet states

There are two color-singlet (CS) Fock states, $^3S_1^{[1]}$ and $^1S_0^{[1]}$, that respectively contributes to J/ψ and η_c productions. For the Higgs boson decay to a charmonium bound state $\langle c\bar{c}\rangle$ via the CS Fock states,

$$H(p_0) \to c(p_1) + \bar{c}(p_2) + \langle c\bar{c}\rangle(k), \tag{241}$$

the Feynman diagrams are presented in Fig. 25 for the g and γ contributions, and Fig. 26 for additional QED only contributions.

The CS LDMEs can be related to the wave function at the origin $R(0)$ by

$$\langle \mathcal{O}^{J/\psi}[^3S_1^{[1]}]\rangle = \frac{3N_c}{2\pi}|R(0)|^2, \quad \langle \mathcal{O}^{\eta_c}[^1S_0^{[1]}]\rangle = \frac{N_c}{2\pi}|R(0)|^2, \tag{242}$$

using the vacuum saturation approximation, valid up to corrections of order v^4, where $N_c = 3$ is the number of colors. The value of the radial wave function $|R(0)|^2 = 1.0952\,\mathrm{GeV}^3$ can be

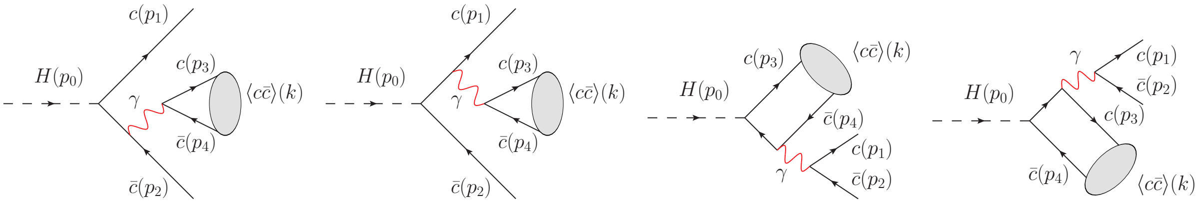

Figure 26: QED Feynman diagrams for color-singlet (CS) charmonium state production via $H \to c + \bar{c} + \langle c\bar{c}\rangle$.

calculated using the potential models [189]. In calculating the SDC as in Eq. (240), we have the LDMEs for the free $Q\bar{Q}$ color-singlets

$$\langle \mathcal{O}^{Q\bar{Q}}\rangle = 6N_c, \text{ for } {}^3S_1^{[1]}, \quad \langle \mathcal{O}^{Q\bar{Q}}\rangle = 2N_c, \text{ for } {}^1S_0^{[1]}. \tag{243}$$

The Feynman amplitudes have the form

$$\mathcal{M} = \frac{y_c}{\sqrt{2}}\frac{\delta_{ij}}{\sqrt{N_c}}\sum_{\ell=1}^{4}\bar{u}(p_1)\epsilon_\alpha\left[\left(C_F g_s^2 + q_c^2 e^2\right)\mathcal{A}_\ell^\alpha + C_A q_c^2 e^2 \mathcal{B}_\ell^\alpha)\right]\Big|_{q=0} v(p_2), \tag{244}$$

where y_c and q_c are the charm-quark Yukawa coupling and the electric charge, respectively. ϵ_α is the polarization vector of the $Q\bar{Q}$ Fock state[5], $q = p_3 - p_4$ is the relative momentum between the constitute quarks Q and $\bar{Q}$, i and j are the color indices of Q and $\bar{Q}$, $C_A = 3$, $C_F = 4/3$, g_s is the strong coupling, and q_c is the charm quark electric charge. The dominant contribution $\mathcal{A}_\ell^\alpha$ is from the "quark fragmentation mechanism", which can be read from the Feynman diagrams in Fig. 25,

$$\begin{aligned}
\mathcal{A}_1^\alpha &= -\frac{\gamma^\nu \Pi_s^\alpha (m_c - \not{p}_1 - \not{p}_2 - \not{p}_4)\gamma^\nu}{(p_1+p_4)^2((p_1+p_2+p_4)^2 - m_c^2)},\\
\mathcal{A}_2^\alpha &= -\frac{\gamma^\nu (m_c + \not{p}_1 + \not{p}_2 + \not{p}_3)\Pi_s^\alpha \gamma^\nu}{(p_2+p_3)^2((p_1+p_2+p_3)^2 - m_c^2)},\\
\mathcal{A}_3^\alpha &= -\frac{(m_c - \not{p}_2 - \not{p}_3 - \not{p}_4)\gamma^\nu \Pi_s^\alpha \gamma^\nu}{(p_2+p_3)^2((p_2+p_3+p_4)^2 - m_c^2)},\\
\mathcal{A}_4^\alpha &= -\frac{\gamma^\nu \Pi_s^\alpha \gamma^\nu (m_c + \not{p}_1 + \not{p}_3 + \not{p}_4)}{(p_1+p_4)^2((p_1+p_3+p_4)^2 - m_c^2)},
\end{aligned} \tag{245}$$

---

[5] For a spin-zero state such as ${}^1S_0^{[1]}$, $\epsilon_\alpha \to 1$ and $\mathcal{A}^\alpha$, $\mathcal{B}_\ell^\alpha$ are scalar functions independent of α, as given explicitly below.

where Π_s^α is a spin projector for a spin-s state. The pure QED amplitudes $\mathcal{B}_\ell^\alpha$ can be read off from Fig. 26,

$$\begin{aligned}
\mathcal{B}_1^\alpha &= \frac{\mathrm{Tr}[\gamma^\nu \Pi_s^\alpha](m_c - \not{p}_2 - \not{p}_3 - \not{p}_4)\gamma^\nu}{(p_3+p_4)^2((p_2+p_3+p_4)^2 - m_c^2)}, \\
\mathcal{B}_2^\alpha &= \frac{\mathrm{Tr}[\gamma^\nu \Pi_s^\alpha]\gamma^\nu(m_c + \not{p}_1 + \not{p}_3 + \not{p}_4)}{(p_3+p_4)^2((p_1+p_3+p_4)^2 - m_c^2)}, \\
\mathcal{B}_3^\alpha &= \frac{\gamma^\nu \mathrm{Tr}[(m_c - \not{p}_1 - \not{p}_2 - \not{p}_4)\gamma^\nu \Pi_s^\alpha]}{(p_1+p_2)^2((p_1+p_2+p_4)^2 - m_c^2)}, \\
\mathcal{B}_4^\alpha &= \frac{\gamma^\nu \mathrm{Tr}[\gamma^\nu(m_c + \not{p}_1 + \not{p}_2 + \not{p}_3)\Pi_s^\alpha]}{(p_1+p_2)^2((p_1+p_2+p_3)^2 - m_c^2)}.
\end{aligned} \tag{246}$$

Thanks to the "single photon fragmentation" (SPF) mechanism in Fig. 26(a,b), the QED diagrams have a notable enhancement to ${}^3S_1^{[1]}$ production via their interference with the QCD diagrams. Meanwhile, for CP conservation, the SPF diagrams are forbidden in ${}^1S_0^{[1]}$ production. The spin projectors Π_s^α for the outgoing heavy quark pair are given by

$$\begin{aligned}
\Pi_0^\alpha &\to \frac{1}{\sqrt{8m_c^3}}\left(\frac{\not{k}}{2} - \not{q} - m\right)\gamma^5\left(\frac{\not{k}}{2} + \not{q} + m\right), \\
\Pi_1^\alpha &= \frac{1}{\sqrt{8m_c^3}}\left(\frac{\not{k}}{2} - \not{q} - m\right)\gamma^\alpha\left(\frac{\not{k}}{2} + \not{q} + m\right),
\end{aligned} \tag{247}$$

for spin-0 and spin-1 states respectively, where $k = p_3 + p_4$. By substituting Eqs. (242)$-$(247) into Eq. (239), one obtains the decay width of $\Gamma(H \to c\bar{c} + J/\psi(\eta_c))$ through the CS states. The polarization sum formulae are listed in Appx. D.

4.2.1.2 Color-octet states

A key property of NRQCD is that a quarkonium can also be produced through color-octet (CO) Fock states. The CO LDMEs have to be extracted from fitting the experimental data with the NRQCD calculations. Different fitting strategies result in different values of LDMEs; some of the recent CO LDMEs fitting results for the J/ψ production are listed in Table 8. In our computation, a combined fit of CDF and CMS J/ψ production data for the CO LDMEs [190] is employed. One reason for choosing this extraction is due to the fact that it relies on high p_T hadronic data. Since the possible factorization issues at small p_T are not present for the Higgs decay, we feel that the extraction in Ref. [190] is closest to

Reference	$\langle\mathcal{O}^{J/\psi}[^1S_0^{[8]}]\rangle$	$\langle\mathcal{O}^{J/\psi}[^3S_1^{[8]}]\rangle$	$\langle\mathcal{O}^{J/\psi}[^3P_0^{[8]}]\rangle/m_c^2$
G. Bodwin, *et al* [190]	$(9.9 \pm 2.2) \times 10^{-2}$	$(1.1 \pm 1.0) \times 10^{-2}$	$(4.89 \pm 4.44) \times 10^{-3}$
K.T. Chao, *et al* [191]	$(8.9 \pm 0.98) \times 10^{-2}$	$(3.0 \pm 1.2) \times 10^{-3}$	$(5.6 \pm 2.1) \times 10^{-3}$
Y. Feng, *et al* [192]	$(5.66 \pm 4.7) \times 10^{-2}$	$(1.77 \pm 0.58) \times 10^{-3}$	$(3.42 \pm 1.02) \times 10^{-3}$

Table 8: Some fitted numerical values of color-octet (CO) LDMEs for J/ψ production (in units of GeV^3)

our current interest, and will thus use these as our canonical value for the LDMEs. We also note another merit that the CO LDMEs in Ref. [190] is independent of the value of the wave function at origin.

Based on the heavy quark spin symmetry (HQSS), there exist the following relations

$$\begin{aligned}\langle\mathcal{O}^{\eta_c}[^1S_0^{[1,8]}]\rangle &= \frac{1}{3}\langle\mathcal{O}^{J/\psi}[^3S_1^{[1,8]}]\rangle,\\ \langle\mathcal{O}^{\eta_c}[^3S_1^{[8]}]\rangle &= \langle\mathcal{O}^{J/\psi}[^1S_0^{[8]}]\rangle, \quad \langle\mathcal{O}^{\eta_c}[^1P_1^{[8]}]\rangle = 3\langle\mathcal{O}^{J/\psi}[^3P_0^{[8]}]\rangle,\end{aligned} \tag{248}$$

that allow us to relate all the needed LDMEs to those in Table 8.

The SDC calculation for the CO states is similar to those for the CS ones, with the free $Q\bar{Q}$ pair state LDMEs

$$\begin{aligned}&\langle\mathcal{O}^{Q\bar{Q}}(^1S_0^{[8]})\rangle = (N_c^2-1), \quad \langle\mathcal{O}^{Q\bar{Q}}(^3S_1^{[8]})\rangle = 3(N_c^2-1),\\ &\langle\mathcal{O}^{Q\bar{Q}}(^1P_1^{[8]})\rangle = 3(N_c^2-1), \ \langle\mathcal{O}^{Q\bar{Q}}(^3P_J^{[8]})\rangle = (2J+1)(N_c^2-1), \ J = 0,\,1,\,2.\end{aligned} \tag{249}$$

In addition to the Feynman diagrams in Fig. 25, there are new QCD Feynman diagrams for the CO final states, as shown in Fig. 27. The "single gluon fragmentation" (SGF) diagrams in Fig. 27(a,b) contribute only to $^3S_1^{[8]}$ and causes it to dominant over the other CO states. The Fig. 27(c,d) diagrams are non-zero only for the $^3S_1^{[8]}$ and the $^1P_1^{[8]}$ cases due to the CP symmetry. Again, following Eq. (240), the CO Feynman amplitudes can be written as

$$\mathcal{M} = \frac{y_c}{\sqrt{2}}\bar{u}(p_1)\mathcal{M}'v(p_2), \tag{250}$$

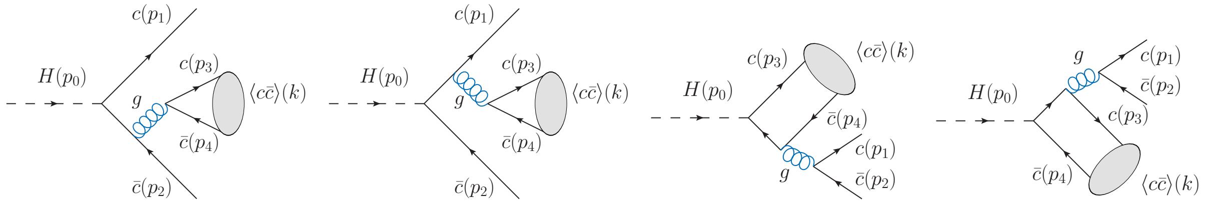

Figure 27: Feynman diagrams for color-octet (CO) charmonium state production. (a) and (b) are the single gluon fragmentation to ${}^3S_1^{[8]}$ state, while (c) and (d) contribute to both ${}^3S_1^{[8]}$ and ${}^1P_1^{[8]}$ states.

where

$$\mathcal{M}' = \sqrt{2}\epsilon_\alpha \left\{ \left[\left(T^a T^b T^a\right)_{ij} g_s^2 + T^b_{ij} q_c^2 e^2 \right] \sum_{\ell=1}^{4} \mathcal{A}_\ell^\alpha + \frac{T^b_{ij}}{2} g_s^2 \sum_{\ell=1}^{4} \mathcal{B}_\ell^\alpha) \right\} \Bigg|_{q=0} , \tag{251}$$

for s-wave states (note $\epsilon_\alpha \to 1$ and $\mathcal{B}_\ell^\alpha \to 0$ for ${}^1S_0^{[8]}$),

$$\mathcal{M}' = \sqrt{2}\epsilon_\beta \frac{\mathrm{d}}{\mathrm{d}q_\beta} \left\{ \left[\left(T^a T^b T^a\right)_{ij} g_s^2 + T^b_{ij} q_c^2 e^2 \right] \sum_{\ell=1}^{4} \mathcal{A}_\ell^\alpha + \frac{T^b_{ij}}{2} g_s^2 \sum_{\ell=3}^{4} \mathcal{B}_\ell^\alpha) \right\} \Bigg|_{q=0} \tag{252}$$

for ${}^1P_1^{[8]}$, and

$$\mathcal{M}' = \sqrt{2}\mathcal{E}_{\alpha\beta} \frac{\mathrm{d}}{\mathrm{d}q_\beta} \left[\left(T^a T^b T^a\right)_{ij} g_s^2 + T^b_{ij} q_c^2 e^2 \right] \sum_{\ell=1}^{4} \mathcal{A}_\ell^\alpha \Bigg|_{q=0} \tag{253}$$

for ${}^3P_J^{[8]}$ ($J = 0,\ 1,\ 2$). The polarization vector and tensor are denoted by ϵ_α and $\mathcal{E}_{\alpha\beta}$, and b is for the color of the CO $Q\bar{Q}$ Fock state.

A special remark is in order about the color-octet mechanism in the J/ψ and η_c production. As described in Eq. (239), the decay width Γ can be factorized into the LDME $\langle \mathcal{O}^h[\mathbb{N}] \rangle$ and the SDC $\hat{\Gamma}_{\mathbb{N}}$, following the NRQCD framework. The CO LDMEs are in higher orders of v than the CS ones as

$$\begin{aligned} &\frac{\langle \mathcal{O}^{J/\psi}({}^1S_0^{[8]}) \rangle}{\langle \mathcal{O}^{J/\psi}({}^3S_1^{[1]}) \rangle} \sim \mathcal{O}(v^3), \quad \frac{\langle \mathcal{O}^{J/\psi}({}^3S_1^{[8]}) \rangle}{\langle \mathcal{O}^{J/\psi}({}^3S_1^{[1]}) \rangle} \sim \mathcal{O}(v^4), \quad \frac{\langle \mathcal{O}^{J/\psi}({}^3P_J^{[8]}) \rangle}{\langle \mathcal{O}^{J/\psi}({}^3S_1^{[1]}) \rangle} \sim \mathcal{O}(v^4), \\ &\frac{\langle \mathcal{O}^{\eta_c}({}^3S_1^{[8]}) \rangle}{\langle \mathcal{O}^{\eta_c}({}^1S_0^{[1]}) \rangle} \sim \mathcal{O}(v^3), \quad \frac{\langle \mathcal{O}^{\eta_c}({}^1P_1^{[8]}) \rangle}{\langle \mathcal{O}^{\eta_c}({}^1S_0^{[1]}) \rangle} \sim \mathcal{O}(v^4), \end{aligned} \tag{254}$$

	Fig. 25			Fig. 26	Fig. 27
	QCD	QED	QCD× QED	QED	QCD
CS	16/9	1	4/3	9	-
CO	2/9	8	$-4/3$	-	2

Table 9: Color factors of different Feynman diagrams for the CS and CO SDCs. The pure QCD contribution, pure QED contribution and the QCD/QED interference are represented as QCD, QED, and QCD×QED, respectively.

which naively suppresses the rates to produce J/ψ and η_c via the CO states. The SDCs for different Fock states can be very different since they may include different contributing diagrams and therefore different color structures. We present the color factors of different Feynman diagrams for the CS and CO SDCs in Table 9. As shown in the table, the QCD quark fragmentation mechanism (the Feynman diagrams with a gluon propagator in Fig. 25) is suppressed in the CO productions by a factor of 8. Among all the CO states, ${}^3S_1^{[8]}$ has the largest SDC, due to both its relatively larger color factor of Fig. 27 and the large logarithmic SGF enhancement from Fig. 27(a,b). For the other CO states, *i.e.* ${}^1S_0^{[8]}$, ${}^1P_1^{[8]}$, and ${}^3P_J^{[8]}$, the main production process is via charm-quark fragmentation as shown in Fig. 25, where the QED diagrams make sizeable contributions via the QCD/QED interference terms because of a large color factor.

4.2.1.3 Electroweak contributions

Besides the Feynman diagrams in Figs. 25, 26 and 27, we also consider the electroweak (EW) production mechanism through the HZZ coupling, as shown in Fig. 28. The color factors of these two Feynman diagrams are listed in Table 10. The Feynman diagram in Fig. 28(a) could give a sizable correction for the CS states productions for both its relatively larger color factor (5 times of the charm quark QCD fragmentation) and the resonance enhancement of the on-shell Z splitting to a pair of free $c\bar{c}$. For Fig. 28(b), one of the two Z propagators could be very closed to Z mass shell with $p_Z^2 \leq m_H^2/2 - 4m_c^2 \simeq (88.34\ \text{GeV})^2$, so

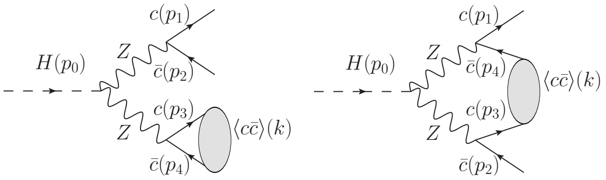

Figure 28: Feynman diagrams for charmonium state production through the HZZ coupling.

	Fig. 28(a)	Fig. 28(b)
CS	9	1
CO	-	8

Table 10: Color factors of the HZZ diagrams for the CS and CO SDCs.

its contribution is also non-negligible. Particularly, for the CO state production, where only Fig. 28(b) exists, the EW correction can be quite large due to nearly on-shell Z enhancement and the relatively larger color factor (36 times of the charm quark QCD fragmentation). We note this EW contribution possesses contamination to the charm-Yukawa coupling measurement. Numerical comparisons will be shown in the following section.

Before ending this section, one remark is in order. Owing to the large top-quark Yukawa coupling, the Higgs boson decay via the top-quark loop may be substantial. The best known example, as the Higgs boson discovery channel, is $gg \to H$ and $H \to \gamma\gamma$, which would also contribute to the final state of our current interest. We show the contributing Feynman diagrams for $H \to g^*g^*/\gamma^*\gamma^* \to J/\psi + c\bar{c}$ in Fig. 29. The branching fraction for the g^*g^* contribution is estimated to be around 2.5×10^{-6} in the heavy top limit, which is significantly smaller than that from the charm-Yukawa contributions. As already noted earlier, the decay $H \to J/\psi + \gamma$ is dominated by the VMD contribution via $H \to \gamma^*\gamma \to J/\psi + \gamma$. The photon splitting will contribute to the final state under our consideration $H \to \gamma^*\gamma^* \to J/\psi + c\bar{c}$. However, it is quite small, less than 2×10^{-7}. We will not discuss those contributions further.

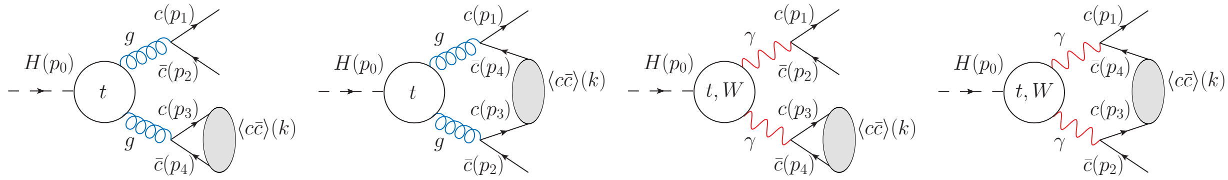

Figure 29: Feynman diagrams for charmonium state production with top-quark and W loop contributions. The gluonic diagram in (a) only contributes to ${}^3S_1^{[8]}$, while the photon one in (c) only contributes to ${}^3S_1^{[1]}$.

4.2.2 Phenomenological results

4.2.2.1 Standard Model results

In our numerical calculations, the SM parameters are taken as

$$
\begin{aligned}
&1/\alpha = 132.5, \quad \alpha_s(2m_c) = 0.2353, \quad m_c^{\text{pole}} = 1.500 \text{ GeV}, \quad m_c(m_H) = 0.6942 \text{ GeV}, \\
&m_H = 125.0 \text{ GeV}, \quad m_W = 80.42 \text{ GeV}, \quad m_Z = 91.19 \text{ GeV}, \quad v = 246.2 \text{ GeV},
\end{aligned}
$$

where the QCD running coupling $\alpha_s(2m_c)$ and the charm quark running mass $m_c(m_H)$ are obtained by running from $\alpha_s(m_Z) = 0.1181$ [193] and $m_c(3 \text{ GeV}) = 1.012$ GeV [194] at one-loop level.[6] The SM Yukawa coupling at the scale of the Higgs boson mass is

$$
y_c^{\text{SM}} = \frac{\sqrt{2} m_c(m_H)}{v} \approx 3.986 \times 10^{-3},
$$

which gives a branching fraction $\text{BR}(H \to c\bar{c}) = 2.9\%$, consistent with Ref. [89].

The numerical SDCs can be obtained by substituting the Feynman amplitudes Eq. (244) and Eq. (250) into Eq. (240). We decompose the SDCs into pure QCD contribution, pure QED contribution, QCD/QED interference, the EW correction, and present the ratios of the SDCs to the corresponding pure QCD values $\hat{\Gamma}_{\mathbb{N}}/\hat{\Gamma}_{\mathbb{N}}^{\text{QCD}}$ in Table 11. The QCD diagrams dominate for the SDCs of both the CS states and most of the CO states, especially for ${}^3S_1^{[8]}$.

---

[6] The amplitude square can be analytically simplified using `FeynCalc` [195, 196, 197], the numerical parameters for the SM parameters, $\alpha_s(Q)$ running, and $m_c(Q)$ running are implemented using `para` [6, 198].

$\hat{\Gamma}_{\mathbb{N}}/\hat{\Gamma}_{\mathbb{N}}^{\mathrm{QCD}}$	${}^1S_0^{[1]}$	${}^3S_1^{[1]}$	${}^1S_0^{[8]}$	${}^3S_1^{[8]}$	${}^1P_1^{[8]}$	${}^3P_0^{[8]}$	${}^3P_1^{[8]}$	${}^3P_2^{[8]}$
QCD	1.0	1.0	1.0	1.0	1.0	1.0	1.0	1.0
QED	1.1×10^{-4}	0.077	0.0073	1.1×10^{-5}	0.0068	0.0073	0.0073	0.0073
QCD×QED	0.021	0.14	-0.17	0.0012	-0.15	-0.17	-0.17	-0.17
EW	0.24	0.051	0.28	2.6×10^{-4}	1.4	0.29	0.33	1.5

Table 11: The ratios of the SDCs to their pure QCD values $\hat{\Gamma}_{\mathbb{N}}/\hat{\Gamma}_{\mathbb{N}}^{\mathrm{QCD}}$. The pure QCD contribution, pure QED contribution, QCD/QED interference, and EW correction are marked as QCD, QED, QCD×QED, and EW, respectively.

The QED diagrams introduce sizable corrections mainly via the QCD/QED interference, which affects different Fock states differently:

- For ${}^3S_1^{[1]}$, the QED contribution is enhanced by both the logarithmic enhancement and the large color factor of the single-photon-fragmentation diagrams (Fig. 26 (a, b)). Together with the QCD/QED interference, the total QED correction is around 22% compared to the pure QCD contribution.
- For ${}^1S_0^{[1]}$, the Fig. 26 diagrams are forbidden by CP conservation, leading to the total QED correction of only 2%.
- For ${}^3S_1^{[8]}$, the QCD contribution is absolutely dominant for the single-gluon-fragmentation diagrams (Fig. 27 (a,b)), for which both the QED and EW corrections are orders of magnitude smaller.
- For ${}^1S_0^{[8]}$ and ${}^3P_J^{[8]}$, the charm-quark fragmentation (Fig. 25) is the only production channel. The QCD and QED Feynman diagrams have exactly the same topology and the corresponding amplitudes differ from each other only by the couplings and the color factors. The QCD/QED interference is negative becasue of its negative color factor, and the ratio could be estimated as $\hat{\Gamma}_{\mathbb{N}}^{\mathrm{QCD}\times\mathrm{QED}}/\hat{\Gamma}_{\mathbb{N}}^{\mathrm{QCD}} = -12q_c^2\alpha/\alpha_s = -0.171$.
- The ${}^1P_1^{[8]}$ case is quite similar to the above one, where the charm-quark fragmentation is the most dominant production channel. The only difference is that there exist Fig. 27 (c, d) diagrams that result in a relatively smaller QCD/QED contribution.

	QCD [CS]	QCD+QED [CS]	Full [CS]	Full [CO]	Full [CS+CO]
$\Gamma(H \to c\bar{c} + J/\psi)$ (GeV)	4.8×10^{-8}	5.8×10^{-8}	6.1×10^{-8}	2.2×10^{-8}	8.3×10^{-8}
$\mathrm{BR}(H \to c\bar{c} + J/\psi)$	1.2×10^{-5}	1.4×10^{-5}	1.5×10^{-5}	5.3×10^{-6}	2.0×10^{-5}
$\Gamma(H \to c\bar{c} + \eta_c)$ (GeV)	4.9×10^{-8}	5.1×10^{-8}	6.3×10^{-8}	1.8×10^{-7}	2.4×10^{-7}
$\mathrm{BR}(H \to c\bar{c} + \eta_c)$	1.2×10^{-5}	1.2×10^{-5}	1.5×10^{-5}	4.5×10^{-5}	6.0×10^{-5}

Table 12: The decomposed numerical values of $\Gamma(H \to c\bar{c} + J/\psi(\eta_c))$ and the corresponding branching fractions.

Owing to the combination of the larger color factor and the on-shell Z enhancement, the EW corrections from the HZZ diagrams (Fig. 28) is also sizable. The relative size of the EW correction is process dependent. The correction for ${}^1S_0^{[1]}$ is larger than that of ${}^3S_1^{[1]}$ because the $Zf\bar{f}$ axial coupling is larger than its vector counterpart. For the CO states, the EW corrections are also significant, $\sim 30\%$ of the QCD contributions for ${}^1S_0^{[8]}$ and ${}^3P_{J=0,\,1}^{[8]}$, and $\sim 140\%$ of the QCD contributions for ${}^1P_1^{[8]}$ and ${}^3P_2^{[8]}$.

For numerical calculations, we employ the J/ψ color-octet LDMEs from Ref. [190], which is independent of the choice of the color-singlet LDMEs. Given the SDCs and the LDMEs, it is then straightforward to obtain the decay width $\Gamma(H \to c\bar{c} + J/\psi(\eta_c))$ and the corresponding branching fractions. We decompose the total decay width into CS QCD only, CS QCD+QED, full CS, full CO, and full CS+CO and present the numerical results in Table 12. The results for the charm-quark fragmentation into CS states are rather robust. In addition, the QED diagrams introduce a 22% (2%) correction to J/ψ (η_c) production and the EW correction is 5% (24%) for J/ψ (η_c). It is interesting to compare the two mechanisms of the CS and CO production. The production rate of J/ψ (η_c) through CO Fock states is around 36% (295%) of the CS one, which is due mainly to the large ${}^3S_1^{[8]}$ SDC via the single-gluon fragmentation diagrams. We see that the CO contribution to J/ψ production is about 1/3 of the total; while it is about a factor of 3 larger than the CS contribution for η_c production, because of the large value of $\langle \mathcal{O}^{\eta_c}[{}^3S_1^{[8]}] \rangle = \langle \mathcal{O}^{J/\psi}[{}^1S_0^{[8]}] \rangle$. We find it instructive to examine the contributions in some details from different CO states as shown in Table 13, where the dominance of ${}^3S_1^{[8]}$ is shown ($\sim 95\%$ (100%) the total CO rate of J/ψ (η_c) production). We quote our final results as

$$\mathrm{BR}(H \to c\bar{c} + J/\psi) = (2.0 \pm 0.5) \times 10^{-5}, \tag{255}$$

$$\mathrm{BR}(H \to c\bar{c} + \eta_c) = (6.0 \pm 1.0) \times 10^{-5}, \tag{256}$$

where the quoted errors are calculated by using the conservative estimate from the ${}^3S_1^{[8]}$ LDME fitting as in Ref. [190]. More work in fitting the LDMEs needs to be done to reduce the uncertainty and improve the precision. In comparison with the well-studied decay mode $\mathrm{BR}(H \to J/\psi + \gamma) = 2.8 \times 10^{-6}$ [167, 168], we see an enhancement by an order of magnitude, which is a result of the fragmentation mechanisms.

The J/ψ and η_c energy distributions $\mathrm{d}\Gamma/\mathrm{d}E_{J/\psi(\eta_c)}$ are presented in Fig. 30. As shown in the plots, the SPF and SGF diagrams have dramatic enhancement on ${}^3S_1^{[1]}$ and ${}^3S_1^{[8]}$ production in the low meson energy range, and the charm-quark fragmentation dominates the relative high energy region. As for the EW contribution, it is quite interesting to recognize the enhancements by the approximate two-body kinematics evidenced by the two contributing diagrams as shown in Fig. 28: the first diagram yields an on-shell Z process at $E_{J/\psi(\eta_c)} = \frac{1}{2}m_H(1 - m_Z^2/m_H^2 + 4m_c^2/m_H^2) \approx 30$ GeV; and the second diagram results in a back-to-back kinematics at $E_{J/\psi(\eta_c)} \approx E_{c\bar{c}} \approx m_H/2$. These features will serve as an effective discriminator against the contamination from the non-Yukawa contributions.

From the observational point of view, it is important to predict the transverse momentum spectrum for the decay products. We show the transverse momentum distributions in the Higgs rest frame for $H \to c\bar{c} + J/\psi$ (η_c) in Fig. 31: (a) and (b) for J/ψ and η_c distributions, respectively; (c) and (d) for the charm quark distributions associated with J/ψ and η_c, respectively, where the solid curves are for the p_T^{max} and dashed curves are for the p_T^{min} distribution. We see that the contribution from the color-octet tends to be softer in $p_{T,J/\psi}$ due to the single-gluon-splitting mechanism, as seen in (a,b); while the p_T^{min} distribution of the charm quark from the color-singlet tends to be softer, as seen in (c,d), consistent with the fact that the color-signlet mesons are harder.

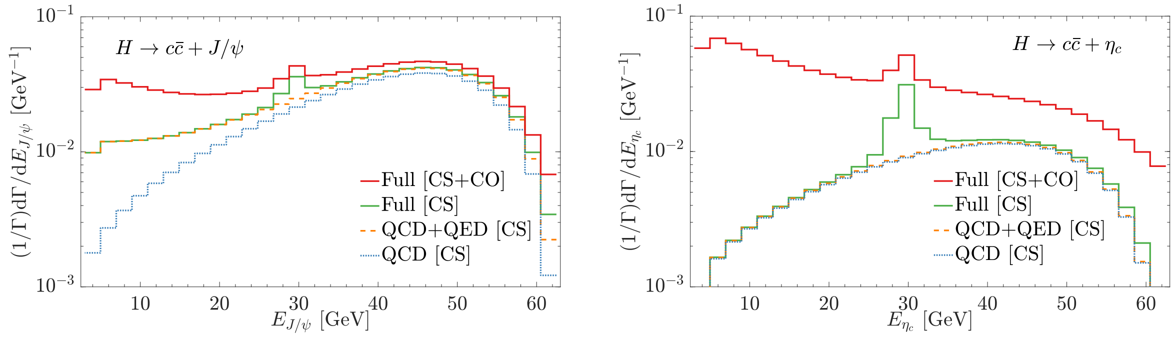

Figure 30: Charmonium energy distributions for (a) J/ψ and (b) η_c. The blue dotted and orange dashed curves are for color-singlet (CS) QCD only and QCD+QED contributions, the red (green) solid curve is for the sum of full leading order (full CS) result. All curves are normalized using the full leading order decay width in Table 12.

4.2.2.2 Probing the charm quark Yukawa

Given the clean decay channels $J/\psi \to \mu^+\mu^-$ and e^+e^-, we will focus on our discussion to the J/ψ mode. With the predicted decay branching fraction of 2×10^{-5} for $H \to c\bar{c} + J/\psi$ and the Higgs production cross section at the LHC as $\sigma_H \approx 50$ pb, we will expect a signal rate of 1000 event per ab^{-1} integrated luminosity. It is thus promising to search for this channel at the HL-LHC [187]. We would like to reiterate that the leading contribution to this process directly involves the charm-quark Yukawa coupling, unlike the process $H \to J/\psi + \gamma$ where the leading contribution is from $\gamma^* \to J/\psi$.

For simplicity, we adopt the κ framework [166] and allow the charm quark Yukawa coupling y_c to deviate from the SM value y_c^{SM} by a factor of κ_c

$$y_c = \kappa_c y_c^{\mathrm{SM}}. \tag{257}$$

Neglecting the sub-leading contributions from the EW and top-loop diagrams, the branching fractions and thus the production rates for the processes under consideration scale with the charm-Yukawa coupling as

$$\mathrm{BR} \approx \kappa_c^2 \, \mathrm{BR}^{\mathrm{SM}}. \tag{258}$$

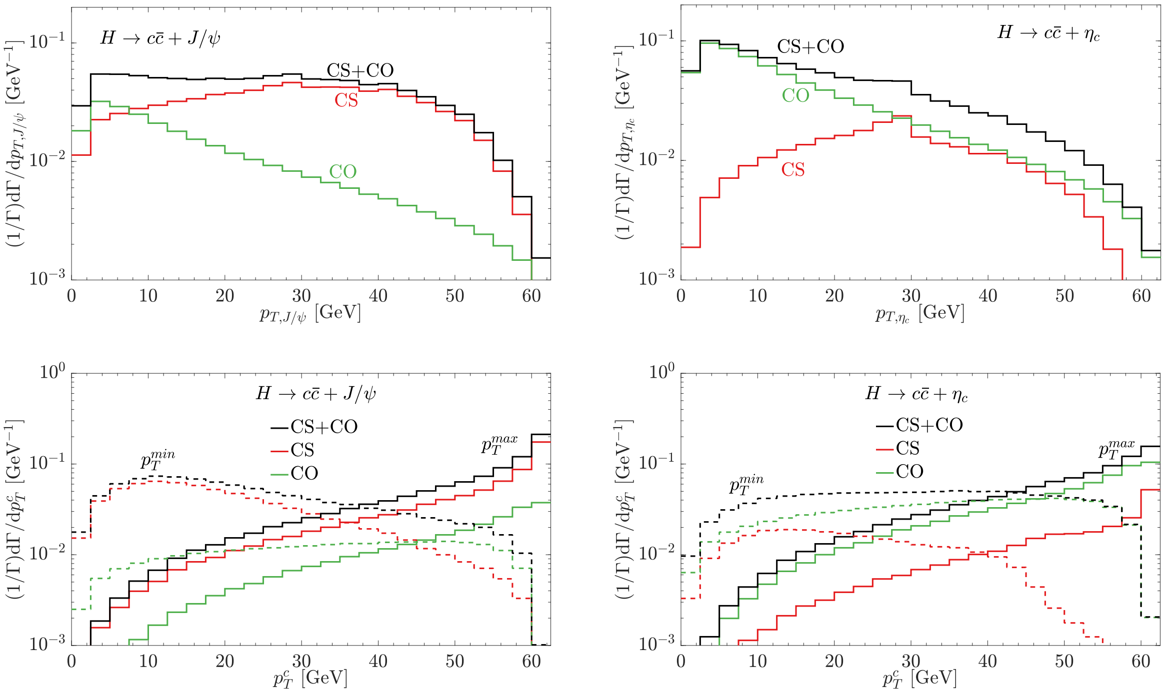

Figure 31: Transverse momentum distributions in the Higgs rest frame $H \to c\bar{c} + J/\psi$ (η_c): (a) and (b) for J/ψ and η_c distributions, respectively; (c) and (d) for the charm quark distributions associated with J/ψ and η_c, respectively, where the solid curves are for the p_T^{max} and dashed curves are for the p_T^{min} distribution. The red, green and black curves are for CS, CO, and the full leading order result. All curves are normalized using the full leading order decay width in Table 12.

	${}^3S_1^{[8]}$	${}^1S_0^{[8]}$	${}^1P_1^{[8]}$	${}^3P_J^{[8]}$	Total
$\Gamma(H \to c\bar{c} + J/\psi)$ (GeV)	2.0×10^{-8}	9.8×10^{-10}	-	2.2×10^{-10}	2.2×10^{-8}
$\mathrm{BR}(H \to c\bar{c} + J/\psi)$	5.0×10^{-6}	2.4×10^{-7}	-	5.3×10^{-8}	5.3×10^{-6}
$\Gamma(H \to c\bar{c} + \eta_c)$ (GeV)	1.8×10^{-7}	3.6×10^{-11}	1.0×10^{-10}	-	1.8×10^{-7}
$\mathrm{BR}(H \to c\bar{c} + \eta_c)$	4.5×10^{-5}	8.9×10^{-9}	2.5×10^{-8}	-	4.5×10^{-5}

Table 13: The CO contributions to $\Gamma(H \to c\bar{c} + J/\psi(\eta_c))$ and the branching fractions.

Assuming a detection efficiency ϵ for the final state $c\bar{c} + \ell^+\ell^-$ ($\ell = \mu, e$) and an integrated luminosity L, we write the anticipated number of events as

$$N = L\sigma_H \, \epsilon \, \mathrm{BR}(c\bar{c} + \ell^+\ell^-) \approx 12 \, \kappa_c^2 \times \frac{L}{\mathrm{ab}^{-1}} \times \frac{\epsilon}{10\%}, \tag{259}$$

where the 12% branching fraction for $J/\psi \to \mu^+\mu^-, e^+e^-$ has been included.[7] Considering the statistical error only $\delta N \sim \sqrt{N}$, one would get an accuracy for the coupling determination

$$\Delta\kappa_c \approx 15\% \times (\frac{L}{\mathrm{ab}^{-1}} \times \frac{\epsilon}{10\%})^{-1/2}. \tag{260}$$

In Fig. 32, we show the J/ψ and η_c energy distributions for a few illustrative couplings $\kappa_c = 1$ (SM), 3, 5, by the red, green and blue curves, respectively. We note that, the results confirm the simple, yet important, relation in Eq. (258). The EW contribution is seen near $E_{J/\psi(\eta_c)} \approx 30$ GeV, that does not follow this relation, and it becomes invisible for larger values of κ_c. To have a more complete comparison, we also employ the four-loop charm quark running mass $m_c(m_H) = 0.629$ GeV via the package RunDec [199, 200] in addition to the one-loop $m_c(m_H) = 0.694$ GeV, as shown by the dashed curves correspondingly. The color-octet long-distance matrix element (LDME) uncertainties are indicated by the colored bands around the solid curves. We see that the uncertainty is more significant at the low energy region, due to the enhancement of the single-gluon-fragmentation diagrams to the ${}^3S_1^{[8]}$ contribution which has a large uncertainty.

---

[7] The 10% efficiency for ϵ is a rough estimate with a double charm tagging of $(40\%)^2$ [164], and a kinematic acceptance of 50% based on the distributions in Fig. 31.

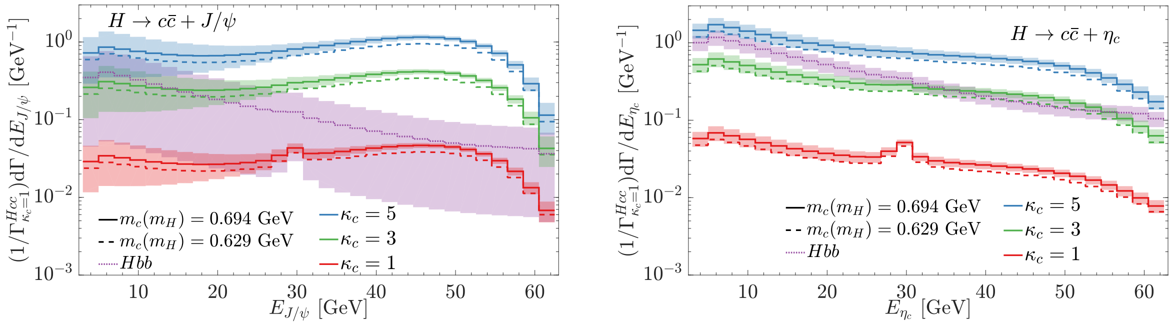

Figure 32: Charmonium energy distributions for (a) J/ψ and (b) η_c for $\kappa_c = 1$ (SM), 3, 5. The solid curves are for the one-loop running mass $m_c(m_H) = 0.694$ GeV; the dashed curves are for the four-loop running mass $m_c(m_H) = 0.629$ GeV. The dotted purple curve is for the background from Hbb decay mode. The colored bands are for the uncertainties from the CO LDMEs. All curves are normalized using the full SM leading order decay width in Table 12.

4.2.2.3 Backgrounds

In the realistic experimental search for the signal $H \to c\bar{c} + J/\psi$ at the LHC, there are large backgrounds to the signal.

The quarkonium production mechanism could result in hadronic jets associated with the quarkonium state, which serve as the main background for the signal $H \to c\bar{c} + J/\psi$. The formidable background is the associated production of J/ψ and light g, q-jets. The cross section of the prompt J/ψ production has been measured to be $\mathrm{BR}(J/\psi \to \mu^+\mu^-) \times \sigma(pp \to J/\psi) \simeq 860$ pb for $20 \leq p_T \leq 150$ GeV, with a data sample of 2.3 fb^{-1} by CMS [201],[8] where the J/ψ state is reconstructed in the dimuon decay channel for dimuon rapidity $|y| < 1.2$. Requiring to tag two additional charm-like jets from the inclusive J/ψ sample would likely reduce this background rate by several orders of magnitude. Detailed simulation would be needed for charm tagging and kinematic optimization in order to draw a quantitative conclusion for the signal observability.

The leading irreducible background comes from the QCD production of J/ψ plus heavy

---

[8] We obtained the cross section by summing over the data from their differential cross section.

flavor jets, *i.e.* $gg, q\bar{q} \to c\bar{c} + J/\psi$. As presented in Ref. [202], the cross section falls sharply versus the transverse momentum, dropping by 4 orders of magnitude at $p_T \simeq 20$ GeV. Experimental measurements of such processes at the LHC have not yet been performed, but the high performance of jet flavor tagging at ATLAS/CMS offers potential for the future measurements at the HL-LHC [203]. The event yield was estimated to be 75000 with an integrated luminosity of 3 ab^{-1} [203], translating to a cross section of 25 fb. Although this background rate is large comparing with the expected signal about 1 fb, their kinematical distributions are quite different from the Higgs decay. We may expect to reduce the background by applying some suitable judicious kinematic cuts.

In addition, due to the larger $Hb\bar{b}$ coupling, the decay $H \to b\bar{b} + J/\psi(\eta_c)$, as shown in Fig. 33, may yield significant contamination to the test of the charm-Yukawa coupling. Following our calculational formalism, it is straightforward to obtain the corresponding branching fractions as

$$\begin{aligned} \text{BR}(H \to b\bar{b} + J/\psi) &= (8.6 \pm 7.5) \times 10^{-5}, \\ \text{BR}(H \to b\bar{b} + \eta_c) &= (7.4 \pm 1.6) \times 10^{-4}, \end{aligned} \tag{261}$$

where the main contribution is through the ${}^3S_1^{[8]}$ state and the errors are estimated using the uncertainty of $\langle \mathcal{O}^{J/\psi}[{}^3S_1^{[8]}] \rangle$. We note the large uncertainty which is attributed to both the large Hbb coupling and the single-gluon-fragmentation enhancement. To appreciate the relative size, we present the charmonium energy distributions from $b\bar{b} + J/\psi$ (η_c) productions in Fig. 32, as shown by the purple curve. The band around it indicates the uncertainty.[9] Its overall rate is about a factor of 4 larger than that of $c\bar{c} + J/\psi$. It is quite conceivable that an effective charm-tagging would be implemented to separate those two contributions in the experimental analysis.

---

[9] The $H \to b\bar{b} + J/\psi$ was recently calculated to NLO in α_s [204]; our estimation is consistent with their LO results under the same parameter settings.

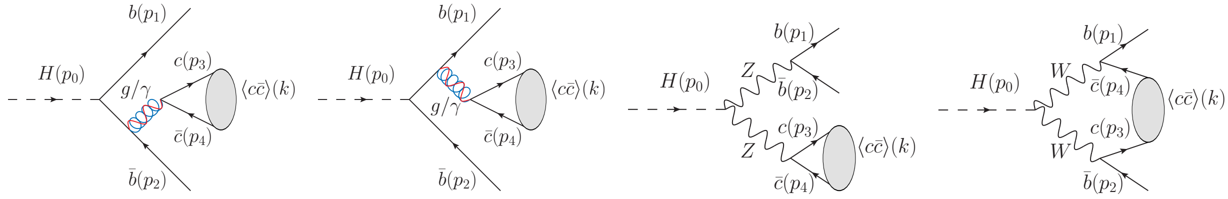

Figure 33: Feynman diagrams for $H \to b\bar{b} + J/\psi(\eta_c)$ production. The gluon diagrams in (a, b) only contribute to ${}^3S_1^{[8]}$, while the photon ones only contribute to ${}^3S_1^{[1]}$. (c) is nonzero only for the CS states.

4.2.3 Summary

It is of fundamental importance to study the Higgs boson couplings to light fermions. It is extremely challenging to test the charm-quark Yukawa coupling at hadron colliders due to the large QCD background to the decay $H \to c\bar{c}$. Instead, other decay modes that may be sensitive to the coupling have been suggested. In this paper, we considered a new decay channel, the Higgs boson decay to J/ψ and η_c states via the charm-quark fragmentation. We calculated the branching fractions for the decays in Eq. (238). The decay rates are governed by the charm-quark Yukawa coupling y_c, unlike the decay $H \to J/\psi + \gamma$, which is dominated by the γ^*-J/ψ mixing.

We performed the calculation in the framework of NRQCD, including the contributions of both the color-singlet and color-octet mechanisms, as well as the electroweak contributions from the HZZ coupling. For the color-singlet production, we adopted the long-distance matrix elements (LDMEs) from the most updated value of wave function at origin $R(0)$ [189]. For the color-octet production mechanism, the LDMEs would have to be extracted from fitting the experimental data. There is a significant uncertainty from the fitting [190, 191, 192], and we adopt the results from Ref. [190], which used the high p_T data as input, more relevant to the situation of our current consideration.

It is interesting to note the different relative sizes from contributions of color-singlet versus color-octet. Numerically, we found that the contribution from the color-singlet state is about three times larger for J/ψ (but three times smaller for η_c) than that from the color-octet states. We found the electroweak contributions to the decay via the HZZ coupling to be small for ${}^3S_1^{[1]}$ (the color-singlet contribution to J/ψ) and ${}^3S_1^{[8]}$ (the main color-octet contribution to both J/ψ and η_c), at the order of percentage. We finally commented on the sub-leading contributions from $H \to g^*g^*$ via the top-quark loop, and from $H \to \gamma^*\gamma^*$ via the top-quark and W loops. We conclude that the decay branching fractions are

$$\mathrm{BR}(H \to c\bar{c} + J/\psi) \approx 2.0 \times 10^{-5} \quad \text{and} \quad \mathrm{BR}(H \to c\bar{c} + \eta_c) \approx 6.0 \times 10^{-5}. \tag{262}$$

We comment on the perspective on searching for the Higgs to J/ψ transition at the HL-LHC for testing the charm-quark Yukawa coupling. If only based on the statistics, with the large Higgs boson production rate anticipated at the HL-LHC of 50 million per ab^{-1}, we would expect to reach a sensitivity of about 15% on the coupling y_c, which is in the same ballpark as the $\sim$ 25% theoretical uncertainty in Eq. (255) and the $\sim$ 16% EW contamination from the HZZ (3%) and the $H \to g^*g^*/\gamma^*\gamma^*$ (13%) channels. There are, however, formidable SM QCD backgrounds for this channel. Assuming $10,000$ background events after the selection cuts at the HL-LHC, one could reach a 2σ sensitivity for the coupling $\kappa_c \approx 2.4$. Detailed analyses including the detector and the systematic effects would be called for to reach a quantitative conclusion.

Our formalism and results are also applicable to the Higgs decays to other fragmentation channels with heavy quarkonia, if the heavy quark mass is properly adjusted, as explicitly shown for $H \to b\bar{b} + J/\psi$ (η_c) in Eq. (261).

5.0 Conclusions

We study the electroweak (EW) physics and Higgs physics at high-energy colliders. The key features of the studies in previous chapters are collected as following:

Electroweak parton distribution functions

For future high-energy colliders, the machine energy is far above the EW scale so that the massive EW bosons can be radiated off from the beam particles. Along this line, all the particles in the Standard Model (SM) should be treated as "partons" of the beam particle and described using the parton distribution function (PDF) formalism. In Chapter 2, we briefly introduce the existing "Equivalent photon approximation" (EPA) and "effective weak boson approximation" (EWA) and then present a formalism for the EW PDFs at the Leading-Log (LL) accuracy. We demonstrate the the procedure to solve the Dokshitzer–Gribov–Lipatov–Altarelli–Parisi (DGLAP) evolution of the SM electroweak PDFs. The discussions are based on Ref. [6, 7].

The partonic picture of future high-energy lepton colliders

For collisions well above the EW scale, the EW gauge boson content of the high-energy lepton beams becomes increasingly relevant, similar to the gauge content of gluon content of high-energy hadron beams. In this sense, a future ultra-high-energy lepton collider can be treated as an electroweak version of LHC, where the vector boson fusion (VBF) channel becomes important. In Chapter 3, we use the EW PDFs formalism to draw the partonic picture of future Multi-TeV level high-energy lepton colliders. The partonic luminosities of a possible high-energy muon collider and the cross sections of typical SM processes are calculated in Sec. 3.1. In addition, we also analyze the QCD jet production to estimate the largest background of future lepton colliders in Sec. 3.2. The results have been reported in Ref. [6, 7, 45].

Yukawa couplings of the second generation fermions

The discovery of the Higgs boson at CERN LHC is a milestone that marks the end of one era and the dawn of another. The next target in high-energy physics is to search for the hint of new physics beyond the SM. Since it is directly related to the electroweak symmetry breaking mechanism, Higgs is regarded as the portal to new physics. In Chapter 4, we suggest two approaches to test the Muon-Higgs coupling and the Charm-Higgs coupling respectively. By the subtle interplay between the muon Yukawa coupling y_μ in the high energy production of multiple bosons, we have shown that it is possible to measure y_μ to an accuracy of ten percent at a 10-TeV muon collider in Sec. 4.1. In Sec. 4.2, we use the non-relativistic QCD framework to study the Higgs boson decay to charmonia (J/ψ and η_c meson) and a pair of free charm quarks. Our results show that the $H \to J/\psi + c\bar{c}$ process can be used to measure the Charm-Higgs coupling at a 3 ab^{-1} high-luminosity LHC and it is possible to constrain $\kappa_c \leq 2.4$. These two studies are published in Ref. [86] and Ref. [87], respectively.

Appendix A Rotation of Wavefunctions

In the derivation of splitting functions, one need to consider the rotations of the spinors and polarization vectors along $\hat{2}$ axis in $\hat{1}$-$\hat{3}$ plane.

The rotation of polarization vector is

$$\epsilon^{\mu} \to e^{-i\theta_{zx}}\epsilon^{\mu} = \begin{pmatrix} \cos\theta & -\sin\theta \\ \sin\theta & \cos\theta \end{pmatrix}_{zx} \epsilon^{\mu}. \tag{263}$$

More explicitly, we write the transverse polarization vector as

$$\epsilon^{\mu}_{\pm} = \frac{1}{\sqrt{2}}(0, 1, \pm, 0) \to \frac{1}{\sqrt{2}}(0, \cos\theta, \pm i, -\sin\theta), \tag{264}$$

which can be approximatly rewriten as

$$\frac{1}{\sqrt{2}}(0, 1, \pm i, -\theta), \tag{265}$$

when θ is small.

The rotation of a spinor u is

$$u \to e^{-i\theta\sigma_2}u = \begin{pmatrix} \cos\theta/2 & -\sin\theta/2 \\ \sin\theta/2 & \cos\theta/2 \end{pmatrix} u. \tag{266}$$

In collinear limit, i.e. $\theta \ll 1$, spinors transform as

$$\xi_{-} = \begin{pmatrix} 0 \\ 1 \end{pmatrix} \to \begin{pmatrix} -\sin\theta/2 \\ \cos\theta/2 \end{pmatrix} \simeq \begin{pmatrix} -\theta/2 \\ 1 \end{pmatrix}, \tag{267}$$

and

$$\xi_{+} = \begin{pmatrix} 1 \\ 0 \end{pmatrix} \to \begin{pmatrix} \cos\theta/2 \\ -\sin\theta/2 \end{pmatrix} \simeq \begin{pmatrix} 1 \\ \theta/2 \end{pmatrix}. \tag{268}$$

Appendix B The splitting functions

In this appendix, we list all the splitting functions. The QED⊗QCD splitting functions involving the leptons and photon are given as

$$P_{\gamma\gamma} = -\frac{\alpha}{2\pi}\left(N_\ell + N_c\sum_q e_q^2\right)\frac{2}{3}\delta(1-x), \quad P_{\ell\ell} = \frac{\alpha}{2\pi}\left[\frac{1+x^2}{(1-x)_+} + \frac{3}{2}\delta(1-x)\right], \tag{269}$$

$$P_{\ell\gamma} = \frac{\alpha}{2\pi}\left[x^2 + (1-x)^2\right], \qquad P_{\gamma\ell} = \frac{\alpha}{2\pi}\frac{1+(1-x)^2}{x}, \tag{270}$$

$$P_{q\gamma} = N_c e_q^2\frac{\alpha}{2\pi}\left[x^2 + (1-x)^2\right], \qquad P_{\gamma q} = e_q^2\frac{\alpha}{2\pi}\frac{1+(1-x)^2}{x}. \tag{271}$$

where $q = u, d$. The quark charges are $e_u = 2/3$, and $e_d = -1/3$. The splitting of $\gamma \to q\bar{q}$ contains a color factor $N_c = 3$ to sum over all the possible final states.

The quark and gluon splitting functions are

$$P_{gg} = \frac{\alpha_3}{2\pi}2C_A\left[\frac{1-x}{x} + \frac{x}{(1-x)_+} + x(1-x)\right] + \frac{\alpha_3}{2\pi}\frac{\beta_0}{2}\delta(1-x), \tag{272}$$

$$P_{qq} = \left(e_q^2\frac{\alpha}{2\pi} + C_F\frac{\alpha_3}{2\pi}\right)\left[\frac{1+x^2}{(1-x)_+} + \frac{3}{2}\delta(1-x)\right], \tag{273}$$

$$P_{qg} = \frac{\alpha_3}{2\pi}T_F\left[x^2 + (1-x)^2\right],\ P_{gq} = \frac{\alpha_3}{2\pi}C_F\frac{1+(1-x)^2}{x}, \tag{274}$$

where $\beta_0 = \frac{11}{3}C_A - \frac{4}{3}T_F(N_u + N_d)$. The QCD group constants are

$$C_A = 3,\ T_F = 1/2,\ C_F = 4/3. \tag{275}$$

The complete EW splitting functions can be constructed from Refs. [13, 43, 6]. We list the polarized splitting functions as

$$P_{f_L f_L} = P_{f_R f_R} = P_{ff} = \frac{1+x^2}{(1-x)_+} + \frac{3}{2}\delta(1-x),\ P_{f_L f_R} = P_{f_R f_L} = 0, \tag{276}$$

$$P_{V_+ f_L} = P_{V_- f_R} = \frac{(1-x)^2}{x},\ P_{V_- f_L} = P_{V_+ f_R} = \frac{1}{x}, \tag{277}$$

$$P_{f_L V_+} = P_{f_R V_-} = \frac{1}{2}(1-x)^2,\ P_{f_L V_-} = P_{f_R V_+} = \frac{1}{2}x^2 \tag{278}$$

$$\begin{aligned} P_{V_+V_+} &= P_{V_-V_-} = \frac{1}{4}\left[\frac{11}{3}C_{A2} - \frac{4}{3}T_F(N_g + N_c N_g)\right]\delta(1-x) \\ &\quad + \frac{C_{A2}}{2}\left[\frac{1+x}{(1-x)_+} + \frac{1}{x} - x(1+x)\right], \end{aligned} \tag{279}$$

$$P_{V_+V_-} = P_{V_-V_+} = \frac{C_{A2}}{2}\frac{(1-x)^3}{x}. \tag{280}$$

We have the $SU(2)_L$ group constants $C_{A2} = 2$ and $C_{F2} = 3/4$. The $N_g + N_c N_g$ is to sum the generations for the lepton and quark doublets. The gluon splitting functions are

$$\begin{aligned} P_{g_+g_+} &= P_{g_-g_-} = \frac{1}{4}\left[\frac{11}{3}C_A - \frac{4}{3}T_F 2N_g\right]\delta(1-x) \\ &\quad + \frac{C_A}{2}\left[\frac{1+x}{(1-x)_+} + \frac{1}{x} - x(1+x)\right], \qquad (281) \\ P_{g_+g_-} &= P_{g_-g_+} = \frac{C_A}{2}\frac{(1-x)^3}{x}. \qquad (282) \end{aligned}$$

where $2N_g$ sums over all the up- and down-type quarks. We have restored the plus-prescription to deal with the soft singularity in the $x \to 1$ limit, which is different from the cutoff $x < 1 - M_Z/Q$ adopted in Refs. [13, 43].

Then we construct the splitting functions in the (T,CP) basis.

$$P^{\pm}_{ff} = P_{f_Lf_L} \pm P_{f_Lf_R} = P_{ff}, \quad P^{\pm}_{VV} = P_{V_+V_+} \pm P_{V_+V_-}, \qquad (283)$$

$$P^{\pm}_{Vf} = P_{V_+f_L} \pm P_{V_-f_L}, \qquad P^{\pm}_{fV} = P_{f_LV_+} \pm P_{f_LV_-}. \qquad (284)$$

The self splittings involving the virtual B boson are

$$P^{\pm}_{BB} = -\frac{1}{6}N_g\left[4Y_\ell^2 + Y_e^2 + N_c\left(4Y_q^2 + 2Y_u^2 + 2Y_d^2\right)\right]\delta(1-x), \qquad (285)$$

$$P^{\pm}_{BW} = -\frac{1}{6}N_g\left[4Y_\ell + N_c 4Y_q\right]\frac{1}{2}\delta(1-x). \qquad (286)$$

The coefficient of the mixing splitting $P^{\pm}_{BW}$ contains a hyper charge and a $SU(2)_L$ gauge coupling.

As for now, we can construct all the splitting functions in Eqs. (167-170). The splittings into $SU(2)_L$ doublets are

$$P^{0\pm}_{LL} = \left(\frac{\alpha_1}{2\pi}Y_\ell^2 + \frac{\alpha_2}{2\pi}C_{F2}\right)P^{\pm}_{ff}, \qquad P^{0\pm}_{LB} = N_g\frac{\alpha_1}{2\pi}Y_\ell^2 P^{\pm}_{fV}, \qquad (287)$$

$$P^{0\pm}_{LW} = N_g\frac{\alpha_2}{2\pi}C_{F2}P^{\pm}_{fV}, \qquad (288)$$

$$P^{0\pm}_{QQ} = \left(\frac{\alpha_1}{2\pi}Y_q^2 + \frac{\alpha_2}{2\pi}C_{F2} + \frac{\alpha_3}{2\pi}C_F\right)P^{\pm}_{ff}, \quad P^{0\pm}_{QB} = N_cN_g\frac{\alpha_1}{2\pi}Y_q^2 P^{\pm}_{fV}, \qquad (289)$$

$$P^{0\pm}_{QW} = N_cN_g\frac{\alpha_2}{2\pi}C_{F2}P^{\pm}_{fV}, \qquad P^{0\pm}_{Qg} = N_g\frac{\alpha_3}{2\pi}T_F P^{\pm}_{fV}. \qquad (290)$$

The splittings into $SU(2)_L$ singlets are

$$P^{0\pm}_{EE} = \frac{\alpha_1}{2\pi} Y_e^2 P^{\pm}_{ff}, \; P^{0\pm}_{EB} = \pm N_g \frac{\alpha_1}{2\pi} Y_e^2 P^{\pm}_{fV}, \tag{291}$$

$$P^{0\pm}_{UU} = \left(\frac{\alpha_1}{2\pi} Y_u^2 + \frac{\alpha_3}{2\pi} C_F\right) P^{\pm}_{ff}, \; P^{0\pm}_{UB} = \pm N_c N_g \frac{\alpha_1}{2\pi} Y_u^2 P^{\pm}_{fV}, \tag{292}$$

$$P^{0\pm}_{Ug} = \pm N_g \frac{\alpha_3}{2\pi} T_F P^{\pm}_{fV}, \; P^{0\pm}_{DD} = \left(\frac{\alpha_1}{2\pi} Y_d^2 + \frac{\alpha_3}{2\pi} C_F\right) P^{\pm}_{ff}, \tag{293}$$

$$P^{0\pm}_{DB} = \pm N_c N_g \frac{\alpha_1}{2\pi} Y_d^2 P^{\pm}_{fV}, \; P^{0\pm}_{Dg} = \pm N_g \frac{\alpha_3}{2\pi} T_F P^{\pm}_{fV}. \tag{294}$$

Keep in mind that the signs of $f^{0-}_{L,R} \leftarrow B$ are ±. The splittings into gluon are

$$P^{0\pm}_{gQ} = 4\frac{\alpha_3}{2\pi} C_F P^{\pm}_{Vf}, \quad P^{0\pm}_{gU} = \pm 2\frac{\alpha_3}{2\pi} C_F P^{\pm}_{Vf}, \tag{295}$$

$$P^{0\pm}_{gD} = \pm 2\frac{\alpha_3}{2\pi} C_F P^{\pm}_{Vf}, \quad P^{0\pm}_{gg} = \frac{\alpha_3}{2\pi} P^{\pm}_{gg}. \tag{296}$$

The splittings into B are

$$P^{0\pm}_{BB} = P^{\pm}_{BB}, \quad P^{0\pm}_{BL} = \frac{\alpha_1}{2\pi} 4Y_\ell^2 P^{\pm}_{Vf}, \quad P^{0\pm}_{BQ} = \frac{\alpha_1}{2\pi} 4Y_q^2 P^{\pm}_{Vf}, \tag{297}$$

$$P^{0\pm}_{BE} = \pm\frac{\alpha_1}{2\pi} 2Y_e^2 P^{\pm}_{Vf}, \quad P^{0\pm}_{BU} = \pm\frac{\alpha_1}{2\pi} 2Y_u^2 P^{\pm}_{Vf}, \quad P^{0\pm}_{BD} = \pm\frac{\alpha_1}{2\pi} 2Y_d^2 P^{\pm}_{Vf}. \tag{298}$$

The splittings into W are

$$P^{0\pm}_{WL} = \frac{\alpha_2}{2\pi} P^{\pm}_{Vf}, \quad P^{0,1\pm}_{WQ} = \frac{\alpha_2}{2\pi} P^{\pm}_{Vf}, \quad P^{0\pm}_{WW} = \frac{\alpha_2}{2\pi} P^{\pm}_{VV}. \tag{299}$$

For the splittings involving 1± states, we have

$$P^{1\pm}_{LL} = -\frac{1}{4}\frac{\alpha_2}{2\pi} P^{\pm}_{ff}, \quad P^{1\pm}_{LW} = N_g \frac{1}{2}\frac{\alpha_2}{2\pi} P^{\mp}_{fV}, \tag{300}$$

$$P^{1\pm}_{QQ} = -\frac{1}{4}\frac{\alpha_2}{2\pi} P^{\pm}_{ff}, \quad P^{1\pm}_{QW} = N_c N_g \frac{\alpha_2}{2\pi}\frac{1}{2} P^{\mp}_{fV}, \tag{301}$$

$$P^{1\pm}_{LM} = N_g \frac{\alpha_M}{2\pi}\frac{Y_\ell}{2} P^{\pm}_{fV}, \quad P^{1\pm}_{QM} = N_c N_g \frac{\alpha_M}{2\pi}\frac{Y_q}{2} P^{\pm}_{fV}, \tag{302}$$

$$P^{1\pm}_{WL} = \frac{\alpha_2}{2\pi} P^{\mp}_{Vf}, \quad P^{1\pm}_{WQ} = \frac{\alpha_2}{2\pi} P^{\mp}_{Vf}, \tag{303}$$

$$P^{1\pm}_{ML} = \frac{\alpha_M}{2\pi} 4Y_\ell P^{\pm}_{Vf}, \quad P^{1\pm}_{MQ} = \frac{\alpha_M}{2\pi} 4Y_q P^{\pm}_{Vf}, \tag{304}$$

$$P^{1\pm}_{WW} = \frac{\alpha_2}{2\pi} P^{\mp}_{VV}, \quad P^{1\pm}_{MM} = \frac{\alpha_M}{2\pi} P^{\pm}_{BW}. \tag{305}$$

The symbol M indicates the mixing state BW. Finally, the 2± splitting is

$$P^{2\pm}_{WW} = -\frac{\alpha_2}{2\pi}\frac{1}{2} P^{\pm}_{VV}. \tag{306}$$

Appendix C The running of the Muon Yukawa Coupling

When testing the muon-Higgs Yukawa coupling, it is necessary to properly take into account the energy-scale dependence of the coupling, which is a fundamental prediction in quantum field theory. The specific form of this running depends on the particle spectrum and their interactions in the underlying theory. In the electroweak sector of the SM, the dominant contribution to the renormalization group (RG) running is the top Yukawa coupling, followed by the strong and EW gauge interactions.

For the sake of illustration, the coupled renormalization group equations (RGEs) of Yukawa couplings y_μ, y_t, vacuum expectation value v, and gauge couplings g_i are given in the $\overline{\rm MS}$ scheme at leading order (LO) in one-loop by [205, 206, 207, 208, 209, 210, 211]

$$\beta_{y_t} = \frac{\mathrm{d}y_t}{\mathrm{d}t} = \frac{y_t}{16\pi^2}\left(\frac{9}{2}y_t^2 - 8g_3^2 - \frac{9}{4}g_2^2 - \frac{17}{20}g_1^2\right), \tag{307}$$

$$\beta_{y_\mu} = \frac{\mathrm{d}y_\mu}{\mathrm{d}t} = \frac{y_\mu}{16\pi^2}\left(3y_t^2 - \frac{9}{4}(g_2^2 + g_1^2)\right), \tag{308}$$

$$\beta_v = \frac{\mathrm{d}v}{\mathrm{d}t} = \frac{v}{16\pi^2}\left(\frac{9}{4}g_2^2 + \frac{9}{20}g_1^2 - 3y_t^2\right), \tag{309}$$

$$\beta_{g_i} = \frac{\mathrm{d}g_i}{\mathrm{d}t} = \frac{b_i g_i^3}{16\pi^2}, \tag{310}$$

with $t = \ln(Q/M_Z)$ and the coefficients b_i for the gauge couplings (g_1, g_2, g_3) given as

$$b_i^{\rm SM} = (41/10, -19/6, -7). \tag{311}$$

We show the LO RGE running of the muon Yukawa y_μ in the SM in Fig. 34 (red solid curve) and the SM vacuum expectation value v in Fig. 35 (left axis) as functions of the energy scale Q, respectively. With the relation

$$m_\mu(Q) = y_\mu(Q)v(Q)/\sqrt{2},$$

we also show the running of the muon mass, $m_\mu(Q)$, in Fig. 35 (right axis). At the energy scales accessible in near future colliders, the change in y_μ is observed to be rather small, for

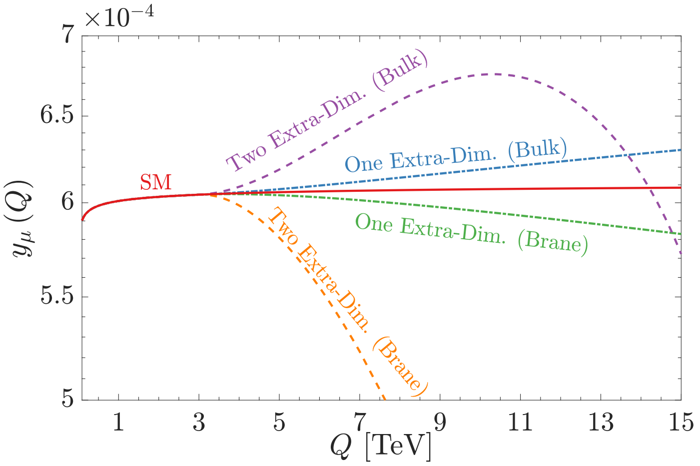

Figure 34: LO RGE running of the muon Yukawa y_μ coupling as a function of the energy scale Q, in the SM (red solid). In the extra-dimensional scenarios (with inverse radius $1/R = 3$ TeV), we consider 1) Bulk: all fields propagating in the bulk, and 2) Brane: all matter fields localized to the brane.

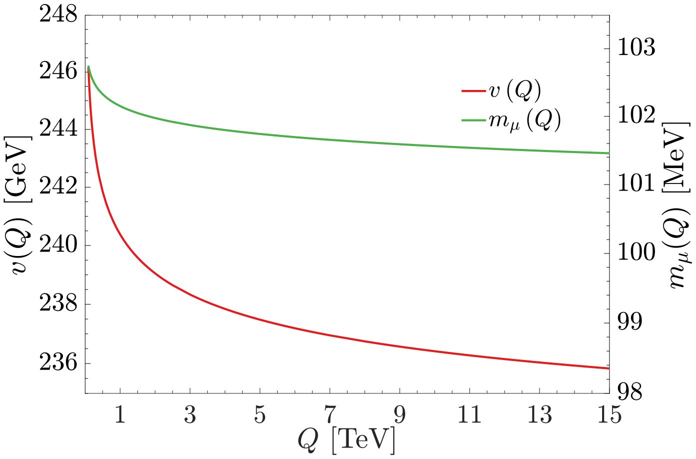

Figure 35: LO RGE running of SM vacuum expectation value v (left scale) and muon mass m_μ (right scale) as functions of the energy scale Q.

example, $y_\mu(Q = 15\ \text{TeV})$ is found to be around 3% smaller compared to $y_\mu(M_Z)$. Similarly, v (m_μ) runs down by about 4% (2%).

New states appearing in beyond SM scenarios can modify the running of the relevant gauge and Yukawa couplings. Generically, the beta function for a coupling λ is given as

$$\beta_\lambda = \beta_\lambda^{\text{SM}} + \sum_{\text{s: massive new states}} \theta(Q - M_s) \times N_s \beta_{s,\lambda}^{\text{NP}} , \tag{312}$$

where $\beta_\lambda^{\text{SM}}$ is the SM beta function, and $\beta_{s,\lambda}^{\text{NP}}$ represents the contribution of a new heavy state s of mass M_s, with N_s number of degenerate degrees of freedom. The theta function encodes the fact that the effect of new heavy states is included in the RG running once the energy scale Q is above the threshold M_s, ignoring here for simplicity the effect of threshold corrections.

In extensions of the SM, the muon-Higgs Yukawa coupling could also be affected both at the tree level and at the quantum level. In addition, the Higgs sector may show a rich flavor structure. In flavor-sensitive Higgs models, the SM prediction for the Yukawa couplings is lost, and the Yukawa couplings become free model parameters. The physical coupling of the SM Higgs to muons may be larger or smaller than its expected SM value. In principle, it could be completely absent, such that the muon mass is generated by other means. The assumption we make for the study in this paper is that the muon Yukawa coupling is a free parameter, as the mass generation for the muon is in general a mixture of the SM mechanism and a yet-unknown mechanism. A typical example for this is a Two-Higgs doublet model (2HDM), or in a general multi-doublet model, that generates third-generation Yukawa couplings, while the second generation couplings are from a different sector (a sample implementation of such a mechanism can be found in [212]). Clearly, the LHC offers also some opportunities to probe first and second generation Higgs Yukawa couplings to light quarks [213], which applies mostly to the Higgs charm Yukawa coupling [167, 182, 169, 214], and maybe even strange tagging is possible at a future Higgs factory [215]. In weakly-coupled theories, the running effects for the muon-Yukawa coupling are rather moderate, similar in size to that in the SM. We will not show it separately.

An interesting question is also whether there could be considerable CP violation in the Higgs Yukawa sector beyond CKM, where there are bounds e.g. for the electron Yukawa coupling [216]. Though it is perfectly possible in our setup in Sec. 4.1.2 to discuss CP-violating operators for the muon Yukawa couplings, such a study is beyond the scope of this current paper.

We add the remark that additional, flavor-dependent, higher-dimensional operators that are responsible for a deviation of the SM muon Yukawa coupling could easily lead to flavor-violating Yukawa couplings that induced $H \to e\mu$. This has been studied e.g. in [217], however, we are not further investigating such flavor-violating processes in this paper. The EFT setup for our study is presented in detail in the next section.

Large modifications to the running couplings compared to the SM case are not expected in four-dimensional quantum field theories essentially due to the logarithmic nature of the running. A qualitatively different scenario however is obtained if there is a tower of new physics states modifying the RGEs, asymptotically leading to a power-law running of the Yukawa coupling [218, 219]. This four-dimensional description is equivalent to a theory with compactified flat extra space-like dimensions, with gauge and/or matter fields propagating in the higher-dimensional bulk. To illustrate this, we consider two scenarios of compactified flat extra-dimensions [220]: a 5D model with the extra-dimension compactified on an S_1/Z_2 orbifold, and a 6D model with the two extra dimensions compactified on a square T^2/Z_2 orbifold [220, 221]. In both models, we consider two cases: 1) all SM fields propagating in the bulk and 2) the SM gauge fields to be propagating in the bulk, with the matter fields of the SM restricted to the brane [222, 223, 224, 225, 226]. The beta functions of the gauge couplings in such scenarios are given as:

$$\begin{aligned} b_i^{5\mathrm{D}} &= b_i^{\mathrm{SM}} + (S(t)-1) \times \left[\left(\frac{1}{10}, -\frac{41}{6}, -\frac{21}{2} \right) + \frac{8}{3}\eta \right] \\ b_i^{6\mathrm{D}} &= b_i^{\mathrm{SM}} + (\pi S(t)^2-1) \times \left[\left(\frac{1}{10}, -\frac{13}{2}, -10 \right) + \frac{8}{3}\eta \right] . \end{aligned} \tag{313}$$

Here, $S(t)$ counts the number of degrees of freedom $S(t) = e^t R$, R being the radius of the extra dimension, η being the number of generations of fermions propagating in the bulk. The corresponding one-loop RGE equations for the Yukawa couplings y_t, y_μ in the extra-dimensional scenarios are as follows [227, 223, 226]

$$\frac{dy_t}{dt} =\beta_{y_t}^{\rm SM} + \frac{y_t}{16\pi^2} 2(S(t)-1)\left(\frac{3}{2}y_t^2 - 8g_3^2 - \frac{9}{4}g_2^2 - \frac{17}{20}g_1^2\right), \qquad \text{5D Brane,} \tag{314a}$$

$$\frac{dy_\mu}{dt} =\beta_{y_\mu}^{\rm SM} - \frac{y_\mu}{16\pi^2} 2(S(t)-1)\left(\frac{9}{4}g_2^2 + \frac{9}{4}g_1^2\right), \qquad \text{5D Brane,} \tag{314b}$$

$$\frac{dy_t}{dt} =\beta_{y_t}^{\rm SM} + \frac{y_t}{16\pi^2} (S(t)-1)\left(\frac{15}{2}y_t^2 - \frac{28}{3}g_3^2 - \frac{15}{8}g_2^2 - \frac{101}{120}g_1^2\right), \qquad \text{5D Bulk,} \tag{314c}$$

$$\frac{dy_\mu}{dt} =\beta_{y_\mu}^{\rm SM} + \frac{y_\mu}{16\pi^2} (S(t)-1)\left(6y_t^2 - \frac{15}{8}g_2^2 - \frac{99}{40}g_1^2\right), \qquad \text{5D Bulk.} \tag{314d}$$

$$\frac{dy_t}{dt} =\beta_{y_t}^{\rm SM} + \frac{y_t}{16\pi^2} 4\pi(S(t)^2-1)\left(\frac{3}{2}y_t^2 - 8g_3^2 - \frac{9}{4}g_2^2 - \frac{17}{20}g_1^2\right), \qquad \text{6D Brane,} \tag{315a}$$

$$\frac{dy_\mu}{dt} =\beta_{y_\mu}^{\rm SM} - \frac{y_\mu}{16\pi^2} 4\pi(S(t)^2-1)\left(\frac{9}{4}g_2^2 + \frac{9}{4}g_1^2\right), \qquad \text{6D Brane,} \tag{315b}$$

$$\frac{dy_t}{dt} =\beta_{y_t}^{\rm SM} + \frac{y_t}{16\pi^2} \pi(S(t)^2-1)\left(9y_t^2 - \frac{32}{3}g_3^2 - \frac{3}{2}g_2^2 - \frac{5}{6}g_1^2\right), \qquad \text{6D Bulk,} \tag{315c}$$

$$\frac{dy_\mu}{dt} =\beta_{y_\mu}^{\rm SM} + \frac{y_\mu}{16\pi^2} \pi(S(t)^2-1)\left(6y_t^2 - \frac{3}{2}g_2^2 - \frac{27}{10}g_1^2\right), \qquad \text{6D Bulk.} \tag{315d}$$

We see from Fig. 34 that in the presence of such a tower of new states, the running of y_μ can be substantially altered for both the 5D (dot-dashed curves), and 6D (dashed curves) models. We note that the effects only become significant when close or above the new physics threshold, $1/R \sim 3$ TeV in our illustration. Above the threshold, the other more direct effects from the existence of the extra dimensions may be observable as well and a coordinated search would be beneficial.

We conclude that while in the SM the energy dependence of the y_μ is a minor effect, there are viable models where the value and the running of this quantity could both follow completely different patterns, as illustrated above with extra-dimensional scenarios. In the next subsection, we will extend this direction in the EFT framework.

Appendix D Polarization sum

In order to perform the proper polarization sums, we define

$$\Pi_{\alpha\beta} \equiv -g_{\alpha\beta} + \frac{P_\alpha P_\beta}{m^2}, \tag{316}$$

where $m = 2m_c$ is the mass of the $Q\bar{Q}$ bound state.

- For ${}^3S_1$ and ${}^1P_1$ states, the polarization sum is

$$\sum_h \epsilon_\alpha \epsilon^*_{\alpha'} = \Pi_{\alpha\alpha'}, \tag{317}$$

- For ${}^3P_J$ states, there are three multiplets, *i.e.* $J = 0, 1, 2$. We need to define the polarization tensor $\mathcal{E}^{(J)}_{\alpha\beta}$

$$\begin{aligned}
\mathcal{E}^{(0)}_{\alpha\beta}\mathcal{E}^{(0)*}_{\alpha'\beta'} &= \frac{1}{3}\Pi_{\alpha\beta}\Pi_{\alpha'\beta'}, \\
\mathcal{E}^{(1)}_{\alpha\beta}\mathcal{E}^{(1)*}_{\alpha'\beta'} &= \frac{1}{2}\left(\Pi_{\alpha\alpha'}\Pi_{\beta\beta'} - \Pi_{\alpha\beta'}\Pi_{\alpha'\beta}\right), \\
\mathcal{E}^{(2)}_{\alpha\beta}\mathcal{E}^{(2)*}_{\alpha'\beta'} &= \frac{1}{2}\left(\Pi_{\alpha\alpha'}\Pi_{\beta\beta'} + \Pi_{\alpha\beta'}\Pi_{\alpha'\beta}\right) - \frac{1}{3}\Pi_{\alpha\beta}\Pi_{\alpha'\beta'}.
\end{aligned} \tag{318}$$

Bibliography

[1] Particle Data Group, PAea Zyla, RM Barnett, J Beringer, O Dahl, DA Dwyer, DE Groom, C-J Lin, KS Lugovsky, E Pianori, et al. Review of particle physics. *Progress of Theoretical and Experimental Physics*, 2020(8):083C01, 2020.

[2] Georges Aad et al. Observation of a new particle in the search for the Standard Model Higgs boson with the ATLAS detector at the LHC. *Phys. Lett. B*, 716:1–29, 2012.

[3] Serguei Chatrchyan et al. Observation of a New Boson at a Mass of 125 GeV with the CMS Experiment at the LHC. *Phys. Lett. B*, 716:30–61, 2012.

[4] Albert M Sirunyan et al. A measurement of the Higgs boson mass in the diphoton decay channel. *Phys. Lett. B*, 805:135425, 2020.

[5] Tao Han. Collider phenomenology: Basic knowledge and techniques. In *Theoretical Advanced Study Institute in Elementary Particle Physics: Physics in* $D \geqq 4$, pages 407–454, 8 2005.

[6] Tao Han, Yang Ma, and Keping Xie. High energy leptonic collisions and electroweak parton distribution functions. *Phys. Rev. D*, 103(3):L031301, 2021.

[7] Tao Han, Yang Ma, and Keping Xie. Quark and gluon contents of a lepton at high energies. *JHEP*, 02:154, 2022.

[8] C. F. von Weizsacker. Radiation emitted in collisions of very fast electrons. *Z. Phys.*, 88:612–625, 1934.

[9] E. J. Williams. Nature of the high-energy particles of penetrating radiation and status of ionization and radiation formulae. *Phys. Rev.*, 45:729–730, 1934.

[10] Gordon L. Kane, W. W. Repko, and W. B. Rolnick. The Effective W+-, Z0 Approximation for High-Energy Collisions. *Phys. Lett.*, 148B:367–372, 1984.

[11] Sally Dawson. The Effective W Approximation. *Nucl. Phys.*, B249:42–60, 1985.

[12] Paolo Ciafaloni and Denis Comelli. Electroweak evolution equations. *JHEP*, 11:022, 2005.

[13] Christian W. Bauer, Nicolas Ferland, and Bryan R. Webber. Standard Model Parton Distributions at Very High Energies. *JHEP*, 08:036, 2017.

[14] Marcello Ciafaloni, Paolo Ciafaloni, and Denis Comelli. Towards collinear evolution equations in electroweak theory. *Physical Review Letters*, 88(10), Feb 2002.

[15] Junmou Chen, Tao Han, and Brock Tweedie. Electroweak Splitting Functions and High Energy Showering. *JHEP*, 11:093, 2017.

[16] Marcello Ciafaloni, Paolo Ciafaloni, and Denis Comelli. Bloch-nordsieck violating electroweak corrections to inclusive tev scale hard processes. *Physical Review Letters*, 84(21):4810–4813, May 2000.

[17] Marcello Ciafaloni, Paolo Ciafaloni, and Denis Comelli. Bloch-nordsieck violation in spontaneously broken abelian theories. *Physical Review Letters*, 87(21), Nov 2001.

[18] Manuel Drees and Rohini M. Godbole. Virtual photon structure functions and the parton content of the electron. *Phys. Rev. D*, 50:3124–3133, 1994.

[19] Guido Altarelli and G. Parisi. Asymptotic Freedom in Parton Language. *Nucl. Phys.*, B126:298–318, 1977.

[20] V. N. Gribov and L. N. Lipatov. Deep inelastic e p scattering in perturbation theory. *Sov. J. Nucl. Phys.*, 15:438–450, 1972. [Yad. Fiz.15,781(1972)].

[21] L.N. Lipatov. The parton model and perturbation theory. *Sov. J. Nucl. Phys.*, 20:94–102, 1975.

[22] Yuri L. Dokshitzer. Calculation of the Structure Functions for Deep Inelastic Scattering and e+ e- Annihilation by Perturbation Theory in Quantum Chromodynamics. (In Russian). *Sov. Phys. JETP*, 46:641–653, 1977.

[23] R. Keith Ellis, W. James Stirling, and B. R. Webber. *QCD and collider physics*, volume 8. Cambridge University Press, 2 2011.

[24] John Campbell, Joey Huston, and Frank Krauss. *The Black Book of Quantum Chromodynamics: A Primer for the LHC Era.* Oxford University Press, 12 2017.

[25] Daniel de Florian, Germán F. R. Sborlini, and Germán Rodrigo. QED corrections to the Altarelli–Parisi splitting functions. *Eur. Phys. J. C*, 76(5):282, 2016.

[26] Daniel de Florian, Germán F. R. Sborlini, and Germán Rodrigo. Two-loop QED corrections to the Altarelli-Parisi splitting functions. *JHEP*, 10:056, 2016.

[27] A. Vogt, S. Moch, and J. A. M. Vermaseren. The Three-loop splitting functions in QCD: The Singlet case. *Nucl. Phys. B*, 691:129–181, 2004.

[28] S. Moch, J. A. M. Vermaseren, and A. Vogt. The Three loop splitting functions in QCD: The Nonsinglet case. *Nucl. Phys. B*, 688:101–134, 2004.

[29] H. Abramowicz et al. Combination of measurements of inclusive deep inelastic $e^{\pm}p$ scattering cross sections and QCD analysis of HERA data. *Eur. Phys. J. C*, 75(12):580, 2015.

[30] Sergey Alekhin, Johannes Bluemlein, Sven-Olaf Moch, and Rengaile Placakyte. The new ABMP16 PDF. *PoS*, DIS2016:016, 2016.

[31] S. Bailey, T. Cridge, L. A. Harland-Lang, A. D. Martin, and R. S. Thorne. Parton distributions from LHC, HERA, Tevatron and fixed target data: MSHT20 PDFs. *Eur. Phys. J. C*, 81(4):341, 2021.

[32] Tie-Jiun Hou et al. New CTEQ global analysis of quantum chromodynamics with high-precision data from the LHC. *Phys. Rev. D*, 103(1):014013, 2021.

[33] Richard D. Ball et al. Parton distributions from high-precision collider data. *Eur. Phys. J. C*, 77(10):663, 2017.

[34] Pedro Jimenez-Delgado and Ewald Reya. Delineating parton distributions and the strong coupling. *Phys. Rev. D*, 89(7):074049, 2014.

[35] A. D. Martin, R. G. Roberts, W. J. Stirling, and R. S. Thorne. Parton distributions incorporating QED contributions. *Eur. Phys. J.*, C39:155–161, 2005.

[36] Richard D. Ball, Valerio Bertone, Stefano Carrazza, Luigi Del Debbio, Stefano Forte, Alberto Guffanti, Nathan P. Hartland, and Juan Rojo. Parton distributions with QED corrections. *Nucl. Phys.*, B877:290–320, 2013.

[37] Carl Schmidt, Jon Pumplin, Daniel Stump, and C. P. Yuan. CT14QED parton distribution functions from isolated photon production in deep inelastic scattering. *Phys. Rev.*, D93(11):114015, 2016.

[38] Aneesh Manohar, Paolo Nason, Gavin P. Salam, and Giulia Zanderighi. How bright is the proton? A precise determination of the photon parton distribution function. *Phys. Rev. Lett.*, 117(24):242002, 2016.

[39] Aneesh V. Manohar, Paolo Nason, Gavin P. Salam, and Giulia Zanderighi. The Photon Content of the Proton. *JHEP*, 12:046, 2017.

[40] Valerio Bertone, Stefano Carrazza, Nathan P. Hartland, and Juan Rojo. Illuminating the photon content of the proton within a global PDF analysis. *SciPost Phys.*, 5(1):008, 2018.

[41] L. A. Harland-Lang, A. D. Martin, R. Nathvani, and R. S. Thorne. Ad Lucem: QED Parton Distribution Functions in the MMHT Framework. *Eur. Phys. J.*, C79(10):811, 2019.

[42] Keping Xie, T. J. Hobbs, Tie-Jiun Hou, Carl Schmidt, Mengshi Yan, and C. P. Yuan. The photon PDF within the CT18 global analysis. 6 2021.

[43] Christian W. Bauer and Bryan R. Webber. Polarization Effects in Standard Model Parton Distributions at Very High Energies. *JHEP*, 03:013, 2019.

[44] Tao Han, Yang Ma, and Keping Xie. Heavy flavors at high-energy lepton colliders. 2022.

[45] Diogo Buarque et al. Vector Boson Scattering Processes: Status and Prospects. 6 2021.

[46] European Strategy for Particle Physics Preparatory Group. Physics briefing book, 2019.

[47] Philip Bambade, Tim Barklow, Ties Behnke, Mikael Berggren, James Brau, Philip Burrows, Dmitri Denisov, Angeles Faus-Golfe, Brian Foster, Keisuke Fujii, Juan Fuster, Frank Gaede, Paul Grannis, Christophe Grojean, Andrew Hutton, Benno List, Jenny List, Shinichiro Michizono, Akiya Miyamoto, Olivier Napoly, Michael Peskin, Roman Poeschl, Frank Simon, Jan Strube, Junping Tian, Maksym Titov, Marcel Vos, Andrew White, Graham Wilson, Akira Yamamoto, Hitoshi Yamamoto, and Kaoru Yokoya. The international linear collider: A global project, 2019.

[48] P. Roloff, R. Franceschini, U. Schnoor, and A. Wulzer. The compact linear e^+e^- collider (clic): Physics potential, 2018.

[49] Jean Pierre Delahaye, Marcella Diemoz, Ken Long, Bruno Mansoulié, Nadia Pastrone, Lenny Rivkin, Daniel Schulte, Alexander Skrinsky, and Andrea Wulzer. Muon Colliders. 1 2019.

[50] ALEGRO collaboration. Towards an advanced linear international collider, 2019.

[51] Mario Greco, Tao Han, and Zhen Liu. Isr effects for resonant higgs production at future lepton colliders. *Physics Letters B*, 763:409–415, Dec 2016.

[52] H. Spiesberger. Qed radiative corrections for parton distributions. *Physical Review D*, 52(9):4936–4940, Nov 1995.

[53] Markus Roth and Stefan Weinzierl. Qed corrections to the evolution of parton distributions. *Physics Letters B*, 590(3-4):190–198, Jun 2004.

[54] A. D. Martin, R. G. Roberts, W. J. Stirling, and R. S. Thorne. Parton distributions incorporating qed contributions. *The European Physical Journal C*, 39(2):155–161, Feb 2005.

[55] Aneesh V. Manohar and Wouter J. Waalewijn. Electroweak Logarithms in Inclusive Cross Sections. *JHEP*, 08:137, 2018.

[56] Gabriel Cuomo, Luca Vecchi, and Andrea Wulzer. Goldstone Equivalence and High Energy Electroweak Physics. *SciPost Phys.*, 8(5):078, 2020.

[57] V. M. Budnev, I. F. Ginzburg, G. V. Meledin, and V. G. Serbo. The Two photon particle production mechanism. Physical problems. Applications. Equivalent photon approximation. *Phys. Rept.*, 15:181–281, 1975.

[58] Stanley J. Brodsky. Photon-Photon Collisions: Past and Future. *Acta Phys. Polon. B*, 37:619–632, 2006.

[59] Vernon D. Barger, M. S. Berger, J. F. Gunion, and Tao Han. Studying a strongly interacting electroweak sector via longitudinal gauge boson scattering at a muon collider. *Phys. Rev. D*, 55:142–154, 1997.

[60] Antonio Costantini, Federico De Lillo, Fabio Maltoni, Luca Mantani, Olivier Mattelaer, Richard Ruiz, and Xiaoran Zhao. Vector boson fusion at multi-TeV muon colliders. 5 2020.

[61] Bartosz Fornal, Aneesh V. Manohar, and Wouter J. Waalewijn. Electroweak Gauge Boson Parton Distribution Functions. *JHEP*, 05:106, 2018.

[62] Antonio Costantini, Federico De Lillo, Fabio Maltoni, Luca Mantani, Olivier Mattelaer, Richard Ruiz, and Xiaoran Zhao. Vector boson fusion at multi-tev muon colliders, 2020.

[63] J. Alwall, R. Frederix, S. Frixione, V. Hirschi, F. Maltoni, O. Mattelaer, H. S. Shao, T. Stelzer, P. Torrielli, and M. Zaro. The automated computation of tree-level and next-to-leading order differential cross sections, and their matching to parton shower simulations. *JHEP*, 07:079, 2014.

[64] Wolfgang Kilian, Thorsten Ohl, and Jurgen Reuter. WHIZARD: Simulating Multi-Particle Processes at LHC and ILC. *Eur. Phys. J.*, C71:1742, 2011.

[65] Christian W. Bauer, Davide Provasoli, and Bryan R. Webber. Standard Model Fragmentation Functions at Very High Energies. *JHEP*, 11:030, 2018.

[66] Tao Han, Ian Lewis, and Zhen Liu. Colored Resonant Signals at the LHC: Largest Rate and Simplest Topology. *JHEP*, 12:085, 2010.

[67] P. Roloff, R. Franceschini, U. Schnoor, and A. Wulzer. The Compact Linear e^+e^- Collider (CLIC): Physics Potential. 12 2018.

[68] Jean Pierre Delahaye, Marcella Diemoz, Ken Long, Bruno Mansoulié, Nadia Pastrone, Lenny Rivkin, Daniel Schulte, Alexander Skrinsky, and Andrea Wulzer. Muon Colliders. 1 2019.

[69] Stefano Frixione, Michelangelo L. Mangano, Paolo Nason, and Giovanni Ridolfi. Improving the Weizsacker-Williams approximation in electron - proton collisions. *Phys. Lett. B*, 319:339–345, 1993.

[70] V. Bertone, M. Cacciari, S. Frixione, and G. Stagnitto. The partonic structure of the electron at the next-to-leading logarithmic accuracy in QED. *JHEP*, 03:135, 2020.

[71] Michael S. Chanowitz and Mary K. Gaillard. The TeV Physics of Strongly Interacting W's and Z's. *Nucl. Phys.*, B261:379–431, 1985.

[72] Tao Han, Yang Ma, and Keping Xie. Bread and butter physics at high-energy lepton colliders. 2021.

[73] Mario Greco, Tao Han, and Zhen Liu. ISR effects for resonant Higgs production at future lepton colliders. *Phys. Lett. B*, 763:409–415, 2016.

[74] T Barklow, D. Dannheim, M. O. Sahin, and D Schulte. Simulation of $\gamma\gamma \to$ hadrons background at CLIC. 2011.

[75] Manuel Drees and Rohini M. Godbole. Mini - jets and large hadronic backgrounds at e^+e^- supercolliders. *Phys. Rev. Lett.*, 67:1189–1192, 1991.

[76] Manuel Drees and Rohini M. Godbole. Aspects of two photon physics at linear e^+e^- colliders. *Z. Phys. C*, 59:591–616, 1993.

[77] Pisin Chen, Timothy L. Barklow, and Michael E. Peskin. Hadron production in gamma gamma collisions as a background for e^+e^- linear colliders. *Phys. Rev. D*, 49:3209–3227, 1994.

[78] R. M. Godbole, A. Grau, K. A. Mohan, G. Pancheri, and Y. N. Srivastava. Hadronic backgrounds from two photon processes at e^+e^- colliders. *Nuovo Cim. C*, 034S1:129–138, 2011.

[79] Marcel Froissart. Asymptotic behavior and subtractions in the Mandelstam representation. *Phys. Rev.*, 123:1053–1057, 1961.

[80] Andre Martin. Extension of the axiomatic analyticity domain of scattering amplitudes by unitarity. 1. *Nuovo Cim. A*, 42:930–953, 1965.

[81] Gerhard A. Schuler and Torbjorn Sjostrand. A Scenario for high-energy gamma gamma interactions. *Z. Phys. C*, 73:677–688, 1997.

[82] Torbjorn Sjostrand. High-energy physics event generation with PYTHIA 5.7 and JETSET 7.4. *Comput. Phys. Commun.*, 82:74–90, 1994.

[83] John Campbell and Tobias Neumann. Precision Phenomenology with MCFM. *JHEP*, 12:034, 2019.

[84] Enrico Bothmann et al. Event Generation with Sherpa 2.2. *SciPost Phys.*, 7(3):034, 2019.

[85] P. A. Zyla et al. Review of Particle Physics. *PTEP*, 2020(8):083C01, 2020.

[86] Tao Han, Wolfgang Kilian, Nils Kreher, Yang Ma, Jürgen Reuter, Tobias Striegl, and Keping Xie. Precision test of the muon-Higgs coupling at a high-energy muon collider. *JHEP*, 12:162, 2021.

[87] Tao Han, Adam K. Leibovich, Yang Ma, and Xiao-Ze Tan. Higgs boson decay to charmonia via c-quark fragmentation. 2 2022.

[88] Serguei Chatrchyan et al. Observation of a new boson at a mass of 125 GeV with the CMS experiment at the LHC. *Phys. Lett.*, B716:30–61, 2012.

[89] D. de Florian et al. Handbook of LHC Higgs Cross Sections: 4. Deciphering the Nature of the Higgs Sector. 2/2017, 10 2016.

[90] J. de Blas et al. Higgs Boson Studies at Future Particle Colliders. *JHEP*, 01:139, 2020.

[91] Projections for measurements of Higgs boson cross sections, branching ratios, coupling parameters and mass with the ATLAS detector at the HL-LHC. `https://cds.cern.ch/record/2652762`, Dec 2018.

[92] Sensitivity projections for Higgs boson properties measurements at the HL-LHC. `https://cds.cern.ch/record/2647699`, 2018.

[93] Richard Keith Ellis et al. Physics Briefing Book: Input for the European Strategy for Particle Physics Update 2020. 10 2019.

[94] *2020 Update of the European Strategy for Particle Physics.* CERN Council, Geneva, 2020.

[95] Howard Baer et al. The International Linear Collider Technical Design Report - Volume 2: Physics. 6 2013.

[96] Halina Abramowicz et al. The International Linear Collider Technical Design Report - Volume 4: Detectors. 6 2013.

[97] A. Abada et al. FCC-ee: The Lepton Collider: Future Circular Collider Conceptual Design Report Volume 2. *Eur. Phys. J. ST*, 228(2):261–623, 2019.

[98] Mingyi Dong et al. CEPC Conceptual Design Report: Volume 2 - Physics & Detector. 11 2018.

[99] M Aicheler et al. A Multi-TeV Linear Collider Based on CLIC Technology: CLIC Conceptual Design Report. 10 2012.

[100] M J Boland et al. Updated baseline for a staged Compact Linear Collider. 8 2016.

[101] Albert M Sirunyan et al. Evidence for Higgs boson decay to a pair of muons. *JHEP*, 01:148, 2021.

[102] Georges Aad et al. A search for the dimuon decay of the Standard Model Higgs boson with the ATLAS detector. *Phys. Lett. B*, 812:135980, 2021.

[103] Projections for measurements of Higgs boson signal strengths and coupling parameters with the ATLAS detector at a HL-LHC. `http://cds.cern.ch/record/1956710`, Oct 2014.

[104] A. Abada et al. FCC Physics Opportunities: Future Circular Collider Conceptual Design Report Volume 1. Technical Report 6, 2019.

[105] A. Abada et al. FCC-hh: The Hadron Collider: Future Circular Collider Conceptual Design Report Volume 3. *Eur. Phys. J. ST*, 228(4):755–1107, 2019.

[106] Nazar Bartosik et al. Detector and Physics Performance at a Muon Collider. *JINST*, 15(05):P05001, 2020.

[107] Daniel Schulte, Jean-Pierre Delahaye, Marcella Diemoz, Kenneth Long, Bruno Mansoulié, Nadia Pastrone, Lenny Rivkin, Alexander Skrinsky, and Andrea Wulzera. Prospects on Muon Colliders. *PoS*, ICHEP2020:703, 2021.

[108] K. R. Long, D. Lucchesi, M. A. Palmer, N. Pastrone, D. Schulte, and V. Shiltsev. Muon colliders to expand frontiers of particle physics. 1 2021.

[109] Dario Buttazzo, Roberto Franceschini, and Andrea Wulzer. Two Paths Towards Precision at a Very High Energy Lepton Collider. 12 2020.

[110] Tao Han, Da Liu, Ian Low, and Xing Wang. Electroweak couplings of the Higgs boson at a multi-TeV muon collider. *Phys. Rev. D*, 103(1):013002, 2021.

[111] Tao Han, Zhen Liu, Lian-Tao Wang, and Xing Wang. WIMPs at High Energy Muon Colliders. 9 2020.

[112] Tao Han, Shuailong Li, Shufang Su, Wei Su, and Yongcheng Wu. Heavy Higgs Bosons in 2HDM at a Muon Collider. 2 2021.

[113] Rodolfo Capdevilla, David Curtin, Yonatan Kahn, and Gordan Krnjaic. A Guaranteed Discovery at Future Muon Colliders. 6 2020.

[114] Wen Yin and Masahiro Yamaguchi. Muon $g-2$ at multi-TeV muon collider. 12 2020.

[115] Rodolfo Capdevilla, David Curtin, Yonatan Kahn, and Gordan Krnjaic. A No-Lose Theorem for Discovering the New Physics of $(g-2)_\mu$ at Muon Colliders. 1 2021.

[116] Wei Liu and Ke-Pan Xie. Probing electroweak phase transition with multi-TeV muon colliders and gravitational waves. *JHEP*, 04:015, 2021.

[117] Jiayin Gu, Lian-Tao Wang, and Cen Zhang. An unambiguous test of positivity at lepton colliders. 11 2020.

[118] Guo-yuan Huang, Farinaldo S. Queiroz, and Werner Rodejohann. Gauged $L_\mu - L_\tau$ at a muon collider. 1 2021.

[119] Rodolfo Capdevilla, Federico Meloni, Rosa Simoniello, and Jose Zurita. Hunting wino and higgsino dark matter at the muon collider with disappearing tracks. 2 2021.

[120] G. W. Bennett et al. Final Report of the Muon E821 Anomalous Magnetic Moment Measurement at BNL. *Phys. Rev. D*, 73:072003, 2006.

[121] B. Abi et al. Measurement of the Positive Muon Anomalous Magnetic Moment to 0.46 ppm. *Phys. Rev. Lett.*, 126(14):141801, 2021.

[122] Sidney R. Coleman, J. Wess, and Bruno Zumino. Structure of phenomenological Lagrangians. 1. *Phys. Rev.*, 177:2239–2247, 1969.

[123] Curtis G. Callan, Jr., Sidney R. Coleman, J. Wess, and Bruno Zumino. Structure of phenomenological Lagrangians. 2. *Phys. Rev.*, 177:2247–2250, 1969.

[124] Steven Weinberg. Effective Gauge Theories. *Phys. Lett. B*, 91:51–55, 1980.

[125] Thomas Appelquist and Claude W. Bernard. Strongly Interacting Higgs Bosons. *Phys. Rev. D*, 22:200, 1980.

[126] Anthony C. Longhitano. Low-Energy Impact of a Heavy Higgs Boson Sector. *Nucl. Phys. B*, 188:118–154, 1981.

[127] Antonio Dobado, Domenec Espriu, and Maria J. Herrero. Chiral Lagrangians as a tool to probe the symmetry breaking sector of the SM at LEP. *Phys. Lett. B*, 255:405–414, 1991.

[128] G. J. Gounaris, R. Kogerler, and H. Neufeld. Relationship Between Longitudinally Polarized Vector Bosons and their Unphysical Scalar Partners. *Phys. Rev. D*, 34:3257, 1986.

[129] A. Dobado, A. Gomez-Nicola, Antonio Lopez Maroto, and J. R. Pelaez. *Effective lagrangians for the standard model.* Springer-Verlag (Texts and Monographs in Physics), N.Y., USA, 1997.

[130] Aneesh Manohar and Howard Georgi. Chiral Quarks and the Nonrelativistic Quark Model. *Nucl. Phys. B*, 234:189–212, 1984.

[131] Andrew G. Cohen, David B. Kaplan, and Ann E. Nelson. Counting 4 pis in strongly coupled supersymmetry. *Phys. Lett. B*, 412:301–308, 1997.

[132] Steven Weinberg. Baryon and Lepton Nonconserving Processes. *Phys. Rev. Lett.*, 43:1566–1570, 1979.

[133] L. F. Abbott and Mark B. Wise. The Effective Hamiltonian for Nucleon Decay. *Phys. Rev. D*, 22:2208, 1980.

[134] W. Buchmuller and D. Wyler. Effective Lagrangian Analysis of New Interactions and Flavor Conservation. *Nucl. Phys. B*, 268:621–653, 1986.

[135] B. Grzadkowski, M. Iskrzynski, M. Misiak, and J. Rosiek. Dimension-Six Terms in the Standard Model Lagrangian. *JHEP*, 10:085, 2010.

[136] Adam Falkowski, Sanmay Ganguly, Phillippe Gras, Jose Miguel No, Kohsaku Tobioka, Natascia Vignaroli, and Tevong You. Light quark Yukawas in triboson final states. *JHEP*, 04:023, 2021.

[137] F. Maltoni, J. M. Niczyporuk, and S. Willenbrock. The Scale of fermion mass generation. *Phys. Rev. D*, 65:033004, 2002.

[138] Mauro Moretti, Thorsten Ohl, and Jurgen Reuter. O'Mega: An Optimizing matrix element generator. pages 1981–2009, 2001.

[139] Simon Brass, Wolfgang Kilian, and Jürgen Reuter. Parallel Adaptive Monte Carlo Integration with the Event Generator WHIZARD. *Eur. Phys. J. C*, 79(4):344, 2019.

[140] Neil D. Christensen, Claude Duhr, Benjamin Fuks, Jurgen Reuter, and Christian Speckner. Introducing an interface between WHIZARD and FeynRules. *Eur. Phys. J. C*, 72:1990, 2012.

[141] Ana Alboteanu, Wolfgang Kilian, and Juergen Reuter. Resonances and Unitarity in Weak Boson Scattering at the LHC. *JHEP*, 11:010, 2008.

[142] Wolfgang Kilian, Thorsten Ohl, Jurgen Reuter, and Marco Sekulla. High-Energy Vector Boson Scattering after the Higgs Discovery. *Phys. Rev. D*, 91:096007, 2015.

[143] Simon Brass, Christian Fleper, Wolfgang Kilian, Jürgen Reuter, and Marco Sekulla. Transversal Modes and Higgs Bosons in Electroweak Vector-Boson Scattering at the LHC. *Eur. Phys. J. C*, 78(11):931, 2018.

[144] Alessandro Ballestrero et al. Precise predictions for same-sign W-boson scattering at the LHC. *Eur. Phys. J. C*, 78(8):671, 2018.

[145] M. Beyer, W. Kilian, P. Krstonosic, Klaus Monig, J. Reuter, E. Schmidt, and H. Schroder. Determination of New Electroweak Parameters at the ILC - Sensitivity to New Physics. *Eur. Phys. J. C*, 48:353–388, 2006.

[146] Christian Fleper, Wolfgang Kilian, Jurgen Reuter, and Marco Sekulla. Scattering of W and Z Bosons at High-Energy Lepton Colliders. *Eur. Phys. J. C*, 77(2):120, 2017.

[147] E. Boos, H. J. He, W. Kilian, A. Pukhov, C. P. Yuan, and P. M. Zerwas. Strongly interacting vector bosons at TeV e+ e- linear colliders. *Phys. Rev. D*, 57:1553, 1998.

[148] E. Boos, H. J. He, W. Kilian, A. Pukhov, C. P. Yuan, and P. M. Zerwas. Strongly interacting vector bosons at TeV e+- e- linear colliders: Addendum. *Phys. Rev. D*, 61:077901, 2000.

[149] M. Aaboud et al. Combined measurement of differential and total cross sections in the $H \to \gamma\gamma$ and the $H \to ZZ^* \to 4\ell$ decay channels at $\sqrt{s} = 13$ TeV with the ATLAS detector. *Phys. Lett. B*, 786:114–133, 2018.

[150] Georges Aad et al. Study of (W/Z)H production and Higgs boson couplings using $H \to WW^*$ decays with the ATLAS detector. *JHEP*, 08:137, 2015.

[151] Albert M. Sirunyan et al. Measurements of properties of the Higgs boson decaying to a W boson pair in pp collisions at $\sqrt{s} = 13$ TeV. *Phys. Lett. B*, 791:96, 2019.

[152] M. Aaboud et al. Observation of Higgs boson production in association with a top quark pair at the LHC with the ATLAS detector. *Phys. Lett. B*, 784:173–191, 2018.

[153] Albert M Sirunyan et al. Observation of $\mathrm{t\bar{t}H}$ production. *Phys. Rev. Lett.*, 120(23):231801, 2018.

[154] Georges Aad et al. Evidence for the Higgs-boson Yukawa coupling to tau leptons with the ATLAS detector. *JHEP*, 04:117, 2015.

[155] Albert M Sirunyan et al. Observation of the Higgs boson decay to a pair of τ leptons with the CMS detector. *Phys. Lett. B*, 779:283–316, 2018.

[156] Georges Aad et al. Measurements of the Higgs boson production and decay rates and constraints on its couplings from a combined ATLAS and CMS analysis of the LHC pp collision data at $\sqrt{s} = 7$ and 8 TeV. *JHEP*, 08:045, 2016.

[157] Morad Aaboud et al. Observation of $H \to b\bar{b}$ decays and VH production with the ATLAS detector. *Phys. Lett. B*, 786:59–86, 2018.

[158] A. M. Sirunyan et al. Observation of Higgs boson decay to bottom quarks. *Phys. Rev. Lett.*, 121(12):121801, 2018.

[159] Albert M Sirunyan et al. Combined measurements of Higgs boson couplings in proton–proton collisions at $\sqrt{s} = 13\,\text{TeV}$. *Eur. Phys. J. C*, 79(5):421, 2019.

[160] Georges Aad et al. Combined measurements of Higgs boson production and decay using up to 80 fb^{-1} of proton-proton collision data at $\sqrt{s} = 13$ TeV collected with the ATLAS experiment. *Phys. Rev. D*, 101(1):012002, 2020.

[161] Yohei Noguchi. Observation of the Higgs decay to beauty quarks. *J. Phys. Conf. Ser.*, 1390(1):012046, 2019.

[162] Tilman Plehn and David L. Rainwater. Higgs Decays to Muons in Weak Boson Fusion. *Phys. Lett. B*, 520:108–114, 2001.

[163] Tao Han and Bob McElrath. $h \to \mu^+\mu^-$ via gluon fusion at the LHC. *Phys. Lett. B*, 528:81–85, 2002.

[164] M. Aaboud et al. Search for the Decay of the Higgs Boson to Charm Quarks with the ATLAS Experiment. *Phys. Rev. Lett.*, 120(21):211802, 2018.

[165] Albert M Sirunyan et al. A search for the standard model Higgs boson decaying to charm quarks. *JHEP*, 03:131, 2020.

[166] J R Andersen et al. Handbook of LHC Higgs Cross Sections: 3. Higgs Properties. 7 2013.

[167] Geoffrey T. Bodwin, Frank Petriello, Stoyan Stoynev, and Mayda Velasco. Higgs boson decays to quarkonia and the $H\bar{c}c$ coupling. *Phys. Rev. D*, 88(5):053003, 2013.

[168] Geoffrey T. Bodwin, Hee Sok Chung, June-Haak Ee, Jungil Lee, and Frank Petriello. Relativistic corrections to Higgs boson decays to quarkonia. *Phys. Rev. D*, 90(11):113010, 2014.

[169] Gilad Perez, Yotam Soreq, Emmanuel Stamou, and Kohsaku Tobioka. Constraining the charm Yukawa and Higgs-quark coupling universality. *Phys. Rev. D*, 92(3):033016, 2015.

[170] Gilad Perez, Yotam Soreq, Emmanuel Stamou, and Kohsaku Tobioka. Prospects for measuring the Higgs boson coupling to light quarks. *Phys. Rev. D*, 93(1):013001, 2016.

[171] Ilaria Brivio, Florian Goertz, and Gino Isidori. Probing the Charm Quark Yukawa Coupling in Higgs+Charm Production. *Phys. Rev. Lett.*, 115(21):211801, 2015.

[172] Search for $H^0 \to b\bar{b}$ or $c\bar{c}$ in association with a W or Z boson in the forward region of pp collisions. Sep 2016.

[173] Tao Han, Benjamin Nachman, and Xing Wang. Charm-quark Yukawa Coupling in $h \to c\bar{c}\gamma$ at LHC. *Phys. Lett. B*, 793:90–96, 2019.

[174] Lina Alasfar, Roberto Corral Lopez, and Ramona Gröber. Probing Higgs couplings to light quarks via Higgs pair production. *JHEP*, 11:088, 2019.

[175] Nina M. Coyle, Carlos E. M. Wagner, and Viska Wei. Bounding the charm Yukawa coupling. *Phys. Rev. D*, 100(7):073013, 2019.

[176] J. A. Aguilar-Saavedra, J. M. Cano, and J. M. No. More light on Higgs flavor at the LHC: Higgs boson couplings to light quarks through $h + \gamma$ production. *Phys. Rev. D*, 103(9):095023, 2021.

[177] Direct constraint on the Higgs-charm coupling from a search for Higgs boson decays to charm quarks with the ATLAS detector, Jun 2021. All figures including auxiliary figures are available at https://atlas.web.cern.ch/Atlas/GROUPS/PHYSICS/CONFNOTES/ATLAS-CONF-2021-021.

[178] Ben Carlson, Tao Han, and Sze Ching Iris Leung. Higgs boson to charm quark decay in vector boson fusion plus a photon. *Phys. Rev. D*, 104(7):073006, 2021.

[179] Morad Aaboud et al. Searches for exclusive Higgs and Z boson decays into $J/\psi\gamma$, $\psi(2S)\gamma$, and $\Upsilon(nS)\gamma$ at $\sqrt{s} = 13$ TeV with the ATLAS detector. *Phys. Lett. B*, 786:134–155, 2018.

[180] Albert M Sirunyan et al. Search for rare decays of Z and Higgs bosons to J/ψ and a photon in proton-proton collisions at $\sqrt{s} = 13$ TeV. *Eur. Phys. J. C*, 79(2):94, 2019.

[181] Gino Isidori, Aneesh V. Manohar, and Michael Trott. Probing the nature of the Higgs-like Boson via $h \to V\mathcal{F}$ decays. *Phys. Lett. B*, 728:131–135, 2014.

[182] Alexander L. Kagan, Gilad Perez, Frank Petriello, Yotam Soreq, Stoyan Stoynev, and Jure Zupan. Exclusive Window onto Higgs Yukawa Couplings. *Phys. Rev. Lett.*, 114(10):101802, 2015.

[183] Matthias König and Matthias Neubert. Exclusive Radiative Higgs Decays as Probes of Light-Quark Yukawa Couplings. *JHEP*, 08:012, 2015.

[184] Zhan Sun and Yang Ma. Inclusive productions of $\Upsilon(1S, 2S, 3S)$ and $\chi_b(1P, 2P, 3P)$ via the Higgs boson decay. *Phys. Rev. D*, 100(9):094019, 2019.

[185] Cong-Feng Qiao, Feng Yuan, and Kuang-Ta Chao. Quarkonium production in SM Higgs decays. *J. Phys. G*, 24:1219–1226, 1998.

[186] Jun Jiang and Cong-Feng Qiao. B_c Production in Higgs Boson Decays. *Phys. Rev. D*, 93(5):054031, 2016.

[187] G. Apollinari, O. Brüning, T. Nakamoto, and Lucio Rossi. High Luminosity Large Hadron Collider HL-LHC. *CERN Yellow Rep.*, (5):1–19, 2015.

[188] Geoffrey T. Bodwin, Eric Braaten, and G. Peter Lepage. Rigorous QCD analysis of inclusive annihilation and production of heavy quarkonium. *Phys. Rev. D*, 51:1125–1171, 1995. [Erratum: Phys.Rev.D 55, 5853 (1997)].

[189] Estia J Eichten and Chris Quigg. Quarkonium wave functions at the origin: an update. 4 2019.

[190] Geoffrey T. Bodwin, Hee Sok Chung, U-Rae Kim, and Jungil Lee. Fragmentation contributions to J/ψ production at the Tevatron and the LHC. *Phys. Rev. Lett.*, 113(2):022001, 2014.

[191] Kuang-Ta Chao, Yan-Qing Ma, Hua-Sheng Shao, Kai Wang, and Yu-Jie Zhang. J/ψ Polarization at Hadron Colliders in Nonrelativistic QCD. *Phys. Rev. Lett.*, 108:242004, 2012.

[192] Yu Feng, Bin Gong, Chao-Hsi Chang, and Jian-Xiong Wang. Remaining parts of the long-standing J/ψ polarization puzzle. *Phys. Rev. D*, 99(1):014044, 2019.

[193] M. Tanabashi et al. Review of Particle Physics. *Phys. Rev. D*, 98(3):030001, 2018.

[194] Johann H. Kuhn, Matthias Steinhauser, and Christian Sturm. Heavy Quark Masses from Sum Rules in Four-Loop Approximation. *Nucl. Phys. B*, 778:192–215, 2007.

[195] R. Mertig, M. Bohm, and Ansgar Denner. FEYN CALC: Computer algebraic calculation of Feynman amplitudes. *Comput. Phys. Commun.*, 64:345–359, 1991.

[196] Vladyslav Shtabovenko, Rolf Mertig, and Frederik Orellana. New Developments in FeynCalc 9.0. *Comput. Phys. Commun.*, 207:432–444, 2016.

[197] Vladyslav Shtabovenko, Rolf Mertig, and Frederik Orellana. FeynCalc 9.3: New features and improvements. *Comput. Phys. Commun.*, 256:107478, 2020.

[198] para: A Mathematica package to set up the SM parameters. `https://github.com/YangPhy/para/releases/tag/v1.0.0`, Aug 2021.

[199] K. G. Chetyrkin, Johann H. Kuhn, and M. Steinhauser. RunDec: A Mathematica package for running and decoupling of the strong coupling and quark masses. *Comput. Phys. Commun.*, 133:43–65, 2000.

[200] Florian Herren and Matthias Steinhauser. Version 3 of RunDec and CRunDec. *Comput. Phys. Commun.*, 224:333–345, 2018.

[201] A. M. Sirunyan et al. Measurement of quarkonium production cross sections in pp collisions at $\sqrt{s} = 13$ TeV. *Phys. Lett. B*, 780:251–272, 2018.

[202] P. Artoisenet, J. P. Lansberg, and F. Maltoni. Hadroproduction of J/ψ and Υ in association with a heavy-quark pair. *Phys. Lett. B*, 653:60–66, 2007.

[203] Emilien Chapon et al. Prospects for quarkonium studies at the high-luminosity LHC. *Prog. Part. Nucl. Phys.*, 122:103906, 2022.

[204] Xue-An Pan, Zhong-Ming Niu, Mao Song, Yu Zhang, Gang Li, and Jian-You Guo. J/ψ associated production with a bottom quark pair from the Higgs boson decay in next-to-leading order QCD. *Phys. Rev. D*, 105(1):014032, 2022.

[205] Marie E. Machacek and Michael T. Vaughn. Two Loop Renormalization Group Equations in a General Quantum Field Theory. 1. Wave Function Renormalization. *Nucl. Phys. B*, 222:83–103, 1983.

[206] Marie E. Machacek and Michael T. Vaughn. Two Loop Renormalization Group Equations in a General Quantum Field Theory. 2. Yukawa Couplings. *Nucl. Phys. B*, 236:221–232, 1984.

[207] Haukur Arason, Diego Castano, Bettina Keszthelyi, Samuel Mikaelian, Eric Piard, Pierre Ramond, and Brian Wright. Top quark and Higgs mass bounds from a numerical study of superGUTs. *Phys. Rev. Lett.*, 67:2933, 1991.

[208] H. Arason, D. J. Castano, B. Keszthelyi, S. Mikaelian, E. J. Piard, Pierre Ramond, and B. D. Wright. Renormalization group study of the standard model and its extensions. 1. The Standard model. *Phys. Rev. D*, 46:3945–3965, 1992.

[209] H. Arason, D. J. Castano, E. J. Piard, and Pierre Ramond. Mass and mixing angle patterns in the standard model and its minimal supersymmetric extension. *Phys. Rev. D*, 47:232–240, 1993.

[210] D. J. Castano, E. J. Piard, and Pierre Ramond. Renormalization group study of the Standard Model and its extensions. 2. The Minimal supersymmetric Standard Model. *Phys. Rev. D*, 49:4882–4901, 1994.

[211] B. Grzadkowski and M. Lindner. Nonlinear Evolution of Yukawa Couplings. *Phys. Lett. B*, 193:71, 1987.

[212] Wolfgang Altmannshofer, Stefania Gori, Alexander L. Kagan, Luca Silvestrini, and Jure Zupan. Uncovering Mass Generation Through Higgs Flavor Violation. *Phys. Rev. D*, 93(3):031301, 2016.

[213] Yotam Soreq, Hua Xing Zhu, and Jure Zupan. Light quark Yukawa couplings from Higgs kinematics. *JHEP*, 12:045, 2016.

[214] Fady Bishara, Ulrich Haisch, Pier Francesco Monni, and Emanuele Re. Constraining Light-Quark Yukawa Couplings from Higgs Distributions. *Phys. Rev. Lett.*, 118(12):121801, 2017.

[215] J. Duarte-Campderros, G. Perez, M. Schlaffer, and A. Soffer. Probing the Higgs–strange-quark coupling at e^+e^- colliders using light-jet flavor tagging. *Phys. Rev. D*, 101(11):115005, 2020.

[216] Wolfgang Altmannshofer, Joachim Brod, and Martin Schmaltz. Experimental constraints on the coupling of the Higgs boson to electrons. *JHEP*, 05:125, 2015.

[217] Roni Harnik, Joachim Kopp, and Jure Zupan. Flavor Violating Higgs Decays. *JHEP*, 03:026, 2013.

[218] Keith R. Dienes, Emilian Dudas, and Tony Gherghetta. Extra space-time dimensions and unification. *Phys. Lett. B*, 436:55–65, 1998.

[219] Keith R. Dienes, Emilian Dudas, and Tony Gherghetta. Grand unification at intermediate mass scales through extra dimensions. *Nucl. Phys. B*, 537:47–108, 1999.

[220] Thomas Appelquist, Hsin-Chia Cheng, and Bogdan A. Dobrescu. Bounds on universal extra dimensions. *Phys. Rev. D*, 64:035002, 2001.

[221] Thomas Appelquist, Bogdan A. Dobrescu, Eduardo Ponton, and Ho-Ung Yee. Proton stability in six-dimensions. *Phys. Rev. Lett.*, 87:181802, 2001.

[222] Gautam Bhattacharyya, Anindya Datta, Swarup Kumar Majee, and Amitava Raychaudhuri. Power law blitzkrieg in universal extra dimension scenarios. *Nucl. Phys. B*, 760:117–127, 2007.

[223] A. S. Cornell, Aldo Deandrea, Lu-Xin Liu, and Ahmad Tarhini. Renormalisation running of masses and mixings in UED models. *Mod. Phys. Lett. A*, 28(11):1330007, 2013.

[224] Mattias Blennow, Henrik Melbeus, Tommy Ohlsson, and He Zhang. Renormalization Group Running of the Neutrino Mass Operator in Extra Dimensions. *JHEP*, 04:052, 2011.

[225] Takuya Kakuda, Kenji Nishiwaki, Kin-ya Oda, and Ryoutaro Watanabe. Universal extra dimensions after Higgs discovery. *Phys. Rev. D*, 88:035007, 2013.

[226] Ammar Abdalgabar, A. S. Cornell, Aldo Deandrea, and Ahmad Tarhini. Evolution of Yukawa couplings and quark flavour mixings in 2UED models. *Phys. Rev. D*, 88:056006, 2013.

[227] A. S. Cornell, Aldo Deandrea, Lu-Xin Liu, and Ahmad Tarhini. Scaling of the CKM Matrix in the 5D MSSM. *Phys. Rev. D*, 85:056001, 2012.